THE UNIVERSITY *of* EDINBURGH

Non-physical energy in seismic interferometry

Simon King
BSc. Hons. Geophysics, 2007
University of Edinburgh

Thesis submitted in fulfilment of

the requirements for the degree of

Doctor of Philosophy

School of GeoSciences

University of Edinburgh

2012

Declaration

I declare that this thesis has been composed solely by myself and that it has not been submitted, either in whole or in part, in any previous application for a degree. Except where otherwise acknowledged, the work presented is entirely my own.

Simon King
May 2012

Abstract

Non-physical arrivals produced by seismic interferometry, the process whereby Green's functions are synthesized between two points by cross-correlation, cross-convolution or deconvolution, are often considered to provide little information about the Earth's subsurface. Their contributions are usually suppressed in interferometric Green's function estimates to suit existing methods of seismic velocity estimation which favour the more familiar physical arrivals. In this thesis we show that the non-physical arrivals retrieved in exploration-type settings are useful for determining the long-wavelength seismic velocity structure and can be used to obtain improved Green's function estimates.

First, we estimate the seismic velocity and layer thickness by measuring the signal coherency along traveltime curves between two receivers in a collection of traces consisting of cross-correlated wavefields, known as the correlation gather. The traveltime curves represent the traveltime differences between wavefields recorded at the two receivers. When the procedure is used to find the velocity and thickness of the uppermost layer, the traveltime curves implicitly incorporate the physical and non-physical wavefields in the Green's function estimates. When the procedure is applied to a model with more than one layer, the traveltime curves correspond to non-physical wavefields only in the Green's function estimates. Instead of suppressing multiple reflections as in conventional methods, the procedure incorporates the traveltimes of multiple reflections to constrain velocity and thickness estimates.

The procedure above is most suitable for recovering the first-layer seismic velocity. We propose a simpler method to estimate the seismic velocities corresponding to deeper layers. We find that the Green's functions contain very weak reflections, but are dominated by non-physical refractions if retrieved using a limited source aperture. The seismic velocities are easily identifiable as repeating bright spots after transforming the refraction-dominated Green's functions to the $\tau - p$ domain.

We show that non-physical reflections can be used constructively to provide physical reflections, and therefore improved Green's function estimates, by

using a cross-convolution operation in a new variant of seismic interferometry, called source-receiver interferometry. We also show that non-physical reflections associated with the cross-correlation of reflections from different interfaces allow for the direct estimation of interval velocities and layer thicknesses. This method removes the necessity to first find the root-mean-square velocities and two-way traveltimes required to compute the interval velocities by Dix inversion.

Overall, this thesis significantly improves our understanding of how non-physical energy in seismic interferometry both provides useful information about the Earth's subsurface and contributes to physical energy in particular interferometric methods.

Acknowledgements

I would like to thank Andrew Curtis for first, providing me with the opportunity to complete a PhD under his supervision and second, for guiding and supporting me throughout. The PhD has taught me a lot. Not only have I learned a great deal academically, the research has helped me to think more creatively and to remain positive (and patient) when the going got tough.

I thank the Natural Environment Research Council (NERC) and WesternGeco for supporting me financially. I thank Ed Kragh for supervising a research internship at Schlumberger Cambridge Research in the summer of 2007. The opportunity to research at the top-level in industry fuelled my desire to start the PhD in Edinburgh. I thank Dirk-Jan van Manen (WesternGeco) and Johan Robertsson (Schlumberger) for hosting me at their institutions during project reviews and for taking time out of their busy schedules to listen to presentations of my work.

I thank my family, especially my Mum and Dad, for supporting me throughout. They have always been there for me and travelled to Edinburgh to visit me when it was not always possible to go home. My sister Rachel has just completed a PhD in Manchester and followed in the footsteps of my Dad, the original Dr King. Needless to say, my Mum feels a little left out. Mum – it's never too late to start a PhD!

I've made several great friends during my time in Edinburgh. I first thank those from Edinburgh Seismic Research, Craig, David, Heather, Mohammad and Tom for making feel most welcome within the group. I must thank friends in the attic office in particular Andrew, Gijs, Jen, Matt, Niklas, Rosie and Ruth. Hopefully, we'll stay in touch. Also, to the members of the 5-a-side GeoSciences football team, thank you for your weekly contribution. I leave with fond memories even if we did get relegated once! Also, thank you to Dominic and Parisa, for putting up with me in St Leonards St.

Thank you to Andrew, Dieter, Matt and Rob for proof-reading chapters in this thesis. I would also like to thank reviewers Deyan Draganov, Dylan Mikesell

and Kurang Mehta for reviewing much of the work in this thesis. Their comments always inspired me to keep going and try new ideas.

Simon King, May 2012.

Contents

List of Tables

List of Figures

Chapter 1

Introduction

Seismology is loosely defined as the study of elastic waves propagating in the Earth. A seismic wave is usually excited by either a natural source, such as an earthquake, or by an artificial source, such as an explosion. These waves propagate through the Earth and reflect, refract or diffract at heterogeneities before being recorded at the surface where they are used to infer the physical and structural properties of the Earth's interior indirectly. Recent theoretical advances have shown that recordings of these waves, termed Green's functions if from a temporally impulsive point source, can be constructed under certain assumptions between any two points, for example between two receivers (Wapenaar, 2004; Wapenaar and Fokkema, 2006; van Manen et al., 2005, 2006), between two sources (Curtis et al., 2009) or between a source and receiver (Curtis, 2009; Curtis and Halliday, 2010b). The method has been termed seismic interferometry. The assumptions required are rarely met in practice resulting in 'spurious' or non-physical arrivals being produced in the Green's function estimates. In this thesis, we show that the non-physical arrivals can be used to estimate the physical properties of the Earth, as well as to create physical reflections in a variant

of source-receiver interferometry.

In this chapter, we introduce exploration seismology and provide a historical background and theoretical formulation of seismic interferometry. We then discuss how the non-physical arrivals are introduced and describe the few applications to date which make use of them. We finish with a thesis outline.

1.1 An introduction to exploration seismology

An earthquake is the significant release of energy caused by the sudden displacement of fractures, or *faults*, within the Earth. These events create seismic waves that propagate throughout the Earth. Depending on the strength of the seismic wave when it reaches the Earth's surface, the crust may shake or rupture. Seismologists measure the shaking at the surface using instruments called seismometers. The recorded signals contain information about the subsurface because the seismic waves have travelled through the Earth's interior.

Today and throughout the last century, many organizations have sought to determine if significant natural resources (e.g., oil and gas reserves) are present within the subsurface. In much the same way as seismologists use earthquakes to infer properties about the deep interior of the Earth, these organizations detonate artificial sources to create localized seismic waves to improve their understanding of a region's geology. Vast areas, up to thousands of kilometres squared, are surveyed on land or at sea using arrays of sources and seismometers/receivers. The most commonly used source on land is a vibrating truck. The shaking movement of the truck creates the necessary seismic waves. If the survey is conducted at sea, highly-pressured air from an 'air gun' towed behind a moving vessel is fired underneath the sea surface. The seismic waves travel through the subsurface and are reflected back toward the surface where they are recorded at receivers known as geophones on land or hydrophones at sea. The geophones are

usually positioned in large two-dimensional arrays. The hydrophones are towed on streamers behind the air-gun source. The main aim of most surveys is to create an image of the subsurface. Interpretation geophysicists analyse these images to make predictions about the presence of natural resources. The procedure is analogous to medical imaging where a computerized axial tomography (CAT) scan is performed to image otherwise inaccessible parts of the human body.

In exploration seismology, a data-processing sequence begins soon after the data is acquired. Firstly, any noise recordings are removed to improve the clarity of the reflections. Secondly, multiple reflections (also known as multiples), i.e., the reflections which experience one or more downward reflection before being recorded at the receiver, are suppressed. This is because many of the steps in the data processing sequence can only handle reflections which have reflected upward only once, before being recorded at the receivers. These upward reflections are known as the primary reflections. A procedure known as 'velocity analysis' then occurs. Velocity analysis refers to a variety of techniques which aim to determine the seismic velocities (i.e., the propagation velocities) of the underlying subsurface rocks. This is an important step because the resultant velocity model is used to reposition the seismic reflections from the surface where they are recorded to their true subsurface position. This final process known as migration, generates an image of the subsurface.

The data processing sequence above assumes that the wavefields are excited by sources and recorded at receivers. A new method termed seismic interferometry allows wavefields to be excited at the position of the receiver (i.e., the receiver acts as a virtual source). Seismic interferometry introduces non-physical arrivals in the wavefield estimates (i.e., wavefields that could not have propagated between the receiver locations). In this thesis we show how nonphysical arrivals can help provide information about the subsurface properties of the Earth. In the next section we provide a historical background of seismic interferometry.

1.2 Historical background of seismic interferometry

Claerbout (1968) showed that for a horizontally-layered 1D acoustic medium bounded by a free surface, the reflection response (the trace recorded if the source and receiver were at the free surface) could be obtained by the autocorrelation of the transmission response (the trace recorded if the source was in the half-space below). As stated in Rickett and Claerbout (1999), this led to the following conjecture:

> *"by cross-correlating noise traces recorded at two locations on the surface, we can construct the wavefield that would be recorded at one of the locations if there was a source at the other."*

A passive seismic experiment set up to test this conjecture produced inconclusive results (Cole, 1995). Although a similar procedure proved successful in estimating the Green's functions using noise sources on the surface of the Sun (Rickett and Claerbout, 1999), it was thought that factors including a short-recording time and poor coupling of the geophones hampered the results of Cole (1995). In fact, Aki (1957) showed that in a process referred to as microtremor analysis, shear-wave velocity profiles could be extracted from the the recordings of ambient noise.

Despite the fact 'Claerbout's' conjecture was postulated in seismology, the ultrasonics and acoustics communities made independent contributions that have helped to define interferometry as we know it today. The Green's function between transducers in a closed (perfectly reflecting) medium was extracted using diffusive ultrasonic wavefields (Lobkis and Weaver, 2001; Weaver and Lobkis, 2001). The result, although remarkable, required wavefield diffusivity, an unrealistic assumption in most applications. The work of Weaver and Lobkis (2001) inspired Matthias Fink and co-workers to investigate whether the Green's function could be retrieved in an open (absorbing), but scattering medium. Derode et al. (2003a,b) explained that the Green's function could be recovered by cross-correlations of coda waves if the receivers were surrounded by a boundary

of sources acting as a perfect time-reversed mirror (a boundary which reflects a signal backwards but with the time axis flipped). They argued that the wavefield from an interior source when time-reversed and emitted back into the medium from the boundary, will propagate 'backwards' in the medium, be recorded at any other receiver location, before refocusing at its original source location at $t = 0$ s (like ripples in a pond converging if a video recording is played backwards). This implies that a time-reversed ($t < 0$ s) direct Green's function between the interior source and the receiver is recorded. After refocusing at $t = 0$ s, the wavefield diverges from its original source location and is recorded at the receiver again, providing the 'forward-time' Green's function at $t > 0$ s. Derode et al. (2003a,b) had explained the recovery of Green's functions from the cross-correlation of coda waves using the symmetries of reciprocity and the principles of time-reversal.

These observations encouraged applications with respect to multiply-scattered waves in seismology. Coda waves, which make up the latter part of seismic signals, are thought to be composed of scattered waves from heterogeneities within the lithosphere. Campillo and Paul (2003) cross-correlated seismic codas, as well as microseismic noise, between station pairs in Mexico for 101 distant earthquakes. Surface waves were well-recovered in the stacked cross-correlations. Shapiro et al. (2005) cross-correlated one year's worth of ambient seismic noise between station pairs in California, USA. Their Green's function estimates show good comparison to surface waves emitted by suitably-positioned earthquakes. The Green's functions were then used to create high-resolution group velocity tomographic images of California.

Wapenaar (2003, 2004) showed using a correlation-type reciprocity theorem that the Green's function between two receivers positioned at the free surface is obtained by cross-correlating the recordings from a surrounding boundary of transient or noise sources, thereby providing the first rigorous mathematical proof of Claerbout's conjecture. The derivation makes no assumption about

the diffusivity of the wavefield or the scattering properties of the medium other than that the medium is non-attenuating. These derivations were extended by Wapenaar and Fokkema (2006), who derived Green's function representations for point, transient and uncorrelated noise sources in acoustic and elastic media. Similarly, van Manen et al. (2005, 2006) used a representation theorem to derive the Green's functions between two arbitrary points in inhomogeneous acoustic and elastic media as part of an efficient scheme for wavefield modelling.

Schuster et al. (2004) formed images of the subsurface and located the position of buried sources by migrating cross-correlated seismic recordings at the surface (the method was termed 'interferometric imaging' and he later coined 'seismic interferometry', a term now widely used in the seismic community). The imaging methods presented used both natural and artificial sources.

Bakulin and Calvert (2006) outlined the first significant exploration application of seismic interferometry. Their initial acquisition geometry consisted of surface shots, with receivers positioned in a horizontal well below a time-varying complex overburden. Seismic interferometry allowed them to create a 'virtual' source in the position of a subsurface receiver location. Hence, they manipulate the initial surface-to-downhole dataset into a secondary dataset which contains redatumed virtual sources and receivers at geophone positions. The secondary dataset is relatively free from complications which may arise from the overburden and therefore in theory allows for improved seismic imaging. Similar to the arguments of Derode et al. (2003a,b), Bakulin and Calvert (2006) explained the principles of the 'virtual source' method using time-reversal. Specifically, the wavefield is refocused at the virtual source position after scattering by the complex overburden having been time-reversed by sources at the surface of the Earth (sources at the surface are analogous to the time-reversed mirror as described by Derode et al. (2003a,b)). Energy then diverges from the receiver, providing the Green's function at positive times, as though a physical source was located at the position

of the receiver.

It is clear that several independent advances in ultrasonics (Lobkis and Weaver, 2001), acoustics (Derode et al., 2003b) and seismology (Campillo and Paul, 2003), contributed to the development of seismic interferometry. In a short space of time, the field of seismic interferometry has developed considerably and it continues to grow rapidly. For a complete description and overview of methods and recent applications the reader is directed to the tutorials of Wapenaar et al. (2010a,b). We will cover some of the more recent advances throughout this thesis.

1.3 Theory of seismic interferometry

We now present the mathematical formulation of seismic interferometry as shown in Wapenaar and Fokkema (2006). The representation is exact for a 3D inhomogeneous and lossless medium. The correlation-type reciprocity theorem between two independent states A and B is represented in the frequency domain by

$$\begin{aligned}\int_S \{p_A^* q_B + v_{i,A}^* f_{i,B} + q_A^* p_B + f_{i,A}^* v_{i,B}\} d^3\mathbf{x} \\ = \oint_{\partial S} \{p_A^* v_{i,B} + v_{i,A} p_B\} n_i d^2\mathbf{x},\end{aligned} \tag{1.1}$$

where p and v_i are the pressure and particle velocity, and are solutions to the equation of motion and stress-relation, f_i is the external volume force density, q is a source distribution in terms of volume injection rate density and the asterisk $(*)$ represents complex conjugation, or time reversal in the time domain (Wapenaar and Fokkema, 2006). Integrations are performed over an arbitrary spatial domain S (on the left-hand side of equation 1.1) enclosed by a boundary ∂S (on the right-hand side of equation 1.1) with n_i representing the ith component of an outward pointing normal vector at the boundary ∂S. Einstein's summation convention applies throughout. Replacing p and v_i by the appropriate acoustic Green's

functions recorded at receiver positions $\mathbf{x}_A$ and $\mathbf{x}_B$ (corresponding to states A and B), and assuming source-receiver reciprocity Wapenaar and Fokkema (2006) obtain the expression,

$$G(\mathbf{x}_B, \mathbf{x}_A) + G^*(\mathbf{x}_B, \mathbf{x}_A) = \oint_{\partial S} \frac{-1}{j\omega\rho(\mathbf{x})} (G^*(\mathbf{x}_B, \mathbf{x}) \partial_i \hat{G}(\mathbf{x}_A, \mathbf{x}) - (\partial_i G^*(\mathbf{x}_B, \mathbf{x})) \hat{G}(\mathbf{x}_A, \mathbf{x})) n_i d^2\mathbf{x}, \tag{1.2}$$

where $j = \sqrt{-1}$ and ρ is the density at $\mathbf{x}$. On the left-hand side $G(\mathbf{x}_B, \mathbf{x}_A) + G^*(\mathbf{x}_B, \mathbf{x}_A)$ represents the homogeneous Green's function as though the recording at $\mathbf{x}_B$ was fired at the receiver location $\mathbf{x}_A$. On the right-hand side, G represents the Green's function between a monopolar source at $\mathbf{x}$ recorded at $\mathbf{x}_A$ and $\mathbf{x}_B$. The term $\partial_i G$ represents the Green's function between a dipolar source at $\mathbf{x}$, with the dipole aligned with the coordinate axis i. Note that for transient and uncorrelated noise sources, Wapenaar and Fokkema (2006) show that equation 1.2 is replaced by a single cross-correlation between recordings at the receivers.

The multiplications $\partial_i G\ G^*$ and $G\partial\ G^*$ are equivalent to cross-correlations in the time domain. The integral of cross-correlations are performed for sources positioned on an arbitrary-shaped boundary ∂S enclosing the two receivers at $\mathbf{x}_A$ and $\mathbf{x}_B$ (Figure 1.1).

One major advantage of seismic interferometry is the suppresion of random noise in the Green's function estimates due to the inherent summing over sources. Cross-correlations between incoherent events are likely to destructively interfere during summation in equation 1.2. Seismic interferometry may be attractive in situations where it is important to improve the signal-to-noise ratio.

Seismic interferometry using equation 1.2 is difficult to implement in practice. First, we rarely have sources positioned on a closed boundary around the receivers; sources are usually only available at or close to the surface of the Earth. In fact, if a portion of the source boundary is positioned at the free surface, the cross-

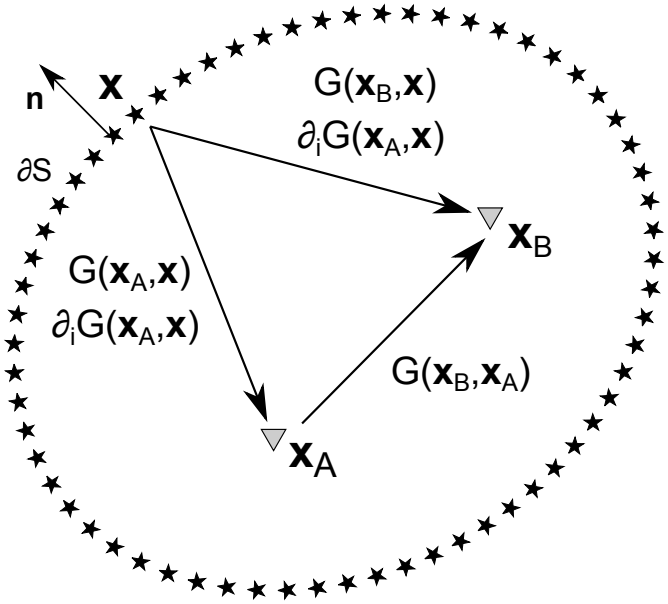

Figure 1.1: Two receivers positioned at $\mathbf{x}_A$ and $\mathbf{x}_B$ (denoted by triangles) record the wavefield from sources (denoted by stars) that are fired sequentially at $\mathbf{x}$ on the source boundary ∂S. The frequency-domain Green's function from a monopolar source at $\mathbf{x}$ and received at $\mathbf{x}_A$ is denoted $G(\mathbf{x}_A, \mathbf{x})$. The frequency-domain Green's function from a dipolar source at $\mathbf{x}$ and received at $\mathbf{x}_A$ is denoted $\partial_i G(\mathbf{x}_A, \mathbf{x})$. The same definitions apply for the Green's function recorded at $\mathbf{x}_B$.

correlations need only be performed for the sources at depth (Wapenaar and Fokkema, 2006), precisely where they are unlikely to exist.

It has been shown that a truncated source boundary leads to uncancelled (and undesirable) endpoint contributions and non-physical artifacts (Snieder et al., 2006b). Wapenaar (2006) has shown that if the medium is sufficiently inhomogeneous, the absence of sources at depth does not degrade the acoustic Green's function because the wavefield is scattered back toward the receivers as though reflected by a mirror. In theory not all sources are of equal importance. The method of stationary-phase (a procedure that enables the evaluation of the non-zero contributions to integrals like those in equation 1.2) has been adopted to find which sources have the most dominant contribution. Snieder (2004) has shown that inline sources (i.e., those sources parallel to the direction in which the data were acquired) are required to retrieve the directly-propagating Green's

function. Moreover, Snieder et al. (2006b) have shown that the stationary-phase sources required to retrieve the singly-reflected body waves are positioned near the surface of the Earth.

Second, the dipolar (derivative) sources required by equation 1.2 are usually unavailable. Wapenaar and Fokkema (2006) show that the Green's function can be retrieved by a single cross-correlation of monopolar Green's functions under certain approximations. These include the assumption that sources are located on a circle with very large radius such that energy propagating from a source leaves the boundary ∂S approximately perpendicularly and that no energy is reflected back into the medium via scatterers outside of the boundary.

A further assumption in the derivation of equation 1.2 requires that the medium be lossless (this assumption is required for the wave equation to be invariant for time-reversal). The Earth however, is strongly attenuating. Snieder (2007) show that extra sources are required within the medium if the losses are significant. It has been shown that by using an alternative equation, derived using cross-convolutional interferometry, that the electromagnetic (Slob and Wapenaar, 2007; Slob et al., 2007) and surface wave (Halliday and Curtis, 2008, 2009b) Green's functions are well-recovered in attenuative media. Interferometry by deconvolution is also applicable to attenuative media (Vasconcelos and Snieder, 2008a,b). Deconvolutional interferometry has the advantage of producing a Green's function estimate that is relatively independent of the source properties. This is particularly important if the recorded wavefields have been excited by a complicated source-time function. However, the approach introduces non-physical artifacts because of an imposed boundary condition that results because of an explicit division of Green's functions in the formulation. Multidimensional deconvolution (MDD) interferometry is the extension of deconvolutional interferometry to three dimensions and multiple energy sources (Wapenaar et al., 2008). The method has been shown to suppress non-physical artifacts present in

cross-correlational interferometry and be relatively insensitive to irregular source distributions.

Interferometry by MDD is only one such method which corrects for an inadequate source illumination. Douma and Snieder (2006) derive a correction factor for noise bias in coda wave interferometry. van der Neut and Bakulin (2009) outline a related application to correct the amplitude spectrum of the virtual source at a downhole receiver. Curtis and Halliday (2010a) remove the directional variations in source strength by applying a directional balancing algorithm. The method matches the biased Green's functions around the virtual source (computed for an array of surrounding receivers) to the modelled (unbiased) Green's functions using a correction factor.

1.4 Geometrical variations of seismic interferometry

The methods of interferometry discussed until now, construct the Green's function between two receivers using the cross-correlation of recordings from illuminating sources. By source-receiver reciprocity, Hong and Menke (2006) and Curtis et al. (2009) show that the Green's function between two sources can be estimated given their recordings on a surrounding set of receivers. This enables one of the sources to become a 'virtual' seismometer. Curtis et al. (2009) show that this manipulation offers a unique opportunity to place seismometers at the location of earthquake sources and hence, the technique would allow geophysicists to explore areas which were previously inaccessible or where receiver coverage is sparse.

Curtis and Halliday (2010b) outline a related method to find the Green's function between a source and receiver. The method requires recordings on both a surrounding source and receiver boundary and combines the approaches of inter-receiver and inter-source interferometry. Thus, they derive a more general form of

seismic interferometry (so-called source-receiver interferometry). Source-receiver interferometry is described in more detail in Chapter 4.

1.5 Non-physical arrivals

For the reasons described above, the assumptions required by seismic interferometry are often contravened. As a result, the Green's function estimates contain both physical and non-physical arrivals.

Several authors have sought to understand the contribution of non-physical arrivals for body waves (Snieder et al., 2006b, 2008; Curtis and Halliday, 2010a) and surface waves (Halliday and Curtis, 2009b), respectively. When several interfaces exist, the cross-correlation between reflections from different interfaces leads to 'spurious multiples'; non-physical wavefields that would be cancelled by destructive interference if sources existed at depth and not only at the surface (Snieder et al., 2006b). Snieder et al. (2008) demonstrate that the spurious arrivals due to scattering are cancelled provided there exists a closed integral of sources. Halliday and Curtis (2009b) derive the stationary-phase points of non-physical arrivals for surface waves and Curtis and Halliday (2010a) show that non-physical arrivals can be predicted by (1) adopting wavefield separation or (2) by reversing the role of the virtual source and receiver, (i.e., by changing the order of the cross-correlation).

Most researchers view the non-physical arrivals as unwanted contributions. As the understanding of non-physical arrivals has increased, a considerable focus aiming to suppress them has evolved in order to obtain Green's function estimates that truthfully resemble the actual impulse response (Bakulin and Calvert, 2006; Mehta et al., 2007; Wapenaar et al., 2008; Curtis and Halliday, 2010a; Wapenaar et al., 2011; van der Neut et al., 2011). Bakulin and Calvert (2006) time-window the direct arrivals at the virtual source to prevent the cross-correlations between

reflections (and hence introduction of the spurious multiples) at the two receivers. Mehta et al. (2007) show that non-physical arrivals are suppressed in the virtual source method of Bakulin and Calvert (2006) by cross-correlating upgoing and downgoing wavefields at the receivers. Non-physical arrivals are suppressed in the method of interferometry by MDD (Wapenaar et al., 2008, 2011; van der Neut et al., 2011) and once Curtis and Halliday (2010a) obtain a prediction of the non-physical arrivals, they are removed from the interferometric estimates using a 2D helical least-squares matching filter.

The suppression methods outlined above are not always applicable to surface seismic data. The approaches of Bakulin and Calvert (2006), Mehta et al. (2007) and Wapenaar et al. (2008) involve time-windowing the direct arrivals. This assumes that the direct arrival can be easily separated from the scattered wavefields. Furthermore, the approaches of Bakulin and Calvert (2006) and Mehta et al. (2007) require sources to be positioned at the appropriate stationary-phase locations. This usually requires sources and receives to be vertically offset from each other. Moreover, the approaches of Mehta et al. (2007) and Wapenaar et al. (2008) involve wavefield separation into upgoing/downgoing components.

In there own right, these correction methods described above are extremely important however,

> "spurious waves can glean information about the medium that is complementary to the direct and scattered waves".
>
> Snieder, R., K. van Wijk, M. Haney, and R. Calvert, 2008
> Cancellation of spurious arrivals in Green's function extraction
> and the generalized optical theorem:
> Physical Review E, **78**, 036606.

Snieder et al. (2008) made this inspiring comment in the final sentence of their work relating to the generalized optical theorem. The authors state that the

location of a scatterer can be constrained by using both the non-physical and physical wavefields. Furthermore, Mikesell et al. (2009) show that non-physical wavefields can be used to infer properties of the medium. Figure 1.2(a) (taken from Mikesell et al. (2009)) shows the Green's function estimates along a receiver array. The Green's functions were obtained using only a line of monopolar sources in a two-layer model (Figure 1.2(b)). As well as the physical direct, reflected and refracted arrivals, they obtain a non-physical arrival (denoted the virtual refraction). The virtual refraction is associated with the cross-correlation of refracted energy and defines the velocity of the underlying medium (Figure 1.2(b)). The virtual refraction is easily identifiable because it passes through the origin.

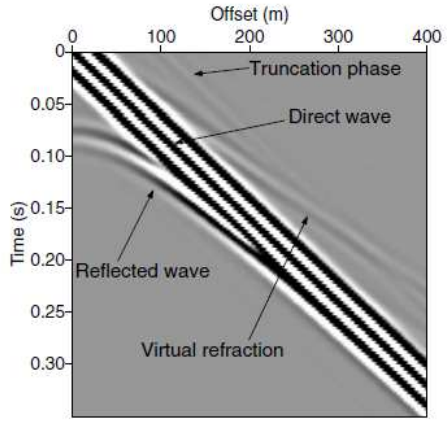

(a)

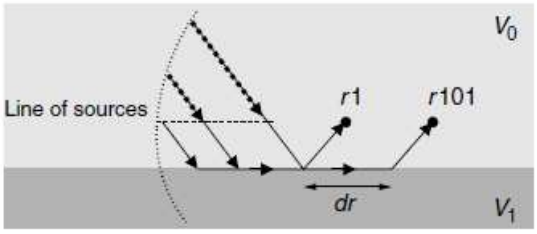

(b)

Figure 1.2: (a) The Green's functions along a line of receivers showing the direct, reflected, refracted and virtual refracted wavefields. (b) Acquisition geometry and paths for taken for refracted waves travelling between receiver 1 and receiver 101 for example.

Despite there being relatively few examples that use non-physical wavefields to gain information about properties of the medium, the work of Snieder et al. (2008) and Mikesell et al. (2009) suggests that this avenue of research shows considerable promise. However, there are still some significant challenges to be addressed.

If the suppression methods are difficult to implement or not applicable as described above, it is likely that non-physical arrivals will persist in the Green's function estimates. Rather than develop new suppression methods to supplement those described above, it seems plausible to use the non-physical energy to our advantage. This requires new methods and procedures to be developed that utilize the non-physical energy. In this thesis, we explore such ideas and outline methods which utilize the non-physical energy to estimate the seismic velocities and to obtain improved Green's function estimates.

1.6 Thesis Outline

In ***Chapter 2***, we use the cross-correlated wavefields obtained in seismic interferometry to extract velocity and layer-thickness parameters of 1D synthetic media. The procedure incorporates multiples correctly and further shows that the non-physical energy, erroneously produced in seismic interferometry, contains useful information about subsurface parameters.

In ***Chapter 3***, the velocity and thickness of the first layer are extracted from the reflected cross-correlations in a marine-type geometry using a semblance analysis similar to that explained in *Chapter 2*. Extraction of the first-layer parameters is relatively trivial. However, when these cross-correlations are summed over all sources, the resulting Green's function estimates are dominated by non-physical refracted energy which can be used in a further semblance analysis to find the refraction velocities of deeper layers. We demonstrate the procedure

on 1D acoustic models and a more realistic 2.5D elastic model based on a North Sea oilfield.

Chapter 4 shows that the non-physical reflections can be converted into physical reflections using cross-convolutional interferometry resulting in improved Green's function estimates. We also show that the non-physical reflections synthesized in cross-correlational interferometry allow for the direct estimation of subsurface interval velocities and layer thicknesses from surface seismic data.

In ***Chapter 5*** we provide some general applications of seismic interferometry. We begin by discussing how the methods of ***Chapter 2*** could be extended to elastic recordings or passive data. We outline the link between source-receiver interferometry (***Chapter 4***) and internal multiple prediction and finish by describing how non-physical arrivals can be emphasized in the Green's function estimates in preparation for applications such as those described throughout which make use of their contributions. We provide a brief conclusion in ***Chapter 6***.

1.7 Publications

Chapter 2 is published as:

- King, S., A. Curtis, and T.L. Poole, 2011, Interferometric velocity analysis using physical and nonphysical energy: Geophysics, **76**, no. 1, SA35-SA49.

Chapter 3 is published as:

- King, S., and A. Curtis, 2011, Velocity analysis using both reflections and refractions in seismic interferometry: Geophysics, **76**, no. 5, SA83-SA96.

Chapter 4 is published as:

- King, S., and A. Curtis, 2012, Improving Green's function estimates using nonphysical reflections (spurious multiples) in source-receiver interferometry: Geophysics, **77**, no. 1, Q15-Q25.

Chapter 2

Interferometric velocity analysis using physical and non-physical energy

To extract the accurate, or sometimes termed physical, inter-receiver Green's function the receiver pair must be illuminated by a complete and surrounding boundary of sources. Deviations of physically realistic source and receiver geometries from those required by theory result in errors to the Green's function estimate. These errors are manifested as apparent energy that could not have propagated between receiver locations – so-called non-physical energy. We have developed a novel method of velocity analysis that uses both the physical and non-physical wavefield energy in the cross-correlated data generated between receiver pairs. This method is used to constrain the root-mean-square (rms) velocity and layer thickness of a locally one-dimensional medium. These estimates are used in turn to compute the piece-wise constant interval velocity. Instead of suppressing multiple energy as in conventional common midpoint velocity analysis, the method uses the multiply reflected wavefield to further constrain the rms velocity and layer-thickness estimates. In particular, we determine that

the non-physical energy contains useful physical information. By using the non-physical energy associated with the truncation of the source boundary and the cross-correlation of reflected waves, a better-defined estimate of the rms velocity and layer thickness is achieved. Because this energy is excited far from the receiver pair, the technique may be ideally suited to long-offset seismic reflection data. We found that interferometric velocity analysis works best to characterize the first few layers beneath a receiver array. We have considered an acquisition configuration that can be used in a marine seismic setting.

2.1 Introduction

The most common form of velocity analysis in exploration seismology begins with the construction of a velocity spectrum (Taner and Koehler, 1969). Obtained from common midpoint (CMP) gathers, the velocity spectrum displays the signal coherency along traveltime curves that vary with respect to the root-mean-square (rms) velocity and the zero-offset two-way traveltime. In general, peaks in the velocity spectrum that have a high moveout velocity are associated with primary reflections. The rms velocities and traveltimes at these peaks are selected and used to perform a normal moveout (NMO) correction that flattens the corresponding traveltime hyperbola. To derive the interval velocity for each layer, the picked rms velocity and traveltime pairs are input to the Dix equation (Dix, 1955).

In this process, multiples are treated as noise. They can be distinguished from the primary reflections because they show a lower moveout velocity at the equivalent traveltime of the primary reflections. For this reason they are often suppressed by NMO correction and subsequent stacking.

This methodology often forms the basis of the current industry practice for

obtaining an initial stacked section of the subsurface. However, a disadvantage of this approach is its failure to use information from the multiple arrivals. In fact, multiple energy clutters the velocity spectra making the picking of primary energy more difficult. Multiples provide secondary ensonification of the subsurface and hence in principle provide additional information. For example, Muijs et al. (2007) use free-surface multiples together with the primary arrivals to image subsurface reflectors. Despite this potential advantage multiples are often removed from, or suppressed in data prior to the onset of velocity analysis.

Another drawback of conventional velocity analysis is that it does not comply with wide-angle or long-offset seismic reflection data. Specifically, when the small-spread approximation is violated (i.e., the maximum offset is large compared with the depth of the target) the conventional two-term hyperbolic traveltime equation derived by Taner and Koehler (1969) becomes invalid. To overcome this limitation, several alternative techniques have been proposed. The method of Diebold and Stoffa (1981) and Schultz (1982) transforms the seismic reflection data into the $\tau - p$ domain. Here, $p = \frac{dt}{dx}$ is the horizontal slowness or ray parameter, and $\tau = t - px$ where t and x are the two-way traveltime and horizontal offset, respectively. Such an approach aids the interpretation of reflection data in horizontally-layered media and lends itself well to the direct estimation of interval velocities. González-Serrano and Claerbout (1984) outline a method to obtain the interval velocity using a linear transformation of the CMP gather. Several authors have built upon this work, and each such study aims to obtain the interval velocities and layer thicknesses from wide-angle or long-offset seismic reflection data (Nowroozi, 1990; Sain and Kaila, 1996; Kumar et al., 2003).

In this chapter, we propose a new method of interval velocity and layer-thickness estimation closely associated with seismic interferometry. To date, much attention has focused on the estimation of the Green's function and its subsequent improvement to match the desired impulse response between

receiver pairs (Douma and Snieder, 2006; Mehta et al., 2007; Wapenaar et al., 2008; van der Neut and Bakulin, 2009; Curtis and Halliday, 2010a). However, in many of these examples, where interferometric theory cannot be realised exactly in practice, non-physical arrivals persist in the Green's function estimate. Non-physical arrivals created by the cross-correlation of physical arrivals still satisfy the wave equation and thus contain information about the nature of the subsurface. They can result from several mechanisms but usually depend upon the acquisition geometry and the scattering and/or physical properties of the medium under consideration. In exploration seismology, sources are predominantly located near the surface of the Earth; in this instance the source boundary is incomplete (e.g., there are no sources in the deep subsurface), and sources positioned near the array end points lead to uncancelled non-physical contributions (Snieder et al., 2006b). Snieder et al. (2006b) also show that the cross-correlation of reflected waves lead to non-physical arrivals that would otherwise be cancelled by the missing boundary sources at depth. Because these non-physical arrivals are dynamically equivalent to peg-leg multiples, those authors term them spurious multiples. For body waves scattered by a single diffractor, Snieder et al. (2008) derive expressions for the non-physical arrivals as part of a generalized optical theorem. Halliday and Curtis (2009a) present a similar derivation for surface waves. Mikesell et al. (2009) demonstrate that the cross-correlation of refracted energy leads to a non-physical arrival they term the virtual refraction. The gradient of this non-physical arrival defines the velocity of the underlying medium in a two-layer model.

We extract rms velocity and layer thickness estimates using the theory of controlled-source seismic interferometry. We perform rms velocity and layer-thickness estimation on so-called correlation gathers between receiver pairs. These estimates are then used to derive the interval velocity. Unlike the standard velocity-estimation techniques described above, we incorporate free-surface and

interbed multiples in our analysis to further constrain the rms velocity and layer-thickness estimates. We also use the non-physical energy contained within the correlation gather. This non-physical energy is associated with the cross-correlation of reflected waves by sources positioned near the end-points of the source boundary. In particular, we find that by using these sources, we obtain a more coherent estimate of the rms velocity and layer thickness. Furthermore, these sources are located at far offset from the receiver pair. Hence, the method presented is applicable to long-offset seismic reflection records.

In the next section, we define and interpret the correlation gather. We then introduce the deconvolution gather and explain why in the following examples the deconvolution gather approximates that of cross-correlation. Following this, we describe the process of velocity and layer-thickness estimation using a single acoustic layer over a half-space model. Next, the method is extended to find the rms and interval velocities of a multi-layered acoustic model. In the subsequent section, we compare the presented method with standard CMP velocity techniques. Finally, we discuss the implications of this work for exploration seismology.

2.1.1 Inter-receiver interferometry by cross-correlation

Wapenaar (2004), van Manen et al. (2005) and Wapenaar and Fokkema (2006) show that the exact acoustic Green's function $G(\mathbf{x}_B, \mathbf{x}_A) + G^*(\mathbf{x}_B, \mathbf{x}_A)$ between receivers at $\mathbf{x}_A$ and $\mathbf{x}_B$ can extracted by cross-correlating and summing the Green's functions from a surrounding boundary of monopolar and dipolar sources (equation 1.2, Chapter 1). To generate the exact Green's function between the receiver pair, it is necessary that the source boundary ∂S completely encloses $\mathbf{x}_A$ and $\mathbf{x}_B$, except for portions of ∂S that coincide with the Earth's free surface at which locations the integrand in equation 1.2 is equal to zero (van Manen et al., 2005, 2006; Wapenaar and Fokkema, 2006).

To apply seismic interferometry with only monopolar sources (e.g., vibrator trucks, dynamite and airguns) Wapenaar and Fokkema (2006) assume the far-field approximation and that the energy leaving each source is approximately perpendicular to ∂S. The Green's function $G(\mathbf{x}_B, \mathbf{x}_A)$ and its complex conjugate is then expressed approximately as,

$$G(\mathbf{x}_B, \mathbf{x}_A) + G^*(\mathbf{x}_B, \mathbf{x}_A) \approx \oint_{\partial S} \frac{2}{\rho c} G(\mathbf{x}_B, \mathbf{x}) G^*(\mathbf{x}_A, \mathbf{x}) d^2\mathbf{x}, \tag{2.1}$$

where $G(\mathbf{x}_i, \mathbf{x})$ denotes the frequency-domain Green's function received at $\mathbf{x}_i$ from a monopolar source positioned at $\mathbf{x}$ and ρ and c are the density and velocity at $\mathbf{x}$, respectively and are assumed to be constant at and outside of the boundary. After integrating over source locations ∂S, we obtain an approximation to the monopolar Green's function $G(\mathbf{x}_B, \mathbf{x}_A)$ as though a source was fired at $\mathbf{x}_A$ and a response was received at $\mathbf{x}_B$. Essentially, the cross-correlation operation isolates the phase differences between waves recorded at both of the receivers (Snieder, 2004). Thus, the phase of the Green's function estimate should remain equal to that of equation 1.2 however, if not fulfilled, the approximation introduces an amplitude error.

The Green's function between a boundary source positioned at $\mathbf{x}$ and recorded at $\mathbf{x}_A$ can be decomposed into its direct and reflected (scattered) component, $G_d(\mathbf{x}_A, \mathbf{x})$ and $G_r(\mathbf{x}_A, \mathbf{x})$ respectively,

$$G(\mathbf{x}_A, \mathbf{x}) = G_d(\mathbf{x}_A, \mathbf{x}) + G_r(\mathbf{x}_A, \mathbf{x}). \tag{2.2}$$

Substituting equation 2.2, the Green's function between $\mathbf{x}$ and $\mathbf{x}_A$, and its equivalent for $\mathbf{x}_B$ into the interferometric integral in equation 2.1, we can express

the cross-correlation as the sum of four terms:

$$\begin{aligned} G(\mathbf{x}_B,\mathbf{x}_A)+G^*(\mathbf{x}_B,\mathbf{x}_A) \approx \frac{2}{\rho c}\underbrace{\oint_{\partial S} G_d(\mathbf{x}_B,\mathbf{x})G_d^*(\mathbf{x}_A,\mathbf{x})d^2\mathbf{x}}_{C_1} \\ + \frac{2}{\rho c}\underbrace{\oint_{\partial S} G_r(\mathbf{x}_B,\mathbf{x})G_d^*(\mathbf{x}_A,\mathbf{x})d^2\mathbf{x}}_{C_2} \\ + \frac{2}{\rho c}\underbrace{\oint_{\partial S} G_d(\mathbf{x}_B,\mathbf{x})G_r^*(\mathbf{x}_A,\mathbf{x})d^2\mathbf{x}}_{C_3} \\ + \frac{2}{\rho c}\underbrace{\oint_{\partial S} G_r(\mathbf{x}_B,\mathbf{x})G_r^*(\mathbf{x}_A,\mathbf{x})d^2\mathbf{x}}_{C_4}. \end{aligned} \tag{2.3}$$

Term C_1 represents the cross-correlation of the direct waves at both receivers, C_2 represents the cross-correlation of the direct wave at $\mathbf{x}_A$ with the reflected waves at $\mathbf{x}_B$, C_3 represents the cross-correlation of the reflected waves at $\mathbf{x}_A$ with the direct wave at $\mathbf{x}_B$ and C_4 represents the cross-correlation of the reflected waves at both receivers.

Before integration, it is useful to display the cross-correlations between the receiver pair in equation 2.1 as a function of source position $\mathbf{x}$ (van Manen et al., 2005). This data display is referred to as the correlation gather by Mehta et al. (2008). To illustrate this concept we consider an acoustic model and the acquisition source geometry shown in Figure 2.1. The acquisition geometry represents a typical configuration of sources and receivers that could be extracted from marine seismic data. The data set, consisting of 400 shot gathers each with 301 receivers, was modeled using a 2D finite-difference scheme with a perfectly reflecting upper free surface (Robertsson et al., 1994). Each receiver records the response from a pressure source at a sample rate of 4 ms for a total of 3 s. Notice that the source boundary, as defined by seismic interferometry in equations 1.2 and 2.1, is incomplete in Figure 2.1 (side and lower boundary source sections are missing). Therefore, we would expect any subsequent Green's function estimates

made using this dataset to contain both physical and non-physical arrivals.

Figure 2.2 displays two shot gathers from the model in Figure 2.1. The shot from source 1 displays late-arriving primary, free-surface multiple and refraction arrivals (Figure 2.2(a)). The primary reflection and free-surface multiples are better depicted in Figure 2.2(b). The arrowhead annotates the primary reflection. The remaining arrivals are the free-surface multiples.

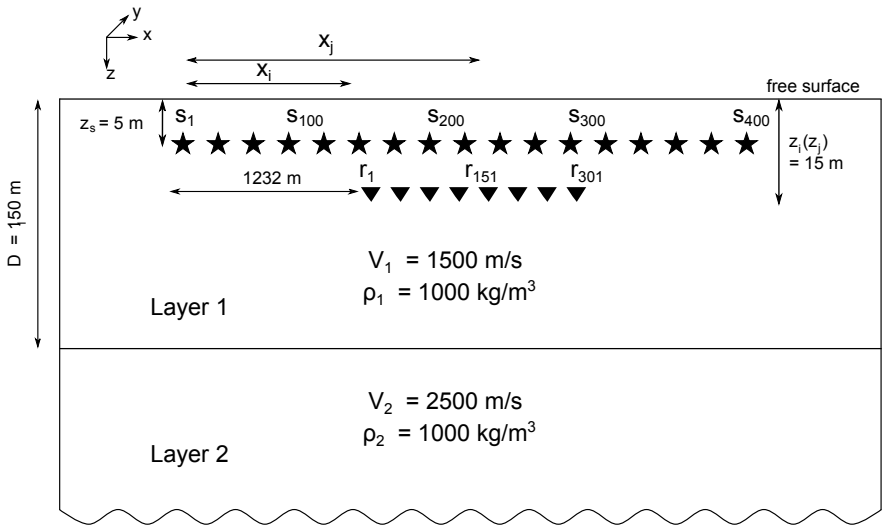

Figure 2.1: Model consisting of a layer over a half-space, both homogeneous. Layer 1 is bounded on top by a free surface and below by a planar interface at 150 m depth. The velocities (V_1 and V_2) and densities (ρ_1 and ρ_2) are shown. Four hundred sources ($s_1, ..., s_{400}$) indicated by stars illuminate 301 receivers ($r_1, ..., r_{301}$) indicated by triangles. Sources are fixed at 5-m depth and separated by 8-m intervals whilst receivers are positioned at 15-m depth and separated by 4-m intervals. Note that for clarity we do not show every source and receiver.

We now perform seismic interferometry. For $\mathbf{x}_A$ and $\mathbf{x}_B$ in equation 2.1, we choose receivers 1 and 151 respectively, offset from each other by 600 m. In all subsequent correlation and deconvolution plots, the correlation/deconvolution values have been scaled to the full range of the grey colormap. Figure 2.3(a) shows the correlation gather, Figure 2.3(b) displays the Green's function estimate, and Figure 2.3(f) shows the true Green's function between these receiver locations. To create the correlation gather we have cross-correlated the full wavefield (i.e., the direct, primary and free-surface multiples) at receiver 1 with the full wavefield at

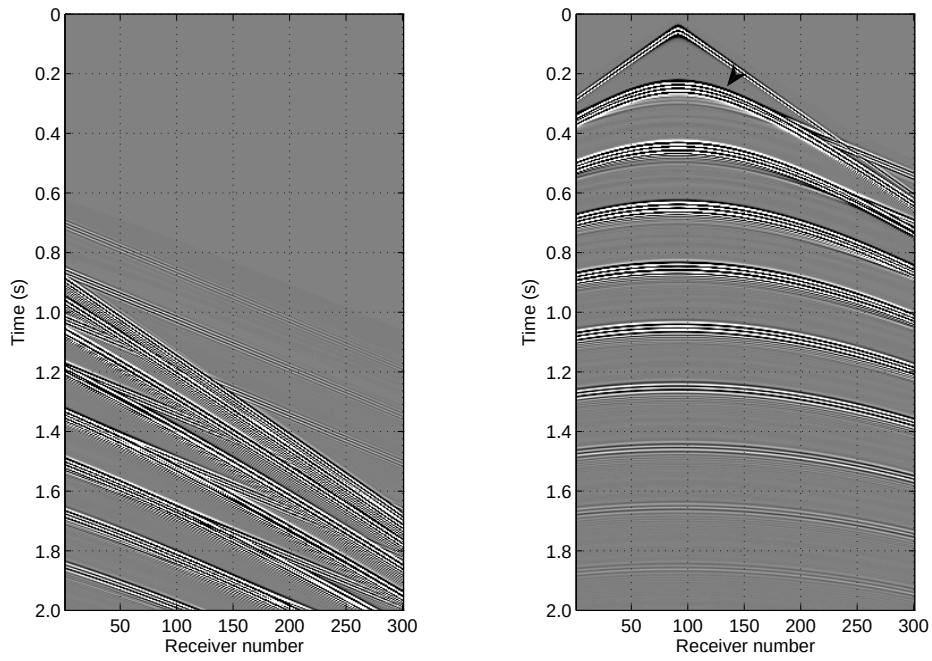

(a) (b)

Figure 2.2: Shot gathers from source 1 (a) and 200 (b) in Figure 2.1.

receiver 151 and plotted the result in the time domain as a function of the source position.

Any significant energy in the correlation gather occurs at the traveltime *differences* between waves recorded at the two receivers. Using the method of images (Brekhovskikh, 1960), we can show that these traveltime difference curves assume the form,

$$\delta\mathbf{t} = \frac{\sqrt{x_{r_j}^2 + (2b_{r_j}Z_1 \pm z_s \pm z_{r_j})^2}}{V_1} - \frac{\sqrt{x_{r_i}^2 + (2b_{r_i}Z_1 \pm z_s \pm z_{r_i})^2}}{V_1}, \qquad (2.4)$$

where $\delta\mathbf{t}$ is the traveltime difference; x_{r_i} and x_{r_j} are the horizontal distances from each source to receiver r_i and r_j, respectively; $b_{r_i}(b_{r_j})$ is the number of bounce points from the bottom reflecting interface to receiver $r_i(r_j)$ and the receivers are at depth $z_i(z_j)$; Z_1 is the depth of the interface; z_s is the depth of the source; and V_1 is the P-wave interval velocity of the medium (Figure 2.1). The sign of z_s is

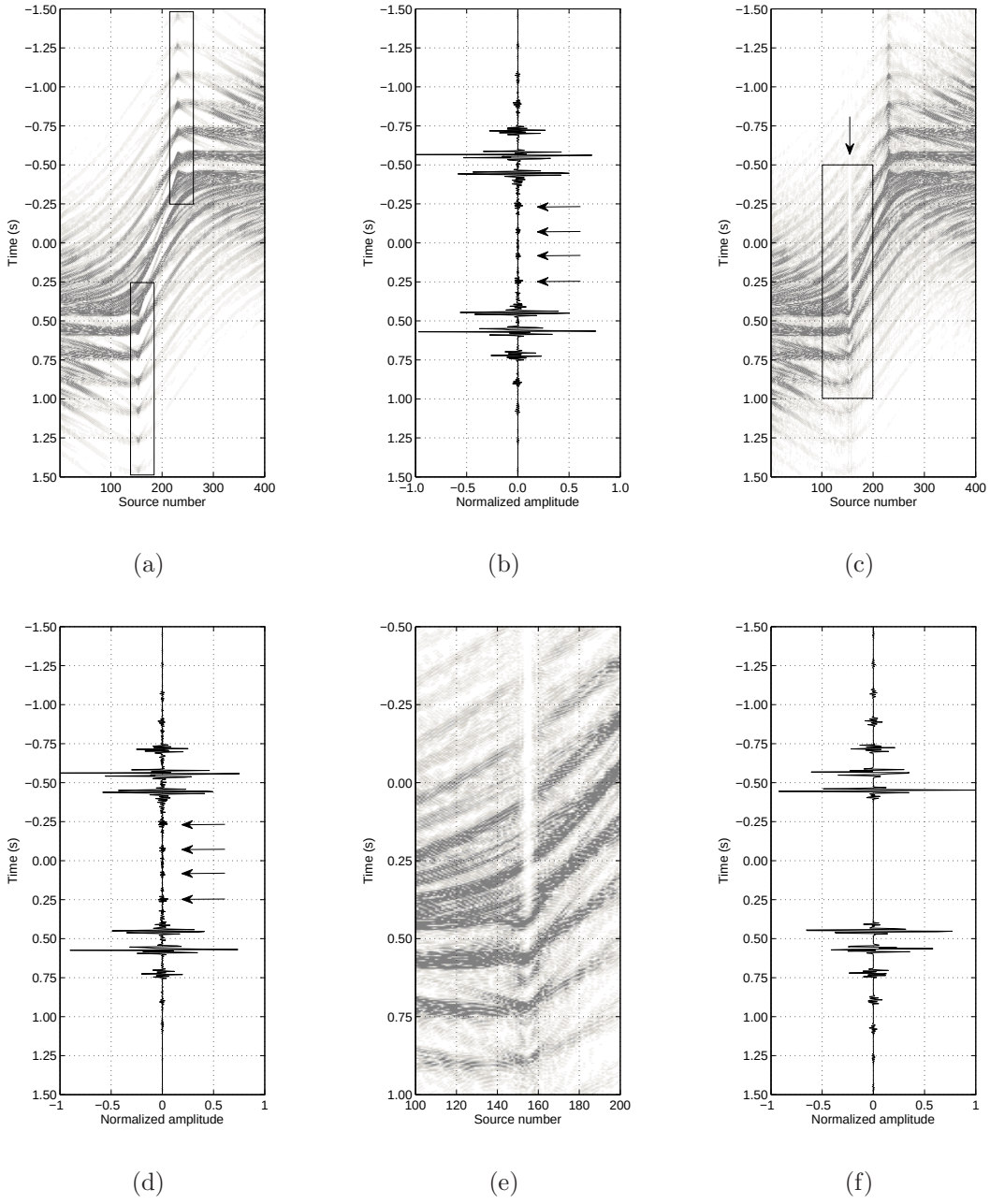

Figure 2.3: Interferometric Green's function estimates and true Green's function for the single layer over half-space model in Figure 2.1. (a) Correlation gather for receivers 1 and 151 showing arrivals between -1.5 s and 1.5 s. (b) Green's function estimate after summation over source position in (a). (c) Deconvolution gather for receivers 1 and 151. (d) Green's function after summation over source position in (c). In (b) and (d), arrows indicate some of the non-physical arrivals. (e) Close-up of the deconvolution gather showing arrivals within the box in (c). (f) True Green's function plus its time-reversed component.

negative when waves are downgoing from the source and positive when waves are upgoing. The sign of $z_{r_i}(z_{r_j})$ is negative when waves are upgoing at the receiver and positive when waves are downgoing. In the examples that follow, we set $i = 1$ and $j = 151$.

We now interpret the traveltime curves in the correlation gather using equation 2.4. For this, we assume that $Z_1 = 150$ m, $V_1 = 1500$ m/s and the reflected wavefields are downgoing at the source and upgoing at the receiver (i.e., the sign of z_s and $z_{r_i}(z_{r_j})$ is negative). The traveltime, which is composed of linear segments and which intersects the time axis at ± 0.4 s in Figure 2.4(a), highlights the energy in the direct arrival at r_{151} cross-correlated with the direct arrival at r_1, term C_1 in equation 2.3. Working downward in Figure 2.4(a), the next curve illustrates the traveltime for energy in the primary reflection at r_{151} cross-correlated with the direct arrival at r_1. The following curve displays the traveltime for energy in the first-order multiple at r_{151} cross-correlated with the direct arrival at r_1 and so on (the remaining curves are defined in the caption to Figure 2.4(a)). These curves are all associated with the term C_2 in equation 2.3. By contrast, we now calculate the traveltime curves by fixing the direct arrival at r_{151} and varying the number of bounce points to r_1. These traveltime curves are displayed in Figure 2.4(b) and are associated with the term C_3 in equation 2.3. Finally, we consider traveltime curves associated with term C_4. Figure 2.4(c) shows traveltime curves of reflected waves that have the same number of bounce points to each receiver. These curves have similar traveltime differences and hence are positioned closely together. Figure 2.4(d) displays the traveltime curves of reflected waves that have a differing number of bounce points to each receiver.

The V-shaped traveltime curves, associated with terms C_2 and C_3, correspond to the the causal and acausal reflections, respectively (Snieder et al., 2006b). The extrema of these curves (indicated by the boxes in Figure 2.3(a)) are termed stationary-phase points because the wave phase becomes stationary with respect

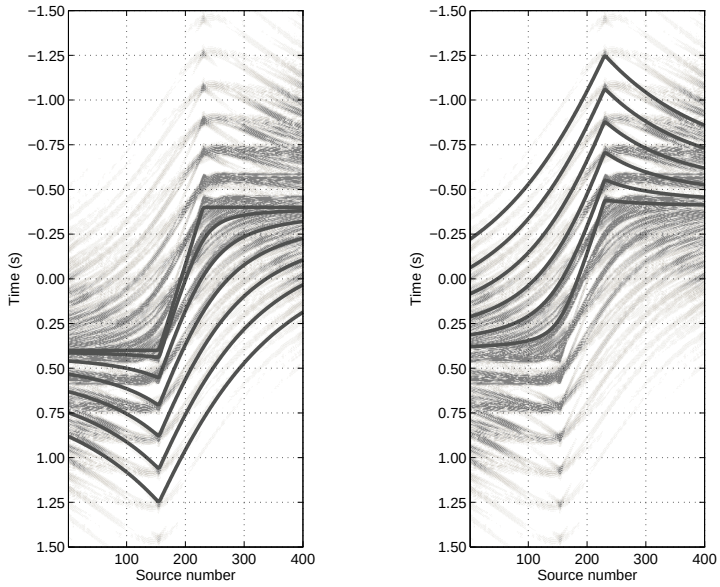

(a) (b)

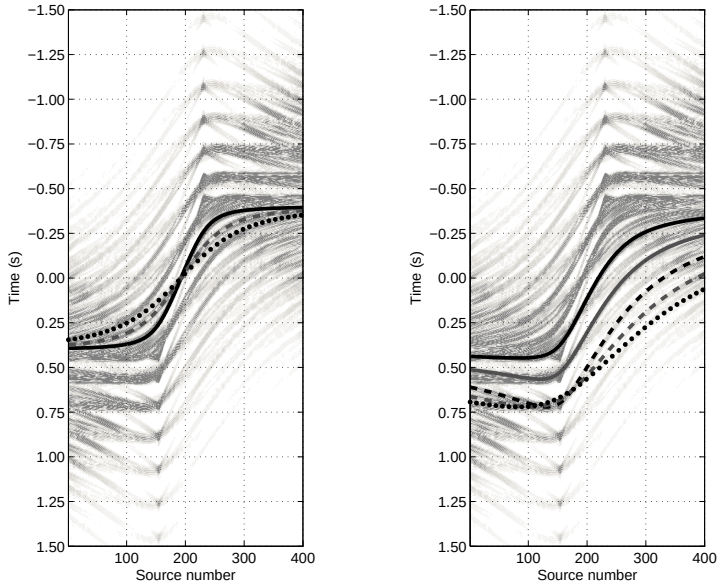

(c) (d)

Figure 2.4: Traveltime curves, calculated using equation 2.4, plotted on the correlation gather. D – Direct arrival; P – Primary arrival; M1 – first-order multiple (M2, M3, M4, M5, M6, and so on). Cross-correlations are expressed as DD, where the first letter refers to the direct arrival at r_{151} and the second letter refers to the direct arrival at r_1. Likewise, PD indicates cross-correlation of the primary arrival at r_{151} and with the direct arrival at r_1. (a) Working downward the traveltimes are as follows, DD, PD, M1D, M2D, M3D, M4D, and M5D. (b) Working upward the traveltimes are as follows, DP, DM1, DM2, DM3, DM4 and DM5. (c) Solid black: PP. Dashed gray: M1M1. Dotted black: M2M2 (d) Solid black: M1P. Solid gray: M2P. Dashed black: M3P. Dashed gray: M4M1. Dotted black: M5M2.

to the boundary source location. Several authors have analysed the contribution of stationary-phase points to interferometric integrands such as in equations 1.2 and 2.1 (Snieder, 2004; Sabra et al., 2005; Halliday and Curtis, 2008, 2009b). In the summation over sources (integration), if the amplitude of the energy does not vary rapidly with source position then energy around these stationary-phase points sums constructively whereas other energy sums destructively. Stationary energy thus provides the dominant contribution to the estimate of the true homogeneous Green's function on the left-hand side of equation 2.1. Consistently with previous studies, we therefore refer to the energy around these points (i.e., approximately between sources 150 and 160) as physical energy. Note that we also obtain stationary-phase points, associated with term C_4, that cluster to the left of the V-shaped traveltime curves (Figure 2.4(d)). Figure 2.5(a) shows a stationary-phase source which would contribute to the primary reflection between the receivers. However, there is a large proportion of energy contributing to term C_4 which is considered non-stationary and is therefore non-physical. Figure 2.5(b) shows two wavefields whose cross-correlation would contribute to a non-physical arrival. These wavefields are particularly problematic and will lead to non-physical endpoint contributions (Snieder et al., 2006b). In the velocity analysis procedure outlined in the next section we will show that the low-order multiples associated with term C_4 between sources 1 and 80 lead to predominantly non-physical energy,

$$G_{np}(\mathbf{x}_B, \mathbf{x}_A) + G^*_{np}(\mathbf{x}_B, \mathbf{x}_A) \approx \frac{2}{\rho c} \underbrace{\int_1^{80} G_r(\mathbf{x}_B, \mathbf{x}) G^*_r(\mathbf{x}_A, \mathbf{x}) d^2\mathbf{x}}_{C_4} \tag{2.5}$$

and can constrain the rms velocity and layer thickness.

(a) (b)

Figure 2.5: Two wavefields whose cross-correlation leads to a physical (a) and non-physical (b) arrival.

2.1.2 Interferometry by deconvolution

In certain situations, deconvolutional interferometry seems a more natural operation than cross-correlational interferometry because it removes much of the signature of non-impulsive boundary sources, leaving a relatively impulsive source signal in the Green's function estimate (Vasconcelos and Snieder, 2008b). Snieder et al. (2006a) show how deconvolution interferometry can be used to obtain the building response at different floors of a multi-storey structure compliant with different boundary conditions. Vasconcelos and Snieder (2008a) further develop the theory of deconvolution interferometry and outline an application related to seismic-while-drilling and imaging of the San Andreas fault in California, USA. (Vasconcelos and Snieder, 2008b).

With reference to Figure 2.1, deconvolutional interferometry for a one-dimensional medium is defined as follows,

$$D(\mathbf{x}_B, \mathbf{x}_A) = \oint_{\partial S} \frac{G(\mathbf{x}_B, \mathbf{x}) G^*(\mathbf{x}_A, \mathbf{x}) d^2\mathbf{x}}{|G(\mathbf{x}_A, \mathbf{x})|^2 + \varepsilon}. \tag{2.6}$$

where ε is a stabilization factor associated with the water-level deconvolution approach of Clayton and Wiggins (1976). Vasconcelos and Snieder (2008a) show that when $|G_d|^2 \gg |G_r|^2$ (i.e., the power spectrum of the direct arrival is much greater than the power spectrum of the reflected wavefield), equation 2.6

reduces to three terms, D_1, D_2 and D_3, respectively. The terms D_1 and D_2 are analogous to C_1 and C_2 in cross-correlational interferometry. The term D_3 is associated with non-physical arrivals that Vasconcelos and Snieder (2008a) term free-point scattered waves. The obvious difference between equations 2.1 and 2.6 is that in equation 2.6, we divide the numerator by the power spectrum of the Green's function at $\mathbf{x}_A$. Thus, any appreciable source wavelet (that would be convolved with the Green's functions on both sides of equation 2.1) is removed in equation 2.6 by division in the frequency domain. If the factor ε is too large, equation 2.6 simply approximates scaled cross-correlation interferometry. Conversely, the deconvolution will become unstable for any frequency with little signal power if ε is too small. Hence, in deconvolutional interferometry there exists a trade-off between stabilization and resolution determined by the factor ε, a trade-off that is not present in cross-correlation interferometry.

We define a second interferometric gather, the deconvolution gather, as the set of integrands contributing to the integral of equation 2.6 between a fixed receiver pair (i.e., at $\mathbf{x}_A$ and $\mathbf{x}_B$) as a function of source position $\mathbf{x}$. Figure 2.3(c) shows the deconvolution gather for receivers 1 and 151, and Figure 2.3(d) displays the Green's function estimate. In this instance, the deconvolution gather seems comparable to the correlation gather. However, there is one important difference indicated by the arrow in Figure 2.3(c). Figure 2.3(e) shows a close-up of this region. Now consider Figure 2.6 which displays $|G_d|^2/|G_r|^2$ (i.e., the power spectrum of the direct arrival divided by the power spectrum of the reflected wavefield). In this region between source numbers 152 and 156 (gray contours), the requirement that $|G_d|^2 \gg |G_r|^2$ holds and we achieve only causal reflected waves (i.e., term D_2 in Figure 2.3(e)) as expected by theory (Vasconcelos and Snieder, 2008a). As a point of note, these particular sources are positioned at and around the stationary-phase points for causal reflected waves. Outside this region however, the source ghost (i.e., the wavefield that travels from the source

into the subsurface via a single reflection at the free surface) significantly reduces the amplitude of the direct arrival. Hence, the requirement that $|G_d|^2 \gg |G_r|^2$ is no longer valid (Figure 2.6). This results in causal and acausal contributions that have phase similar to that of the arrivals in the correlation gather.

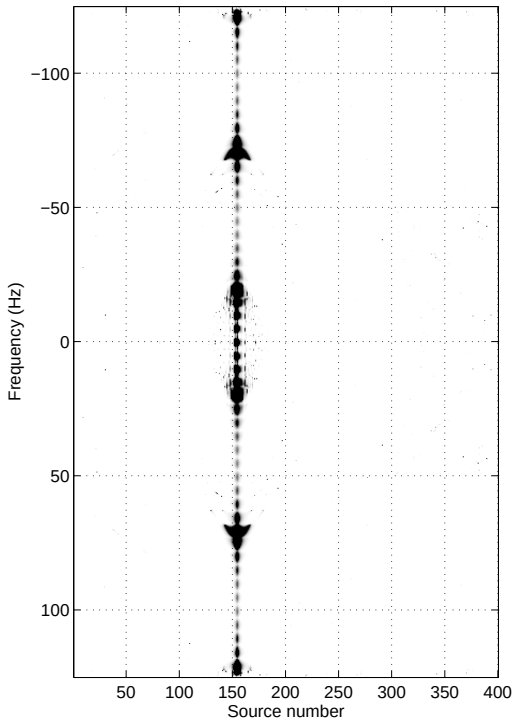

Figure 2.6: The power spectrum of the direct arrival at r_1 divided by the power spectrum of the reflected wavefield at r_1 (i.e., $|G_d(r_1)|^2/|G_r(r_1)|^2$).

A non-physical arrival exists in the deconvolution gather (Figure 2.7(a)) that is not present in the correlation gather (Figure 2.7(b)). We believe that the isolated arrival at 0.62 s and around source number 155 in the deconvolution gather is a type 2 free-point ghost (Vasconcelos and Snieder, 2008a) as defined in Figure 2.8(a). The raypath of a type 2 free-point ghost leads to an arrival time of $t = 2t_1 + t_2$ (Figure 2.8(a)). Assuming vertical incidence,

$$t_1 = (Z_1 - z_{r_j})/V_1 \tag{2.7}$$

and

$$t_2 = \frac{\sqrt{(x^2 + 4(Z_1 - z_{r_j})^2)}}{V_1} \tag{2.8}$$

where x is the horizontal distance between the two receivers, t=2*0.09 + 0.44 = 0.62 s. The expected arrival time t corresponds well to the onset of the non-physical arrival in Figure 2.8(b).

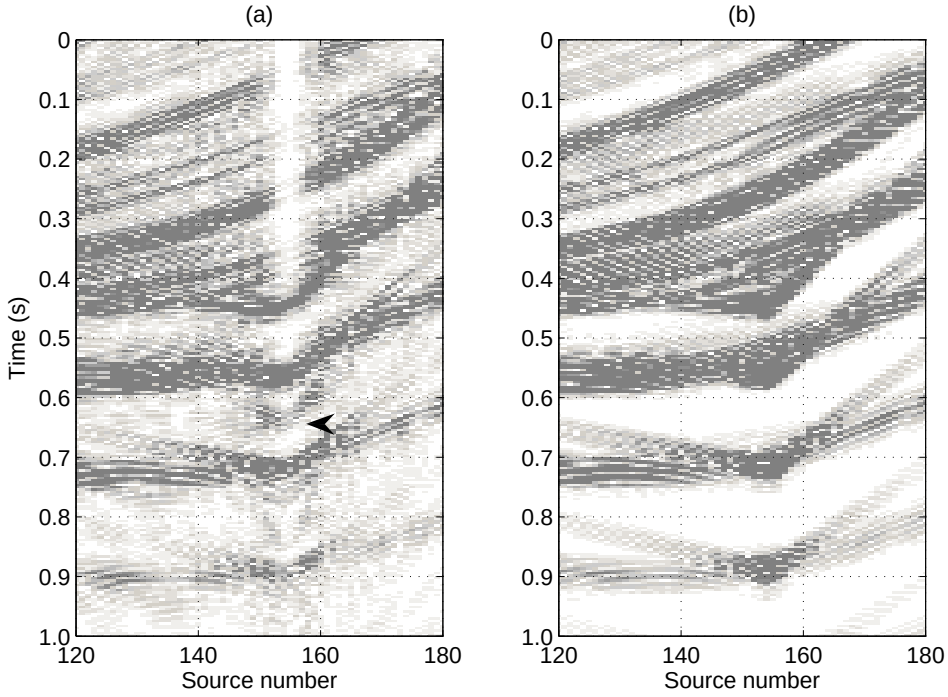

Figure 2.7: (a) Close-up of the deconvolution gather in Figure 2.3(c) and (b) close-up of the correlation gather in Figure 2.3(a). The arrowhead in (a) denotes one non-physical arrival.

As the deconvolution gather approximates that of the cross-correlation gather, we limit our presentation of the velocity analysis procedure, described in the next section, to the correlation gathers only. However, tests show that the method works just as well for deconvolution gathers.

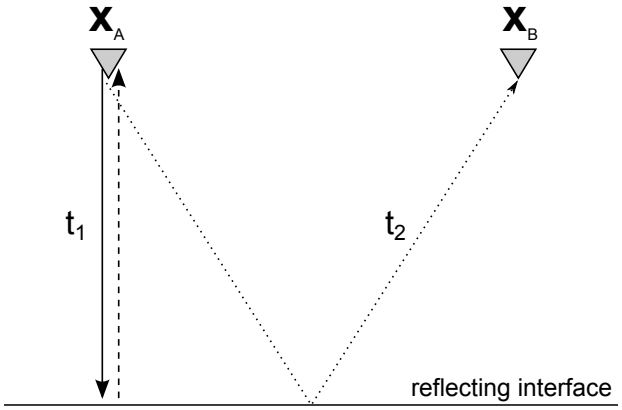

(a)

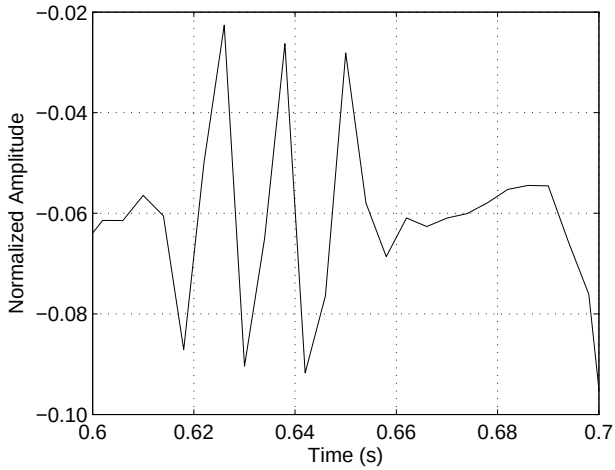

(b)

Figure 2.8: (a) The traveltime path of a type 2 free-point ghost. The expected arrival time of a type 2 free-point ghost is $t = 2t_1 + t_2$. (b) A time-slice of Figure 2.7(a) showing the arrival at source number 155 between 0.6 s and 0.7 s.

2.2 Interferometric velocity analysis

For field data, we know the source-receiver geometry and treat both Z_1 and V_1 as unknowns. For different values of Z_1, V_1, b_{r_i}, and b_{r_j}, we calculate the traveltime difference curves using equation 2.4 and then measure the signal coherency along each curve in the correlation gather. The aim of interferometric velocity analysis is to find a velocity and layer-thickness estimate that gives the highest coherency of signal along the specified traveltime difference curves. In the following examples, we compute equation 2.4 by assuming that wavefields are downgoing at the source and upgoing at the receivers (we do not explicitly decompose the measured

wavefield into its upgoing and downgoing components, but this could be done). As a coherency measure, we use a modified version of semblance S_c (Neidell and Taner, 1971), which is defined as the normalized output (E^{out}) to input (E^{in}) energy,

$$S_c = \frac{1}{(b_{r_1} \cdot b_{r_{151}})} \sum_{i=1}^{b_{r_1}} \sum_{j=1}^{b_{r_{151}}} \frac{E^{out}_{i,j}}{N \cdot E^{in}_{i,j}} \qquad 0 \leq S_c \leq 1, \tag{2.9}$$

where N is the number of sources or 'traces' in the correlation gather, and the output energy E_{out} and input energy E_{in} are defined as,

$$E^{out}_{i,j} = \sum_{t(k)=\delta\mathbf{t}-t/2}^{\delta\mathbf{t}+t/2} \left\{ \sum_{l=1}^{N} f_{i,j,l,t(k)} \right\}^2 \tag{2.10}$$

and

$$E^{in}_{i,j} = \sum_{t(k)=\delta\mathbf{t}-t/2}^{\delta\mathbf{t}+t/2} \sum_{l=1}^{N} f^2_{i,j,l,t(k)}, \tag{2.11}$$

where f is a function of Z_1, V_1, b_{r_1}, and $b_{r_{151}}$ and is the amplitude value at the lth source at time $\delta\mathbf{t}$ within a time window $[-t/2\ t/2]$. After summation over the number of bounce points and number of sources we obtain a 2D spectrum in velocity and layer thickness. Note that in equations 2.9–2.11 we only consider wavefields with $b_{r_i}(b_{r_j}) \geq 1$ and hence, the traveltime difference curves correspond to term C_4 in equation 2.3.

We first consider the velocity-layer thickness spectra computed using all 400 sources in equations 2.9–2.11. Figure 2.9(a) shows the velocity-layer-thickness spectrum computed using energy up to the first-order multiples ($b_{r_i} = b_{r_j} = 2$) in the correlation gather, and Figure 2.9(b) displays the same plot computed up to the third-order multiples ($b_{r_i} = b_{r_j} = 4$). It is clear that by increasing the order of multiples in the semblance computation, Figure 2.9(b) clarifies which is the single, correct peak, which lies close to the true value of velocity and layer thickness.

Estimation of the correct parameters may be improved by using a different

combination of interferometric arrivals. In the work of Mikesell and van Wijk (2011), a semblance analysis using the interferometric refractions provides an elongated peak which dips from top right to bottom left. This is the oppposite direction to the elongated peak obtained in Figure 2.9. It seems reasonable to suggest that if the two approaches were combined, the peaks would cross allowing a more accurate estimate of velocity and layer thickness to be obtained.

We now consider using only the first 80 sources in equations 2.9–2.11 (contributing predominantly non-physical energy to the interferometric integrand in equation 2.1). For a typical marine survey, this represents the data geometries commonly recorded. In Figure 2.10(a) and 2.10(b), we display the velocity-layer thickness spectra for energy up to the first-order multiples ($b_{r_i} = b_{r_j} = 2$) and third-order multiples ($b_{r_i} = b_{r_j} = 4$), respectively. By incorporating a higher number of multiples in Figure 2.10(b), we achieve a more accurate estimate of velocity and layer thickness.

At first glance, the spectra in Figures 2.9 and 2.10 appear very similar. However, careful attention should be turned toward the coherency values (scalebars) in both figures. The maximum coherency value in Figure 2.10, using only 80 sources, is more than three times as large as the maximum coherency value of the respective semblance when all 400 sources are considered, in Figure 2.9. This implies that by using fewer sources, positioned at the end points of the source boundary, which predominantly contribute to non-physical interferometric arrivals, we achieve a better-defined velocity and layer-thickness estimate. This result appears non-intuitive; however, it may arise because for multiples, the interferometric wavefield diverges for sources positioned in the non-stationary region (see Figure 2.4(d)). Thus, the contribution from these arrivals may be emphasized when only these sources are considered in the semblance computation. Moreover, note that the first 80 sources are positioned at far offset from both receivers and hence, the method works for long-offset seismic reflection data. Thus, we have shown our

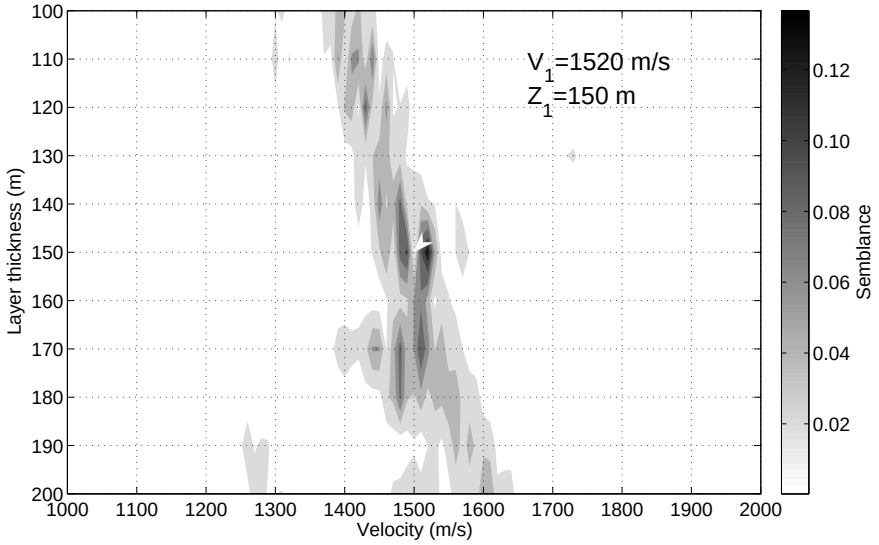

(a)

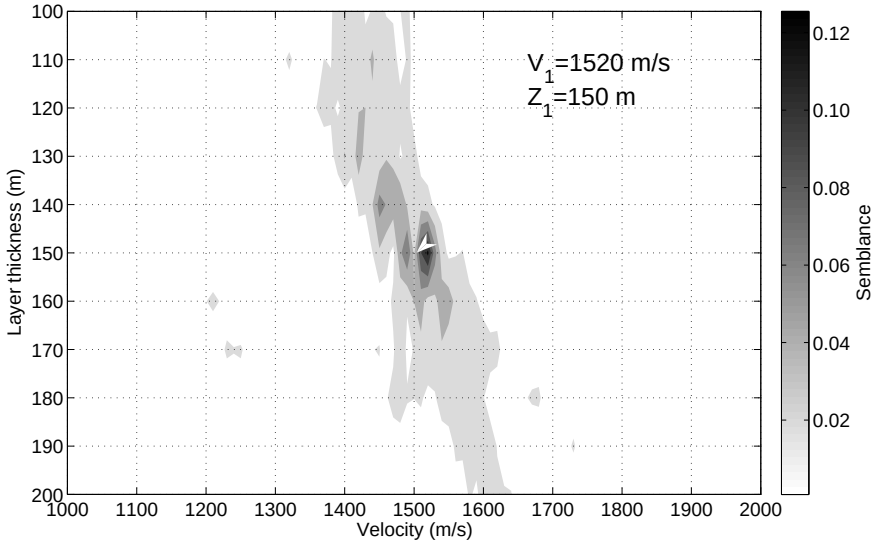

(b)

Figure 2.9: Spectra computed from the correlation gather in Figure 2.3(a). The velocity V_1 spans from 1000 to 2000 m/s and increments every 10 m/s. The layer thickness Z_1 spans from 100 to 200 m and increments every 10 m. We use a time window of 10 ms. In each of the following spectra we indicate the true value of velocity and layer thickness with an arrowhead and display the user-picked velocity-thickness pair in the upper right-hand corner. (a) Semblance computed using all 400 sources and energy up to the first-order multiples ($b_{r_i} = b_{r_j} = 2$). (b) As for (a) but computed using energy up to the third-order multiples ($b_{r_i} = b_{r_j} = 4$).

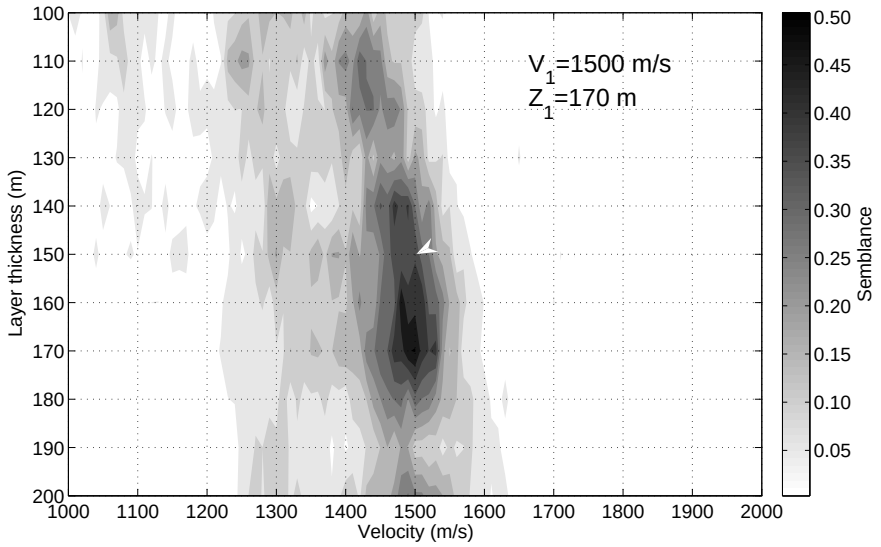

(a)

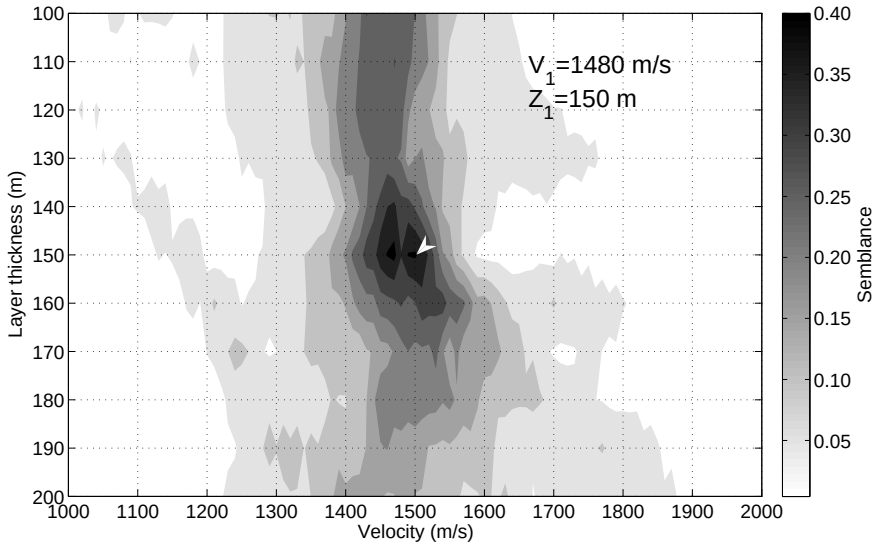

(b)

Figure 2.10: Spectra computed using predominantly non-physical energy from the correlation gather in Figure 2.3(a). We use the same parameters for V_1, Z_1 and t (time window) as in Figure 2.9. (a) Semblance computed using the first 80 sources and energy up to the first-order multiples ($b_{r_i} = b_{r_j} = 2$). (b) As for (a) but computed using energy up to the third-order multiple ($b_{r_i} = b_{r_j} = 4$).

method, unlike many interferometric imaging applications (e.g., Schuster et al. (2004)) that require wavefields to be excited at stationary-phase locations, to be accurate for sources positioned in the non-stationary region and also at long-

offset.

2.2.1 Multi-layered model

We now describe interferometric velocity analysis in a multi-layered Earth. Figure 2.11 shows a sketch of the acoustic multi-layered model and acquisition geometry. Each receiver now records the monopolar response for a total of 3.5 s at sample rate of 4 ms. Figure 2.12(a) shows the shot gather from source 1 and Figure 2.12(b) shows the shot gather from source 200. The primary reflections from the first, second and third interface ($P1$, $P2$, and $P3$) are annotated in Figure 2.12(b).

Because we are primarily interested only in reflected waves (i.e., $b_{r_i}(b_{r_j}) \geq 1$ in equations 2.9–2.11), we model the direct arrival in a homogeneous medium (with the velocity and density of layer 1) and subtract the result from each common shot gather prior to performing interferometry by cross-correlation. Hence, terms such as C_1, C_2 and C_3 in equation 2.3 are not present in any subsequent cross-correlational interferometric estimate. This step was not necessary in the single-layer model described in the previous section but may be advisable when more complex models such as this one are considered. Figure 2.13(a) shows the correlation gather, Figure 2.13(b) displays the corresponding Green's function estimate, and Figure 2.13(c) shows the true Green's function. For comparison, Figure 2.13(d) show the correlation gather for the single-layer model which has been processed minus the direct arrivals.

The correlation gather in Figure 2.13(a) is more complicated than that in Figure 2.13(b). As any significant energy occurs at the traveltime differences between waves recorded at the receiver pair, energy from deeper layers may arrive at the same time as energy from shallow layers and therefore mask that energy. This makes an interpretation of arrivals such as those depicted in Figure 2.4, more difficult in the multilayer case. Nevertheless, we can still identify similar

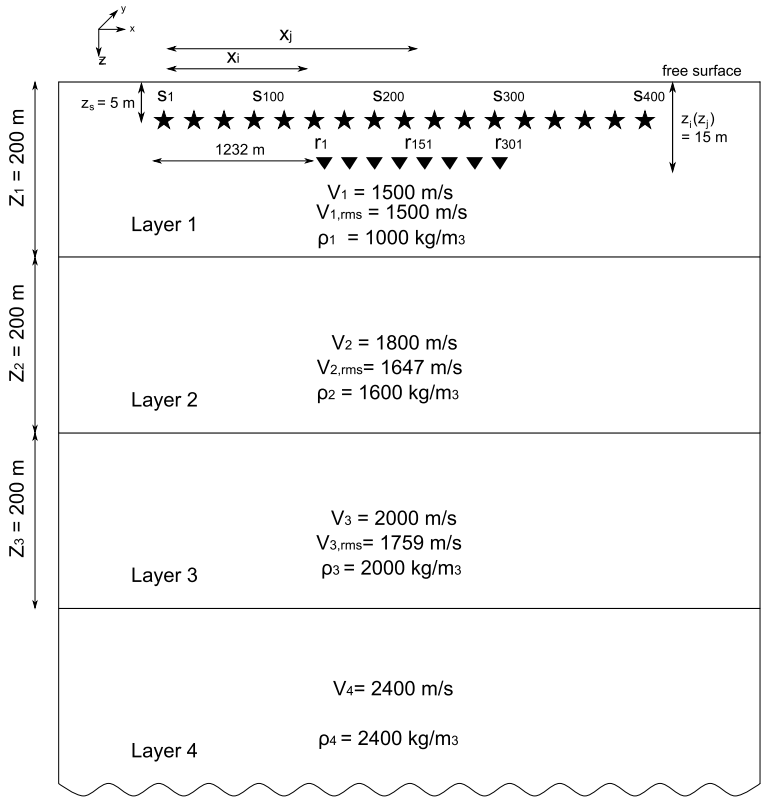

Figure 2.11: Model consisting of four homogeneous layers separated by three interfaces positioned at 200 m intervals. The interval velocities (V_1,...,V_4), rms velocities ($V_{1,rms}$,...,$V_{3,rms}$) and densities (ρ_1,...,ρ_4) are shown. The acquisition geometry is the same as in Figure 2.1.

features such as the stationary-phase and non-stationary regions.

When we have a sequence of layers, we adopt a 'layer-stripping' approach. As we now consider a multi-layered model, any velocity estimate will be the rms velocity. We determine the rms velocity and thickness of each layer in turn, beginning at the surface and progressing with depth. In the final step, these estimates are converted to interval velocities. Let us first consider $V_{1,rms}$ and Z_1 of layer 1. The traveltime moveout formula due to the interference of wavefields in layer 1 is expressed in equation 2.4. We adopt the same approach to calculate semblance as described in the previous section, for the time being ignoring energy in the gather from the interference of wavefields from layers 2 and 3.

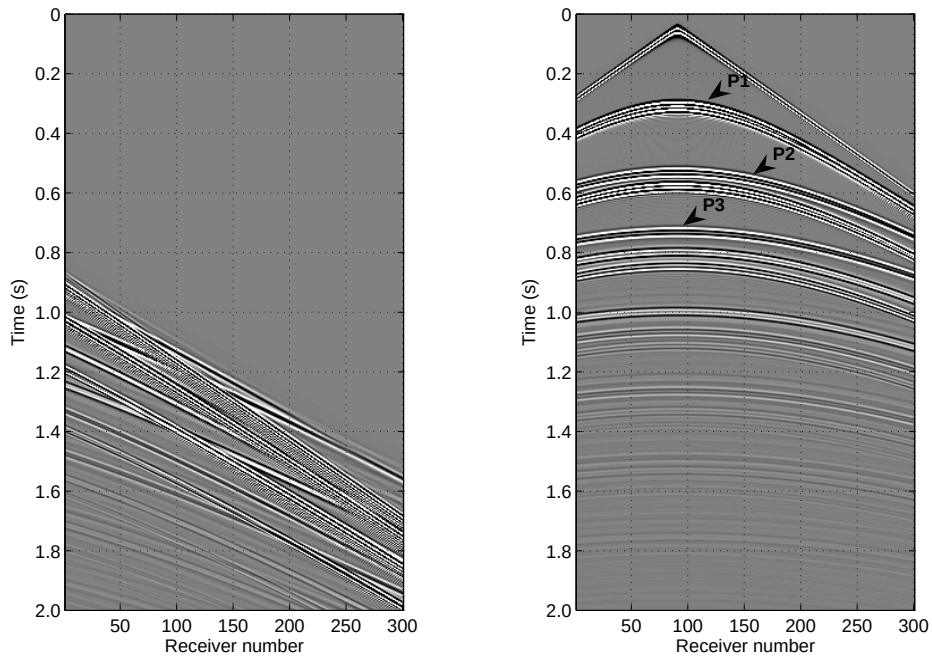

(a) (b)

Figure 2.12: Shot gathers from source 1 (a) and 200 (b) in Figure 2.11.

Figure 2.14(a) displays the rms velocity-layer 1 thickness spectrum calculated using all 400 sources in the correlation gather, and Figure 2.14(b) shows the corresponding spectrum calculated using only the first 80 sources. To reduce the impact of arrivals from deeper layers, we consider only multiples up to first order ($b_{r_i} = b_{r_j} = 2$). In Figure 2.14(a), we achieve four peaks positioned close to the correct values of velocity and layer thickness. However, by considering fewer sources, those that contribute predominantly non-physical energy, we obtain a single peak with a higher coherency estimate than when all sources are included (note the scalebar in Figure 2.14(a) and 2.14(b)).

We now investigate the velocity $V_{2,rms}$ and layer thickness Z_2 of layer 2 (Figure 2.11). We assume that the dominant wavefield contributions in interferometry will occur when the high amplitude free-surface reflections from layer 1 are cross-correlated with reflections from layer 2. These arrivals are termed spurious multiples by Snieder et al. (2006b) and would vanish at the stationary-

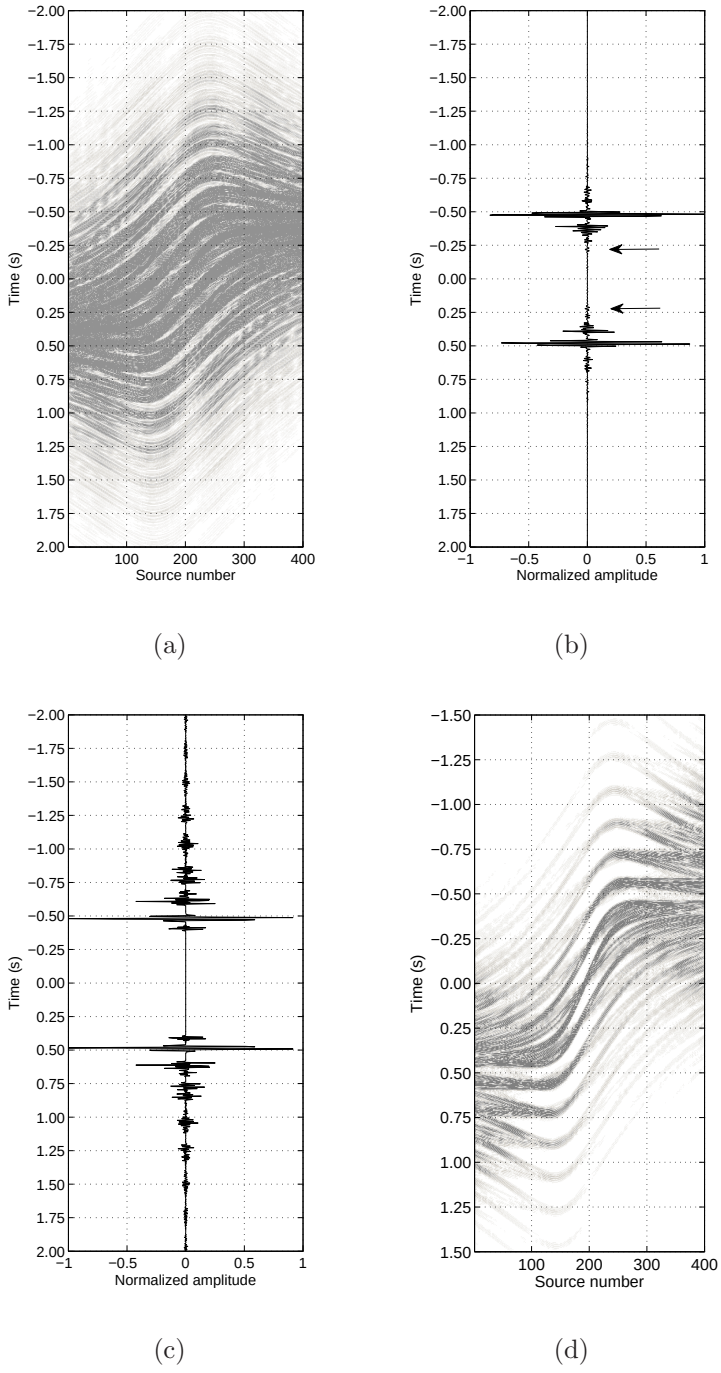

Figure 2.13: Interferometric Green's function estimates and true Green's function for the multi-layered model in Figure 2.11. (a) Correlation gather for receivers 1 and 151 showing arrivals between -2 s and 2 s. (b) Green's function estimate after summation over source position in (a). Arrows denote non-physical arrivals. (c) True Green's function plus its time-reversed component. (d) Correlation gather for single-layer model processed minus the direct arrivals. For comparison, see the full wavefield correlation gather in Figure 2.3(a).

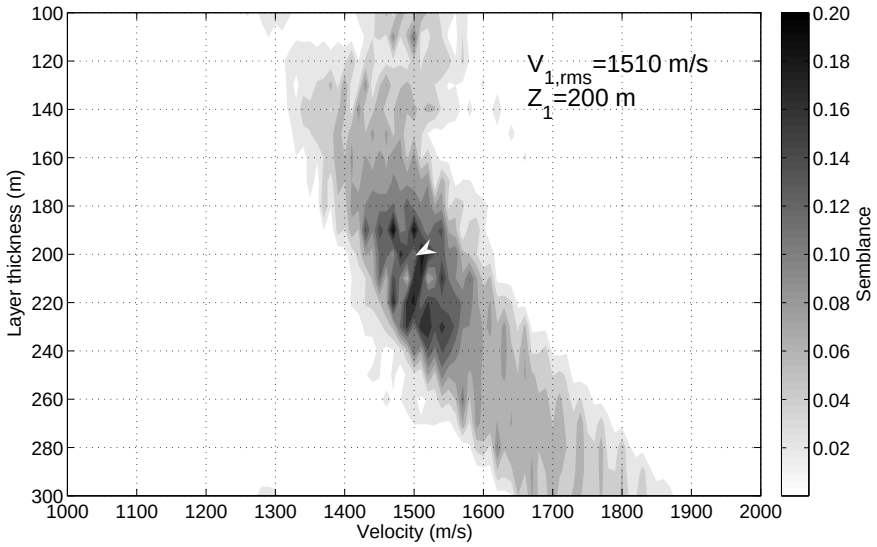

(a)

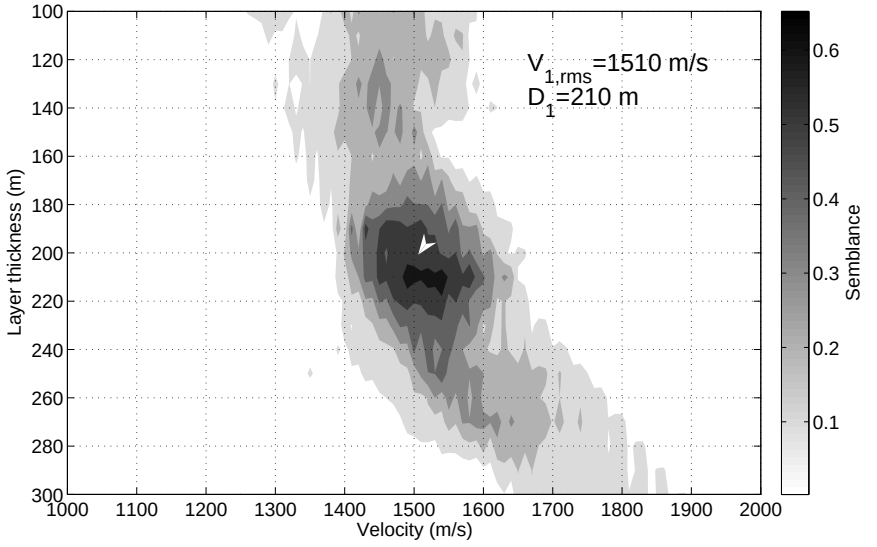

(b)

Figure 2.14: Spectra showing $V_{1,rms}$ against Z_1. The velocity $V_{1,rms}$ spans from 1000 to 2000 m/s and increments every 10 m/s. The layer thickness Z_1 spans from 100 to 300 m and increments every 10 m. We use a time window of 20 ms. (a) Semblance computed from the correlation gather (Figure 2.13(a)) using all 400 sources and energy up to the first-order multiples. (b) As for (a) but using only the first 80 sources.

phase point given a source boundary below the reflectors. Hence, we assume that

significant energy in Figure 2.13(a) will have an arrival time equal to

$$\delta \mathbf{t} = T_2^{k,l} - T_1^m, \tag{2.12}$$

where $T_2^{k,l}$ is the arrival time of a reflection with k bounces in layer 1 and l bounces in layer 2 and T_1^m is the arrival time of a reflection with m bounces from layer 1. The important aspect about the moveout formula in equation 2.12, is the fact that we have an estimate of the parameters of T_1^m (i.e., we have found $V_{1,rms}$ and Z_1 as displayed in Figure 2.14). Hence, the moveout formula varies with respect to the first term $T_2^{k,l}$ which depends on the unknowns $V_{2,rms}$ and Z_2.

In Appendix 1, we derive the traveltime equation for multiple raypaths in a multi-layered model and show that the traveltime $T_2^{k,l}$ assumes the form

$$t = t_{0_{mult}}\left(1 - \frac{1}{S}\right) + \sqrt{\left(\frac{t_{0_{mult}}}{S}\right)^2 + \frac{x_{r_j}^2}{SV_{rms}^2}} \tag{2.13}$$

where $t_{0_{mult}} = 2\sum_{k=1}^{M} b_{k,r_j} Z_k / V_k$, b_{k,r_j} is the number of bounce points in the kth layer to the jth receiver, Z_k is the layer thickness, V_k is the interval velocity, M is the number of layers and S is a constant sometimes referred to as the inhomogeneity factor. Equation 2.13 is accurate for long-offset seismic reflection data. Substituting the traveltimes in equations 2.4 and 2.13 into the traveltime difference formula in equation 2.12 we obtain

$$\delta \mathbf{t} = \underbrace{t_{0_{mult}}\left(1 - \frac{1}{S}\right) + \sqrt{\left(\frac{t_{0_{mult}}}{S}\right)^2 + \frac{x_{r_j}^2}{SV_{rms}^2}}}_{T_2} - \underbrace{\frac{\sqrt{x_{r_i}^2 + (2b_{r_i}Z_1 \pm z_s \pm z_{r_i})^2}}{V_{1,rms}}}_{T_1}. \tag{2.14}$$

We take $M = 2$ (the total number of layers in term T_2). Similar to what is

described in the previous section, for different values of b_{r_i} in T_1, b_{k,r_j} in T_2 and different estimates of $V_{2,rms}$ and Z_2 we compute the traveltime difference curves as defined by equation 2.14. For each curve we find the signal coherency in the correlation gather. As we consider a further set of raypaths in layer 2 (determined by $b_{2,r_{151}}$), we redefine semblance as

$$S_c = \frac{1}{(b_{r_1} \cdot b_{1,r_{151}} \cdot b_{2,r_{151}})} \sum_{i=1}^{b_{r_1}} \sum_{j=1}^{b_{1,r_{151}}} \sum_{m=1}^{b_{2,r_{151}}} \frac{E^{out}_{i,j,m}}{N \cdot E^{in}_{i,j,m}} \qquad 0 \leq S_c \leq 1, \tag{2.15}$$

where

$$E^{out}_{i,j,m} = \sum_{t(k)=\delta\mathbf{t}-t/2}^{\delta\mathbf{t}+t/2} \left\{ \sum_{l=1}^{N} f_{i,j,m,l,t(k)} \right\}^2 \tag{2.16}$$

and

$$E^{in}_{i,j,m} = \sum_{t(k)=\delta\mathbf{t}-t/2}^{\delta\mathbf{t}+t/2} \sum_{l=1}^{N} f^2_{i,j,m,l,t(k)}. \tag{2.17}$$

We take $V_{1,rms} = 1510$ m/s and $Z_1 = 210$ m since these values correspond to a single peak with maximum coherency in Figure 2.14(b). Figure 2.15(a) displays the rms velocity-layer 2 thickness spectrum computed using all 400 sources and for $b_{r_i} = b_{k,r_j} = 2$ in each layer to each receiver, and Figure 2.15(b) displays the corresponding spectrum computed using the first 80 sources (i.e., using the predominantly non-physical energy). In both figures we obtain a distinct peak at velocities of 1640 m/s and 1680 m/s. By using all sources we achieve a prominent peak at the correct rms velocity and thickness of layer 2. By using purely the non-physical energy we achieve a less well-constrained but more coherent estimate of the subsurface parameters of layer 2. Notice that in both figures, we still obtain a strong peak with the velocity 1500 m/s of layer 1. This occurs because the correlation gather contains a variety of interfering wavefields. Although the traveltime equation 2.13 is designed to isolate the parameters of layer 2, it is entirely conceivable that the strongest interfering wavefields from layer 1 will have similar traveltimes and therefore the corresponding velocity will occur in

the semblance estimate. Furthermore, it is likely that the peak at 1800 m/s in Figure 2.15(a) is derived from the interfering wavefields from layer 3.

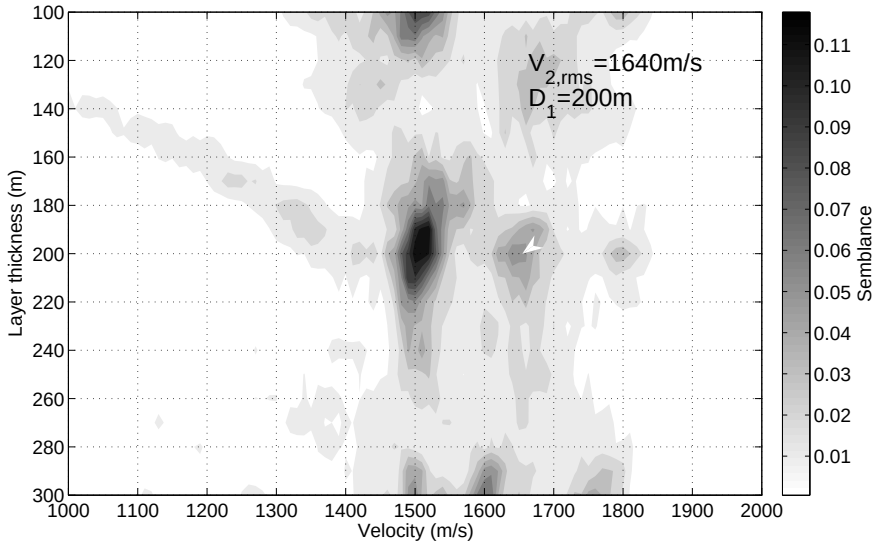

(a)

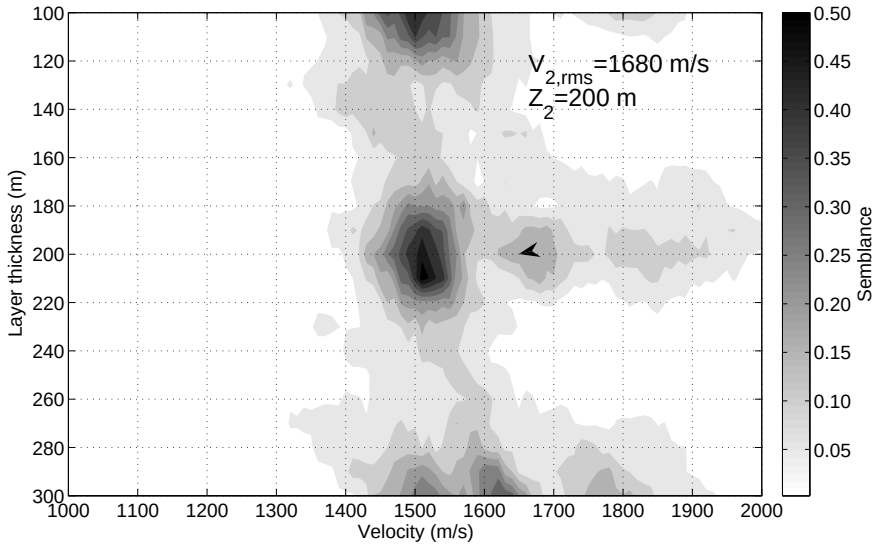

(b)

Figure 2.15: Spectra showing $V_{2,rms}$ against Z_2. We assume that velocity increases with depth and hence, we choose $V_{2,rms}$ to vary from 1000 to 2000 m/s and increments every 10 m/s. The layer thickness Z_2 spans from 100 to 300 m and increments every 10 m. We use a time window of 20 m/s. (a) Semblance computed using all 400 sources in the correlation gather and for $b_{r_i} = b_{k,r_j} = 2$ in each layer. (b) As for (a) but using only the first 80 sources.

Finally, we consider the velocity $V_{3,rms}$ and layer thickness Z_3 of Layer 3. As

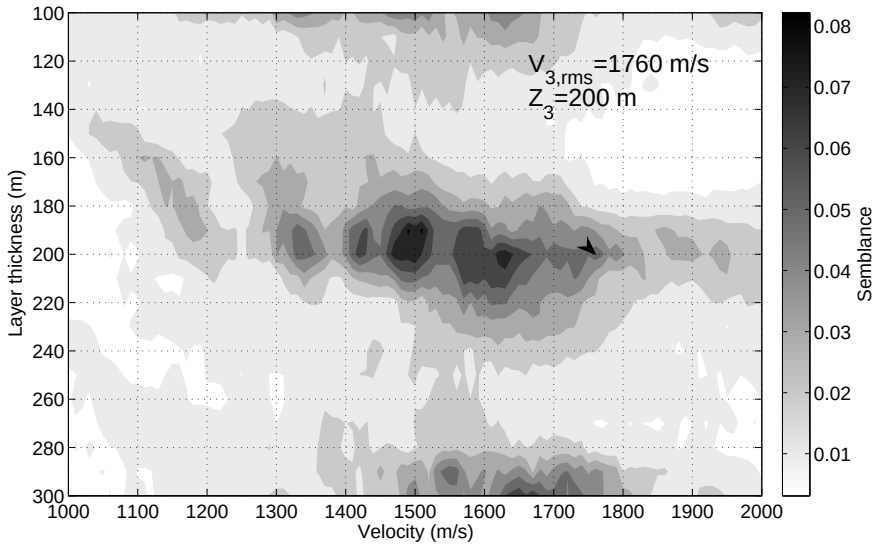

(a)

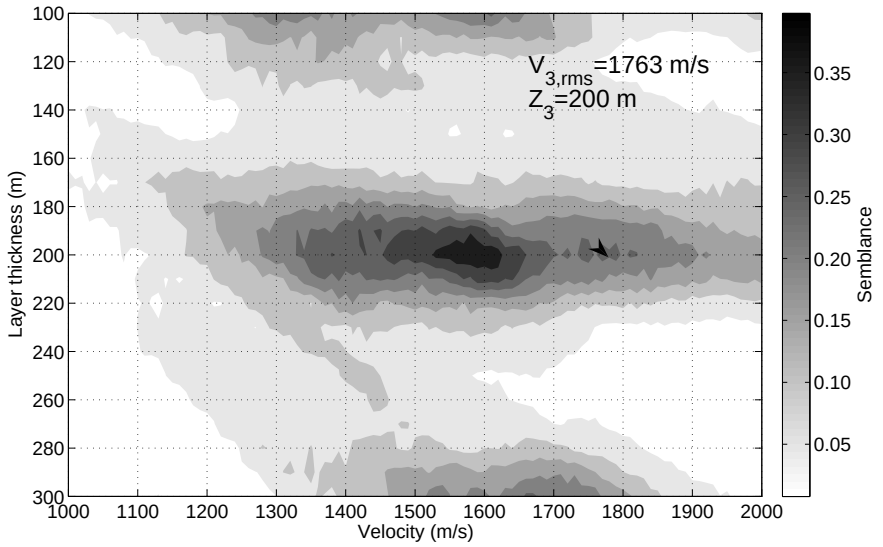

(b)

Figure 2.16: Spectra showing $V_{3,rms}$ against Z_3. The velocity $V_{3,rms}$ spans from 1000 to 2000 m/s and increments every 10 m/s. The layer thickness Z_3 spans from 100 to 300 m and increments every 10 m. We use a time window of 20 m/s. (a) Semblance computed using all 400 sources in the correlation gather and for $b_{r_i} = b_{k,r_j} = 2$ in each layer. (b) As for (a) but using only the first 80 sources.

before, we assume that the dominant contributions will occur when free-surface reflections from layer 1 are cross-correlated with reflections from layer 3. We now take the number of layers $M = 3$ in equation 2.14. We assume the same values

Table 2.1: Estimated velocity and layer thickness results with true values for comparison.

Layer	Estimated $V_{k,rms}$ (m/s)	True $V_{k,rms}$ (m/s)	Estimated Z_k (m)	True Z_k (m)	Estimated V_k (m/s)	True V_k (m/s)
1	1510	1500	210	200	1510	1500
2	1660	1647	200	200	1804	1800
3	1763	1759	200	200	1957	2000

for $V_{1,rms}$ and Z_1 as before but now take $V_{2,rms}$=1660 m/s and Z_2=200 m, the average values of the two prominent peaks in Figure 2.15. We redefine Semblance as

$$S_c = \frac{1}{(b_{r_1} \cdot b_{1,r_{151}} \cdot b_{2,r_{151}} \cdot b_{3,r_{151}})} \sum_{i=1}^{b_{r_1}} \sum_{j=1}^{b_{1,r_{151}}} \sum_{m=1}^{b_{2,r_{151}}} \sum_{n=1}^{b_{3,r_{151}}} \frac{E^{out}_{i,j,m,n}}{N \cdot E^{in}_{i,j,m,n}} \qquad 0 \leq S_c \leq 1, \tag{2.18}$$

where

$$E^{out}_{i,j,m,n} = \sum_{t(k)=\delta\mathbf{t}-t/2}^{\delta\mathbf{t}+t/2} \left\{ \sum_{l=1}^{N} f_{i,j,m,n,l,t(k)} \right\}^2 \tag{2.19}$$

and

$$E^{in}_{i,j,m,n} = \sum_{t(k)=\delta\mathbf{t}-t/2}^{\delta\mathbf{t}+t/2} \sum_{l=1}^{N} f^2_{i,j,m,n,l,t(k)}. \tag{2.20}$$

Figure 2.16(a) displays the rms velocity-layer 3 thickness spectrum for all 400 sources and for $b_{r_i} = b_{k,r_j} = 2$ in each layer to each receiver. Figure 2.16(b) displays the corresponding spectrum for the first 80 sources (i.e., using the predominantly non-physical energy). The velocity interpretation is less clear than in Figures 2.14 and 2.15. In Figure 2.16(a) we obtain very strong peaks relating to the velocities of layer 1 and layer 2. However, given our previous interpretation we may assume that the strong peaks at the far right between 1700 m/s and 1800 m/s are related to the parameters of layer 3. In Figure 2.16(b), we find that by using the predominantly non-physical energy we obtain two prominent peaks between 1700 m/s and 1800 m/s compared to the case when all 400 sources are considered.

Table 2.1 provides a summary of the selected rms velocities V_{rms} and layer thicknesses Z. We convert these estimates to interval velocity using a similar formula to the Dix equation (Dix, 1955),

$$V_k = \sqrt{\frac{V_{k,rms}^2 D_k - V_{k-1,rms}^2 D_{k-1}}{D_k - D_{k-1}}}, \tag{2.21}$$

where V_k is the interval velocity and D_k is the depth from the free surface to the kth layer. In this form, equation 2.21 may be sensitive to inaccurate rms velocities. However, methods exist, such as that outlined by Koren and Ravve (2006), that constrain the inversion in the least-squares sense. It should be noted that in equation 2.21, and in our analysis so far, we use depths and not two-way traveltimes as expected by the classical Dix formula (Dix, 1955). Given an arbitrary velocity variation, consider the result when we average the rms velocity in time (Appendix 1):

$$V_{rms}^2(t) = \frac{1}{t}\int_0^t V^2(t)dt = \mu_2. \tag{2.22}$$

Now consider the result when we average with respect to depth,

$$V_{rms}^2(z) = \frac{1}{z}\int_0^z V^2(z)dz = \frac{\int_0^t V^3(t)dt}{\int_0^t V(t)dt} = \frac{\mu_3}{\mu_1}. \tag{2.23}$$

We define the inequality

$$\mu_3 \geq \mu_2^{3/2} \geq \mu_1^3, \tag{2.24}$$

which is valid for any inhomogeneous vertically varying medium and dividing by μ_1 we obtain

$$\frac{\mu_3}{\mu_1} \geq \frac{\mu_2^{3/2}}{\mu_1} = \mu_2 \cdot \frac{\sqrt{\mu_2}}{\mu_1}. \tag{2.25}$$

As $\sqrt{\mu_2}/\mu_1 \geq 1$, it is clear from equation 2.25 that $\mu_3/\mu_1 \geq \mu_2$. This suggests that

$V_{rms}(z)$, obtained by averaging in depth, in equation 2.23 will always exceed the standard rms velocity $V_{rms}(t)$, obtained by averaging in time, in equation 2.22. This observation is highlighted by the estimated values of $V_{k,rms}$ in Table 2.1. These 'over-estimated' rms velocities in depth are likely to result in a lower estimate of interval velocity as compared with the Dix inversion in time. However, the estimated interval velocities using equation 2.21 are displayed in Table 2.1 and offer good agreement with the true values.

2.3 A Comparison with Conventional Velocity Analysis

In the early stages of seismic processing, reflection data are typically rearranged into CMP gathers. Each trace within the CMP gather is assumed to have sampled the same subsurface point. This allows traces to be combined (or stacked) to enhance the arrivals of interest, in this case the primary reflections from the common midpoint. We exploit the fact that such arrivals have a normal moveout (NMO) defined as follows:

$$\Delta t_{NMO} = \sqrt{t_0^2 + \frac{x^2}{V_{rms}^2}} - t_0. \tag{2.26}$$

For the appropriate value of t_0 and V_{rms} in equation 2.26 each trace is shifted upward in time by Δt_{NMO}. Such a procedure removes the effect of offset x and results in the primary reflections being horizontally aligned in the CMP gather (called NMO correction). After this correction is performed the traces within each CMP gather are stacked. This results in a single trace recorded at zero-offset above the common midpoint. The aligned primary reflections sum constructively. Other wave types sum destructively and are thus suppressed. For comparison with interferometric velocity analysis, we perform an NMO correction on the CMP gathers of the multi-layered model (Figure 2.11).

Using the complete array of sources and receivers, we group the seismic data

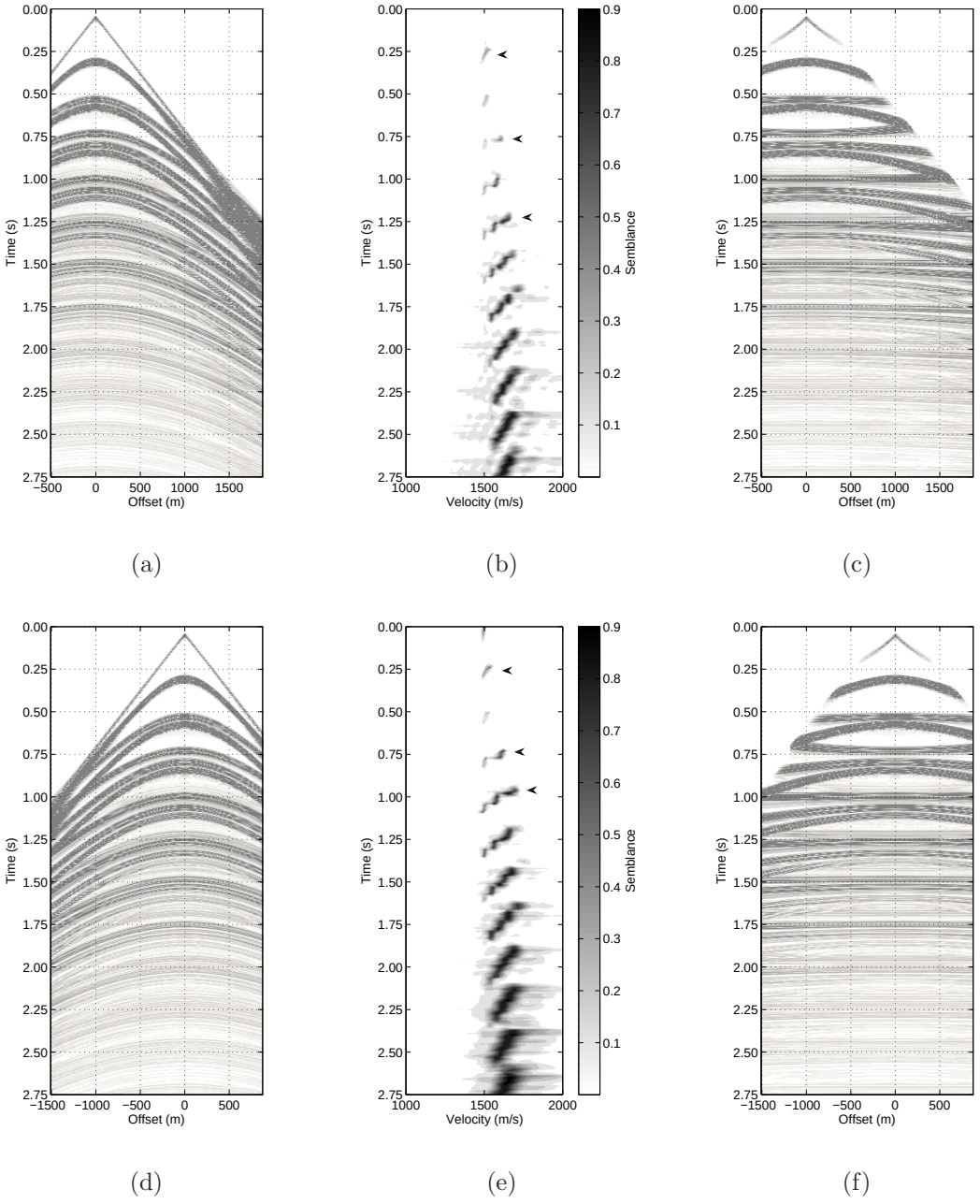

Figure 2.17: NMO correction performed on two CMP gathers from Figure 2.11. (a) CMP 1500. (b) Velocity spectrum for CMP 1500. (c) NMO-corrected CMP 1500. (d) CMP 2000. (e) Velocity spectrum for CMP 2000. (f) NMO-corrected CMP 2000. In (b) and (e), arrowheads show where time-velocity picks are made.

into their respective CMP gathers. Figure 2.17(a) and 2.17(d) display two CMP gathers (which are numbered CMP 1500 and CMP 2000, respectively). Here, we have applied a time-squared gain and have retained the full wavefield (including

multiples). Figure 2.17(b) and 2.17(e) shows the corresponding velocity spectra with time-velocity picks. It is not clear which arrivals are primaries and hence which should be picked for NMO correction. In this instance, the multiples are incorrectly handled by the semblance computation, as they are essentially treated as primary arrivals. The events picked allow for an adequate NMO correction in Figure 2.17(c) and 2.17(f). The majority of arrivals appear nicely flattened; however as is the objective in velocity analysis, we wish for multiple arrivals to stack out and not reinforce. In interferometric velocity analysis we obtain isolated peaks (in previous figures) because we treat multiples correctly.

2.4 Discussion

In the preceding sections, we have shown that interferometric velocity analysis can be used to constrain the interval velocity and layer thickness of a layered acoustic model. There are several advantages and disadvantages of such a method. We begin with the limitations.

First, as with any layer-stripping approach, any error that occurs near the beginning of the process will propagate throughout. We aim to reduce these errors by using multiples to constrain the rms velocity and thickness of each layer. However, there is a trade-off between considering a high number of multiple events and the amount of computation required to calculate traveltime curves. A similar effect occurs when the number of layers or sources are increased. When many more than four layers are considered, however, the method may become overly complex due to the number of orders of multiply reflected waves to be considered. Therefore, we remark that interferometric velocity analysis works well to characterize a small number of horizontal layers beneath a receiver array.

Another drawback is that we have to know what range of velocities and layer thicknesses to use in the semblance computation. However, this same drawback is

encountered during the generation of a standard velocity spectrum (Figure 2.17(b) and 2.17(d)) where a suitable range of velocities and vertical two-way traveltimes must be defined. We use realistic parameters of Z and V that span a broad range of values. However, some prior knowledge from well logs or from other means may prove beneficial. Prior knowledge would also help with the velocity interpretation, especially when we obtain peaks with different velocities as in Figure 2.16 and 2.17.

Similar to NMO analysis, here we assume a sequence of horizontal layers. In its current form, interferometric velocity analysis breaks down in the presence of dip. For an inclined interface, the traveltime of the primary arrival is dependent on the perpendicular depth from the source to reflector and on the dip angle of the interface. If the shot position is moved laterally, the depth point of the primary arrival shifts accordingly. Therefore, in a method such as ours that relies on the traveltime differences between numerous shots, to invert for a single depth point would be meaningless. Such a procedure, although feasible, becomes highly complicated when multiples are considered and a dip moveout (DMO) analysis would achieve the required objective.

Despite these disadvantages, interferometric velocity analysis has several benefits. In our interferometric examples, we correctly use multiple energy to constrain the velocity and layer-thickness estimate. As demonstrated in the previous section, this contrasts with conventional velocity analysis, where multiple arrivals are usually ignored and only primary arrivals are picked. Moreover in some cases, like the NMO-corrected gathers in Figure 2.17(c) and 2.17(f), conventional velocity analysis treats multiples as primaries causing the multiple arrivals to align. On the other hand, interferometric velocity analysis treats multiples differently from primaries – all are considered with their correct ray geometries. Although in the multi-layered case we remove the direct arrival from each common shot gather, the fact that we consider multiply reflected wavefields

means that interferometric velocity analysis is closer to a full wavefield-based technique.

Interferometric velocity analysis is applicable to only a single receiver pair at a time. This has two advantages. First, in seismic surveys in which a large number of receivers are deployed, the technique allows for velocity and layer-thickness estimation between fixed receiver pairs. This allows for a high spatial frequency of velocity and layer-thickness estimates to be computed because there are usually a higher density of receivers than sources. Second, and perhaps more important, in areas where sparse source and receiver coverage exists (for example in areas of complex terrain or where ocean-bottom receivers are deployed), CMP methods may not be applicable. In these settings, interferometric velocity analysis provides a direct alternative to conventional velocity estimation. In fact, as we have shown, we achieve high-coherence estimates when only 80 sources are considered. However, we should bear in mind that these values may not be the most accurate (using all sources appears better in Figure 2.15); a degree of interpretation is therefore required. However, the method is ideally suited to applications where source coverage is limited. Furthermore, because these sources may be positioned far from the receiver pair, the method is compatible with long-offset seismic reflection data. By source-receiver reciprocity, all of the above remains true if sources and receivers are interchanged.

So far we have discussed interferometric velocity analysis with respect to cross-correlation- and deconvolution-type interferometry because the required source-receiver geometries can be approximated using conventional marine data acquisition. However, interferometry can be performed by cross-convolution using an equation not dissimilar to equation 2.1,

$$G(\mathbf{x}_B, \mathbf{x}_A) \approx \oint_S \frac{2}{\rho c} G(\mathbf{x}_B, \mathbf{x}) G(\mathbf{x}_A, \mathbf{x}) d^2\mathbf{x}. \tag{2.27}$$

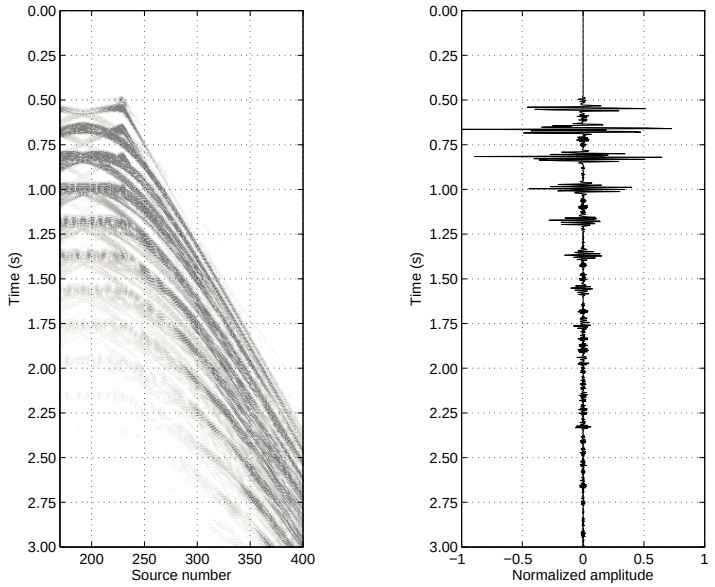

(a) (b)

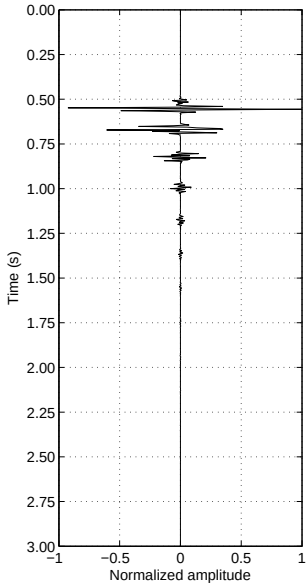

(c)

Figure 2.18: Interferometric Green's function estimates and true Green's function for the single layer over half-space model in Figure 2.1. (a) Convolution gather for receivers 1 and 151 showing arrivals between 0 s and 3 s. (b) Green's function estimate after summation over source position in (a). True Green's function.

A third interferometric gather, the convolution gather, can therefore be defined similarly to the other gathers described. In cross-convolutional interferometry

we require a slight modification to the usual geometry of sources and receivers in Figure 1.1 (Chapter 1): it is necessary that one of the pair of receivers be positioned outside of the source boundary. For example, in the single layer over a half-space model as shown in Figure 2.1, we can fulfil this requirement by considering receivers 1 and 151 and only the portion of the source boundary between 170–400. In that case, we can imagine that if this portion had been complemented with sources in two vertical lines below sources 170 and 400, plus along a horizontal section at depth, receiver 1 would be outside this boundary. Figure 2.18(a) shows the corresponding convolution gather using only the surface sources. Figure 2.18(b) displays the Green's function estimate and Figure 2.18(c) shows the true Green's function. In Figure 2.18(a) the physical energy (i.e., the stationary-phase region) is located between source numbers 170–240. Outside this region the remaining energy can be considered largely non-physical. In contrast to cross-correlation interferometry, now any significant energy occurs at the traveltime summations

$$\sigma\mathbf{t} = \frac{\sqrt{x_{r_j}^2 + (2br_jZ_1 \pm z_s \pm z_{r_j})^2}}{V_1} + \frac{\sqrt{x_{r_i}^2 + (2br_iZ_1 \pm z_s \pm z_{r_i})^2}}{V_1} \qquad (2.28)$$

between waves recorded at both receivers rather than the traveltime difference. We perform interferometric velocity analysis as before where semblance is defined by equations 2.9– 2.11, but now we use the traveltime summation equation 2.28. Figure 2.19(a) shows the semblance computed using energy up to the sixth-order multiples ($b_{r_i} = b_{r_j} = 7$) using sources 170–240, located in the stationary phase region of the convolution gather. We obtain a velocity and layer-thickness pair that lies close to the true values of 1500 m/s and 150 m. Figure 2.19(b) shows the semblance computed using energy up to the sixth-order multiples using sources 240–400, located in the non-stationary region of the convolution gather. Although our estimate of velocity remains good, the layer-thickness estimate is smeared

along the vertical axis. As we now deal with the traveltime summations in equation 2.28, the convolutions between reflected wavefields (excited far from the receiver pair) appear very close together (e.g., see the non-stationary region between sources 240–400 in Figure 2.18(a)). This contrasts with the correlation gather, where the cross-correlation of reflected wavefields appears farther apart than the respective wavefields at the stationary-phase point (e.g., see the non-stationary region in Figure 2.4(d)). The smearing in Figure 2.19(b) may be a direct consequence of the converging wavefield in Figure 2.18(a). We suggest that if sources are predominantly located in the stationary-phase position, convolution interferometric velocity analysis may work sufficiently well. On the other hand, if sources are positioned in the non-stationary regions, as is the usual case in long-offset seismic surveys, we suggest that correlation interferometric velocity analysis may provide the better option.

Finally, a significant theoretical contribution of this chapter is to show that a great deal of information lies within – and hence, can in principal be extracted from – the non-physical energy contributions to interferometric wavefields. This corroborates the results of previous studies which have used non-physical wavefields to derive refraction velocities (Mikesell et al., 2009) and new optical theorems (Halliday and Curtis, 2009b) and shows that rms velocities are also recoverable from this energy.

2.5 Conclusions

In seismic interferometry, the correlation gather is typically summed over the source position to produce the inter-receiver Green's function. The resulting summation removes a significant amount of non-stationary energy (termed non-physical energy in seismic interferometry) through destructive interference. However, this non-physical energy provides valuable information about the physical

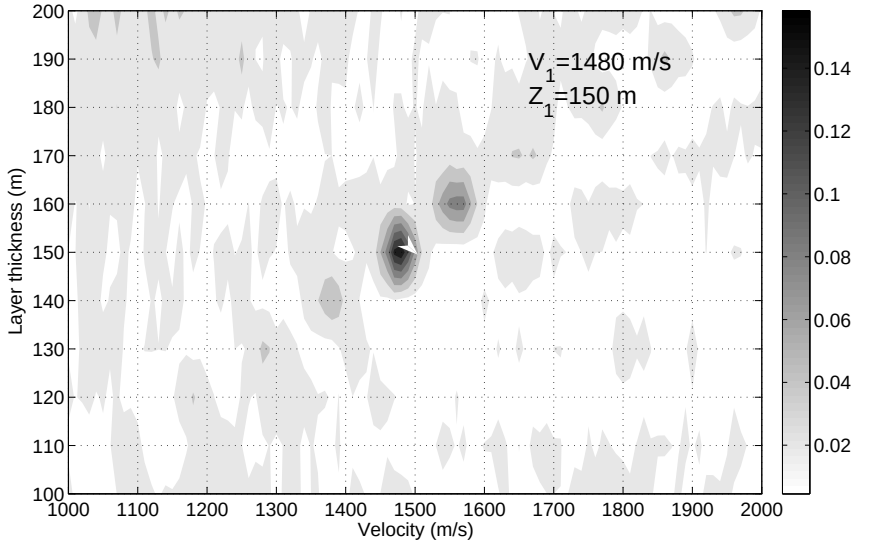

(a)

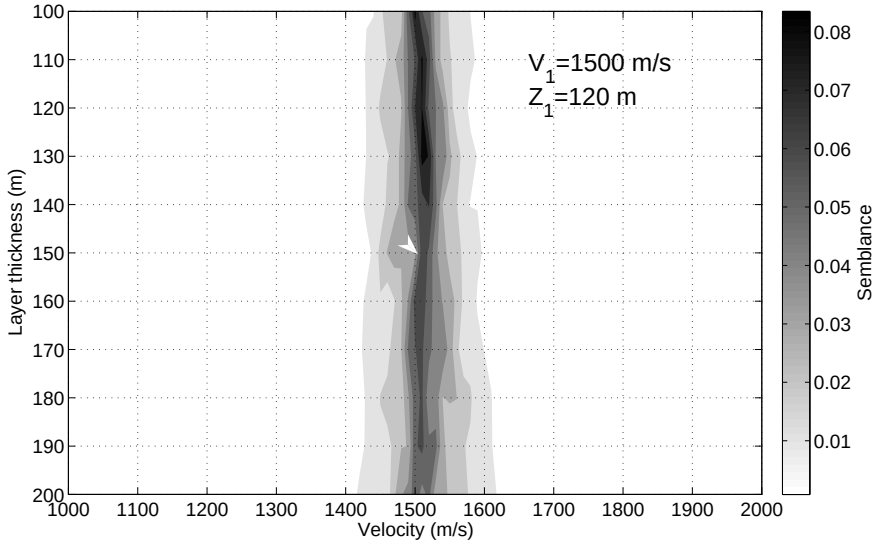

(b)

Figure 2.19: (a) Spectrum showing V_1 against Z_1 calculated using source numbers 170–240 in the stationary-phase region. The velocity V_1 spans from 1000 to 2000 m/s and increments every 10 m/s. The layer thickness Z_1 spans from 100 to 200 m and increments every 10 m. We use a time window of 10 m/s. (b) As for (a) but computed for source numbers 240–400, located in the non-stationary region.

rock properties of the subsurface. We describe a method that uses both the physical and non-physical energy to obtain this information from the correlation gathers, called interferometric velocity analysis. The method constrains the root-

mean-square (rms) velocity and layer thickness of a horizontally layered synthetic acoustic model, which allows us to estimate interval velocity.

We use the multiply reflected wavefield (both free-surface multiples and interbed multiples) to further constrain rms velocity and layer-thickness estimates. Traditionally, these arrivals are handled incorrectly in, or even suppressed prior to the onset of, velocity analysis. We find that by including the multiply reflected wavefield we achieve better constrained rms velocity and layer-thickness estimates. We show that by using sources positioned near the endpoints of the source boundary which contribute mainly to non-physical energy, we achieve a better-defined estimate of rms velocity and layer thickness. The method may be ideally suited to both short and long-offset reflection data.

Unlike conventional common midpoint (CMP) techniques which require a large array of both sources and receivers, we require only two receivers and a small array of sources (or, by reciprocity, two sources and an array of receivers). This has implications in exploration seismology, for example in land data or ocean-bottom seismics, where sparse source and receiver coverage may limit the application of CMP analysis. In these situations, our method may provide a direct alternative to conventional methods of velocity estimation. We do not expect our method to replace conventional CMP analysis; however, it may be used in conjunction with it as an additional processing tool.

Chapter 3

Velocity analysis using both reflections and refractions in seismic interferometry

The Green's function between two receiver locations can be estimated by cross-correlating and summing the recorded Green's functions from sources on a boundary that surrounds the receiver pair. We show that when two receivers are positioned far from the source boundary in a marine-type acquisition geometry, the cross-correlations (the Green's functions before summation over the source boundary) are dominated by reflected energy which can be used in a semblance analysis to determine the seismic velocity and thickness of the first layer. When these cross-correlations are summed over the boundary of sources, the resulting Green's function estimates along a receiver array contain non-physical or spurious refracted energy. We show using a further semblance analysis that the most prominent non-physical refracted energy occurs prior to the direct arrival and determines the remaining refraction velocities of deeper layers (or interval velocities in the case of a subsurface with homogeneous layers). We demonstrate the velocity analysis procedure on a single layer over half-space model, a three

layer over half-space model, and a more realistic model based on a North Sea oilfield.

3.1 Introduction

A seismic image represents subsurface interfaces or points at which the (an)elastic properties of the Earth vary significantly in magnitude over a spatial length scale that is short relative to the wavelength of seismic waves. Before an image can be computed, we require an accurate estimation of the elastic property variations over length scales of a wavelength or longer, often referred to as a seismic velocity model. Usually geophysicists estimate the subsurface seismic velocities by analysing the kinematic properties of recorded traveltimes as a function of the source-receiver offset.

In this Chapter, we study the moveout properties of reflected and refracted Green's function estimates that have been redatumed to a receiver array located beneath the free surface using seismic interferometry. We aim to estimate the seismic velocity using these moveout properties.

To estimate the Green's function with the correct kinematic and amplitude properties, theory dictates that the source boundary must enclose the receiver pair (indicated by the closed integral in equation 2.1 in Chapter 2). In exploration seismology it is usual for the source boundary to be partially complete resulting in an erroneous Green's function contaminated with artifacts known as non-physical arrivals (Snieder et al., 2006b). Here, we use the moveout of such artifacts to obtain model subsurface information.

The retrieval of reflections and refractions in seismic interferometry has received both theoretical and applied attention. Bakulin and Calvert (2006) and Mehta et al. (2007) showed that by cross-correlating recordings in a horizontal well at depth, reflections that are relatively free from the distortive effects of a complex

overburden can be synthesized. Theoretically, Snieder et al. (2006b) extract the primary reflection by cross-correlating the direct arrival with the primary reflection. Tatanova et al. (2008) present a similar derivation but focus on the contributions obtained when cross-correlating refracted energy.

Little attention has been focused on the possibilities of using seismic interferometry to recover information about the long-wavelength seismic velocity model in exploration seismology. Examples that do exist estimate the seismic velocity using interferometric refractions (Mikesell et al., 2009) and reflections (Chapter 2), respectively. The former authors show that the cross-correlation of refracted energy leads to a spurious linear refraction that passes through the origin and whose gradient is equal to the slowness of the refracting layer. In Chapter 2 we demonstrate that interfering primary and multiple energy in the so-called correlation gather can be used to find the root-mean-square (rms) and interval velocities of a multi-layered model.

We study the retrieval of reflected and refracted Green's functions in a marine seismic setting. We combine the approach outlined in Chapter 2 with that of Mikesell et al. (2009) (see Chapter 1) to investigate the seismic velocity of subsurface strata. We perform a semblance analysis on the cross-correlated wavefield between two receivers to estimate the velocity and thickness of the first layer. We then show that when the receiver array is positioned at far offset from the illuminating source array, the estimated Green's functions are dominated by non-physical refracted energy prior to the direct arrival, similar to that identified by Mikesell et al. (2009), that can be used to characterize the seismic velocity of deeper layers using a semblance analysis. We demonstrate our velocity analysis procedure on a single layer over half-space, and a three layer over half-space acoustic models. Finally, we demonstrate this procedure on a more realistic 2.5D model based on a North Sea oilfield.

3.2 Seismic interferometry in exploration seismology

3.2.1 Single layer over a half-space model

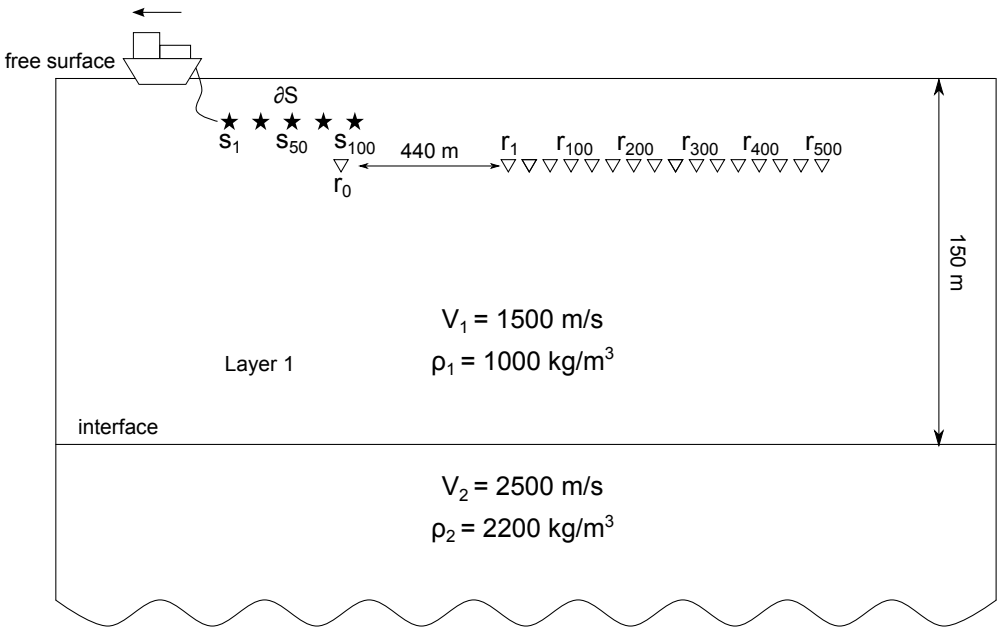

Figure 3.1: Single layer over half-space model showing acquisition geometry. Velocities (V_1 and V_2) and densities (ρ_1 and ρ_2) are shown. Sources and receivers are denoted by stars and triangles, respectively. The source boundary ∂S, containing 100 sources at 5 m depth, illuminates 501 receivers at 15 m depth. Sources are spaced every 8 m. An isolated receiver r_0 is positioned directly beneath source 85. The remaining 500 receivers form an array, 440 m from source 100, and are separated at 4 m intervals.

Figure 3.1 shows a single layer over half-space homogeneous model and acquisition geometry. The model comprises an upper layer with a velocity of 1500 m/s separated from a half-space with velocity of 2500 m/s by a planar interface at 150 m depth. A boundary of 100 sources, at 5 m depth, illuminates 501 receivers, at 15 m depth. Receiver r_0 is positioned directly beneath source 85. The remaining 500 receivers form an array. In this example, we produce synthetic data by firing each source on the boundary ∂S in turn and modelling the full wavefield Green's functions to all receivers using a 2D acoustic finite-difference scheme (Robertsson et al., 1994). Figure 3.2 shows the shot gather

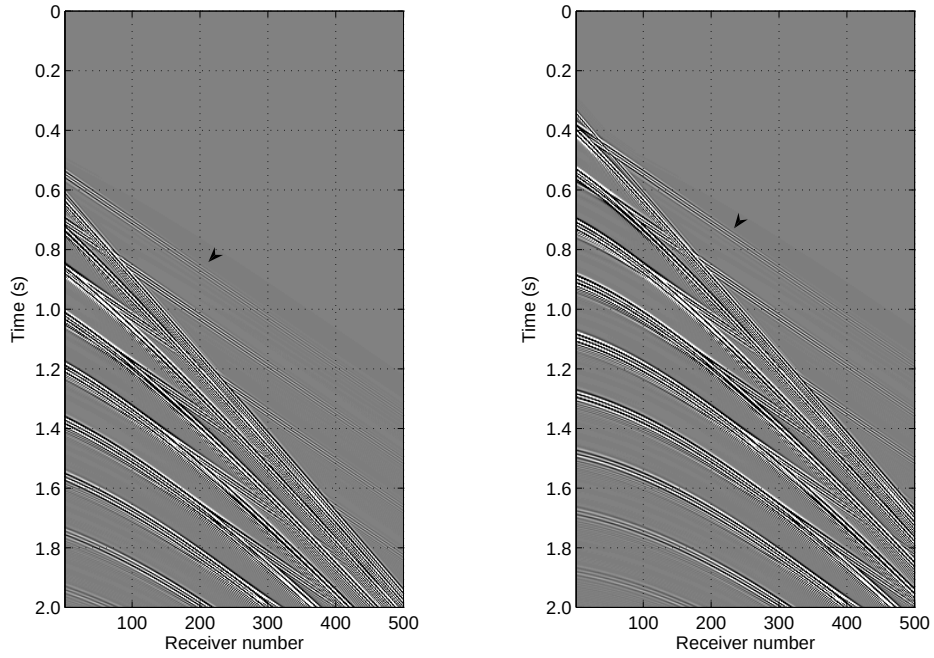

Figure 3.2: Shot gathers from source 50 (a) and 100 (b) in Figure 3.1.

from source 50 and source 100, respectively. The arrowhead denotes the singly-refracted arrival.

Figure 3.3(a) shows the correlation gather for receivers r_0 and r_1 obtained using equation 2.1. The distance between r_0 and r_1 is 560 m. The cross-correlation operation subtracts the phase of the wavefield recorded at r_0 from the phase of the wavefield recorded at r_1. Hence, wavefields in the correlation gather occur at the traveltime differences between waves recorded at the two receivers. Reflected wave energy in the correlation gather arrive at traveltimes $\delta\mathbf{t}$ according to equation 2.4.

In the following traveltime interpretation we assume that V_1 and Z_1 are known and that waves are downgoing at the source and upgoing at the receiver. Figure 3.3(b) displays a reflective traveltime interpretation of the correlation gather using equation 2.4. For clarity, we do not interpret every arrival, but a significant number to provide the reader with a good impression of the correlation gather properties. The V-shaped traveltime curves represent the cross-correlation

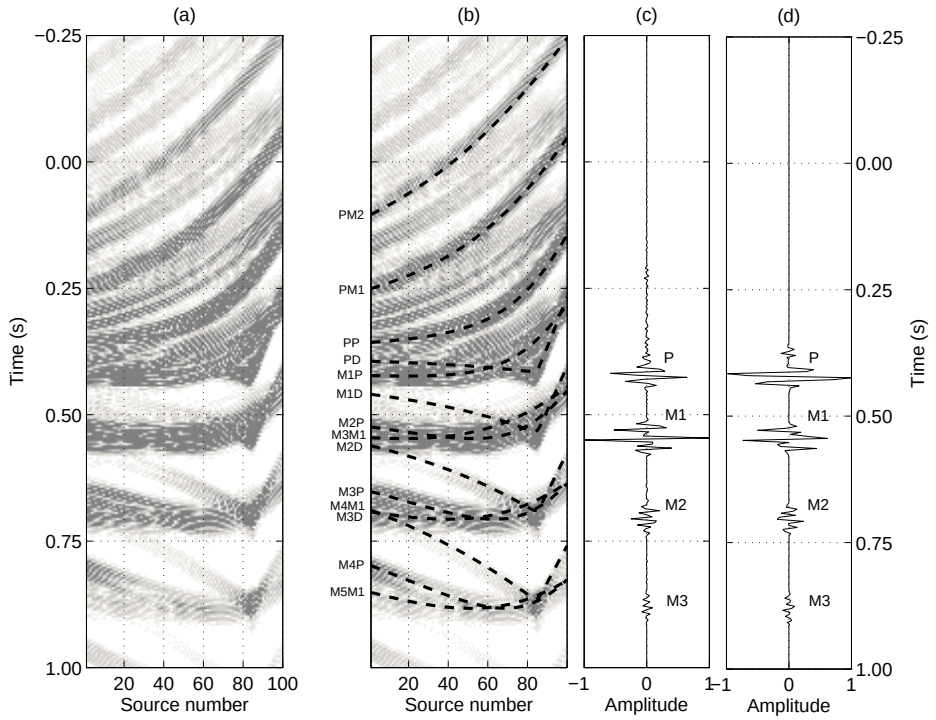

Figure 3.3: (a) Correlation gather for r_0 and r_1, with (b) reflective traveltime interpretation for single layer over half-space model. (c) Normalized Green's function after summation over source number in (a). (d) Normalized true Green's function. In (b), we annotate reflected cross-correlational energy (dashed black curves) and assume the convention 'M1P' for example, which refers to the cross-correlation of the first-order multiple (M1) at r_1 with the primary reflection (P) at r_0. Abbreviations are D – direct arrival, P – primary reflection, M1 – first-order multiple, M2 – second-order multiple, and so on. In (c) and (d), we include an interpretation of arrivals.

of increasing orders of reflections, primary (P) or multiple (MN) at r_1, where N is the multiple order (e.g., $b_{r_j} > 0$ in equation 2.4), with the direct arrival D ($b_{r_i} = 0$) at r_0. The smooth traveltime curves represent the cross-correlations between reflections at both receivers (see the left-hand side of Figure 3.3(b) and caption for further definitions). Figure 3.3(c) shows the Green's function estimate after summing the correlation gather over all source numbers. Stationary energy in the correlation gather (i.e., extrema in Figures 3.3(a) and 3.3(b) – energy that varies slowly with respect to the boundary source location) will add constructively and provides the dominant contribution to the Green's function

estimate in Figure 3.3(c) (Snieder, 2004; van Manen et al., 2005, 2006). Active sources that produce stationary energy are called stationary-phase sources. Apart from the incoherent noise obtained prior to the primary reflection P, the Green's function estimate shows reasonable agreement with the true Green's function in Figure 3.3(d).

In exploration seismology, most receivers are positioned at far offset from the available sources. Hence, consideration of the equivalent panels for example receivers r_{200} and r_{400} would provides a more likely or practical scenario than having a receiver at r_0 as above. Figure 3.4(a) shows the correlation gather for receivers r_{200} and r_{400} with traveltime interpretation (using equation 2.4). The distance between r_{200} and r_{400} is 800 m. Instead of distinct extrema as displayed in Figure 3.4(a), near-horizontal arrivals which represent the cross-correlation between reflections provide the stationary energy to the Green's function estimate (Figure 3.4(b)). These linear arrivals should not be confused with those generated by the cross-correlation of refractions, for example the 'virtual refraction', as observed in Mikesell et al. (2009). In fact, although both receivers are positioned past the critical offset (= 210 m) for all 100 sources, refractions are not observable in the correlation gather because their amplitudes are masked by those of reflections. Refraction amplitudes decrease rapidly with increasing range as $1/(L^{3/2}x_{r_{i,j}}^{1/2})$, where $L = x_{r_{i,j}} - x_c$, $x_{r_{i,j}}$ is the offset between source and receiver, and x_c is the critical offset (Kennett, 1977). Reflections dominate the correlation gather because their amplitudes decrease only as $1/x_{r_{i,j}}$.

Positive arrival times in the estimated Green's function in Figure 3.4(b) show reasonable agreement to those in the positive-time true Green's function in Figure 3.4(c). The reflected energy before 0.5 s in the correlation gather interferes destructively resulting in an estimated Green's function at negative times which shows little agreement to the true homogeneous Green's function. Despite this, it is clear from Figure 3.4(d), which shows an enlarged portion of the Green's

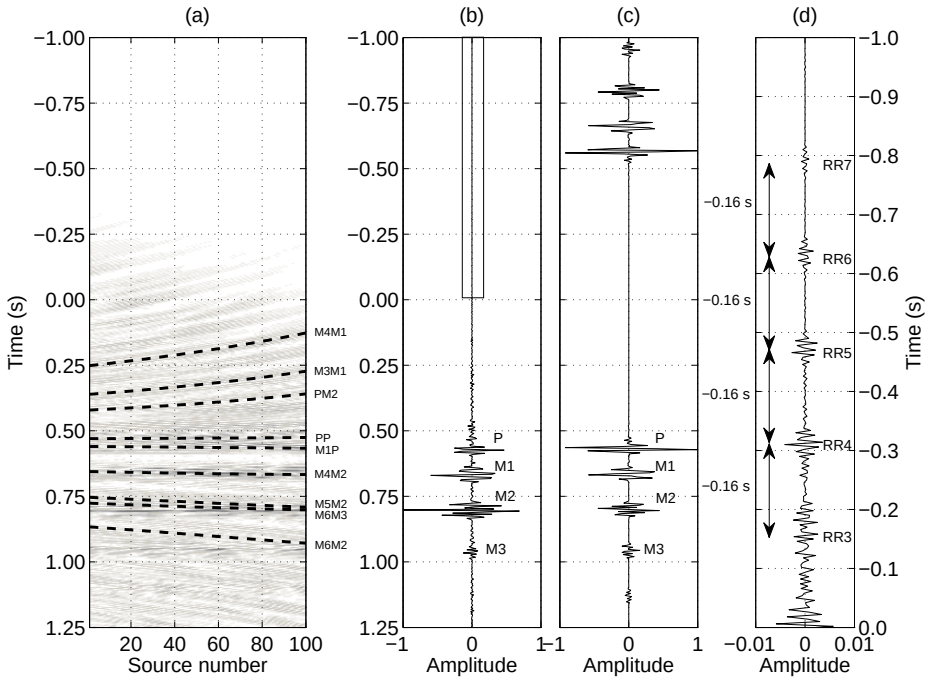

Figure 3.4: (a) Correlation gather for r_{200} and r_{400} with reflective traveltime interpretation for single layer over half-space model. (b) Normalized Green's function after summation over source number in (a). (c) Normalized true Green's function. (d) Enlargement showing the Green's function in the box in (b). In (a), the annotation convention follows that of Figure 3.3.

function within the box in Figure 3.4(b), that we obtain coherent arrivals of cross-correlated energy separated at constant -0.16 s intervals. These arrivals result from the summation of the cross-correlational energy between pairs of refracted waves according to the following traveltime equation:

$$\delta \mathbf{t} = \Big(\frac{x_{r_j}}{V_2} + \frac{(2b_{r_j} Z_1 \pm z_s \pm z_{r_j}) \cos\theta_c}{V_1} \Big) - \Big(\frac{x_{r_i}}{V_2} + \frac{(2b_{r_i} Z_1 \pm z_s \pm z_{r_i}) \cos\theta_c}{V_1} \Big) \quad (3.1)$$

where θ_c is the critical angle at the interface as determined by Snell's law. When $b_{r_j}(b_{r_i}) \geq 2$ the wavefield represents a surface-related refraction multiple (Meissner, 1965). For example, Figure 3.5 shows a sketch of a second-order free-surface multiple. In Figure 3.4(d), the energy at -0.16 s represents the third-order refraction multiple, R3, ($b_{r_i} = 4$) at r_{200} cross-correlated with the singly-refracted

arrival, R, ($b_{r_j} = 1$) at r_{400}. Similarly, the energy at approximately -0.32 s, -0.48 s, -0.64 s and -0.80 s represent increasing orders of refraction multiples, RN, where $N \geq 4$ at r_{200} cross-correlated with the singly-refracted arrival, R, at r_{400}. Tatanova et al. (2008) term the cross-correlation of refracted energy that appears prior to the actual refracted arrival as satellite waves. This refracted energy is not observable in the raw correlation gather but is clearly visible in the Green's function estimate after the reflected energy at negative times has cancelled through destructive interference.

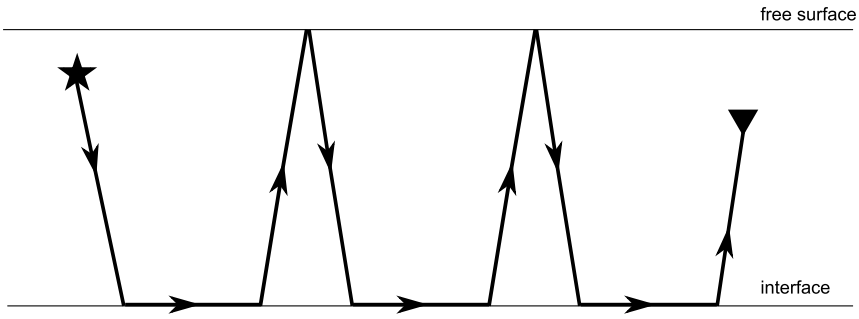

Figure 3.5: Sketch showing a second-order refraction multiple.

These non-physical refractions are more obvious when we produce the estimated Green's function along the receiver array. Figure 3.6 shows the virtual source gather obtained by cross-correlating the records at r_{200} with receivers r_1–r_{500} using equation 2.1. The estimated Green's functions for r_1–r_{199} have been time-reversed so that the moveout properties resemble those of a usual source gather. We apply this operation to traces left of the virtual source in all virtual source gathers that follow. The Green's function estimates are dominated by linear and largely non-physical refracted arrivals (see dashed lines in Figure 3.6 for their traveltime interpretation). The arrival marked RR is the 'virtual refraction' as described by Mikesell et al. (2009). The circles mark the coherent arrivals displayed in Figure 3.4(d). We observe high-amplitude reflection events that asymptote to the non-physical refractions R2R, R3R, R4R and R5R, respectively.

For example, the second-order free-surface multiple is an asymptote to R3R. However, we do not observe the characteristic reflection hyperbola for two reasons. First, we require sources positioned at distinct reflected wave stationary-phase locations and in their associated Fresnel zones. Several stationary-phase sources (particularly those that lie close to and above the virtual source receiver as in Figure 3.3(a) for example) are not available in typical marine seismic surveys like this one. Second, the cross-correlation of reflected waves excited by sources near the surface produce a reflected Green's function whose amplitude is smaller than that of the true reflected wave since obtaining the true amplitude requires sources at depth (Forghani and Snieder, 2010). On the other hand, refracted energy from sources that are past the critical offset (= 210 m) at the virtual source receiver, will add constructively in the estimated Green's function. Therefore, the stationary-phase requirement for non-physical refracted waves is less restrictive than for reflected waves, and hence for the model shown here the cross-correlation of r_{200} with r_1–r_{500} will produce a Green's function dominated by refraction-associated events.

3.3 Velocity determination using reflections and non-physical refractions

Although we do not observe reflection hyperbola in Figure 3.6, the reflected energy in the correlation gather (Figure 3.4(a)) is still useful for determining the unknown velocity V_1 and layer thickness Z_1 of the first layer. By choosing different estimates of V_1 and Z_1 and different values of $b_{r_j}(b_{r_i})$ in equation 2.4 we compute the traveltime difference moveout curves and measure the associated signal coherency in the correlation gather. Here, we use semblance as the coherence measure which

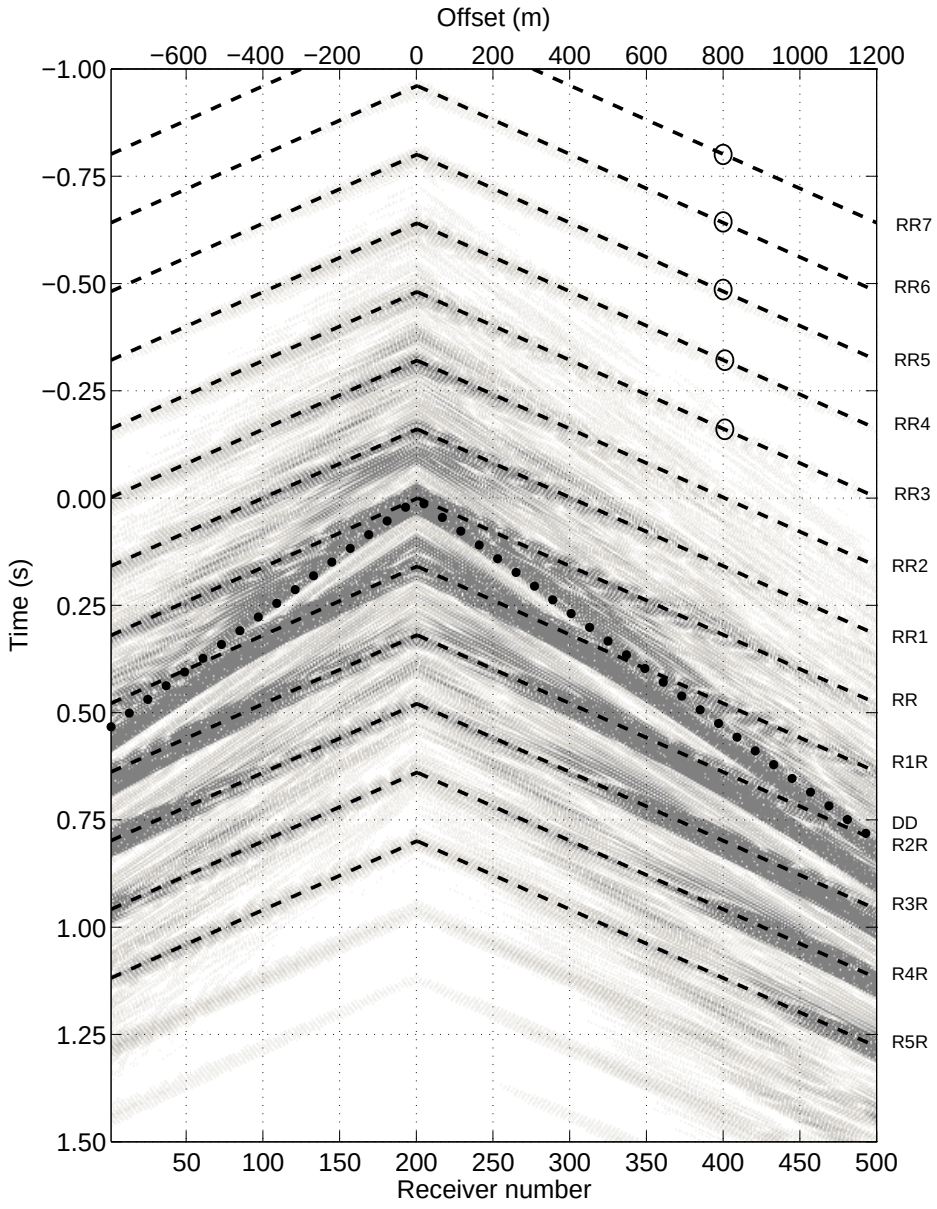

Figure 3.6: Virtual source gather for single layer over half-space model. The virtual source is positioned at r_{200}. On the right-hand side, the direct and non-physical refracted Green's functions are annotated using the convention outlined in the caption to Figure 3.3. Abbreviations are D – direct arrival, R – singly-refracted arrival, R1 – first-order refraction multiple, R2 – second-order refraction multiple and so on. Circles represent the traveltime of the coherent arrivals in Figure 3.4(d). Traces at negative offsets have been reversed in time to emulate a more familiar form of the (virtual) source gather.

is defined as,

$$S_c = \frac{1}{(b_{r_i} \cdot b_{r_j})} \sum_{i=1}^{b_{r_i}} \sum_{j=1}^{b_{r_j}} \frac{E_{i,j}^{out}}{N \cdot E_{i,j}^{in}} \qquad 0 \leq S_c \leq 1, \tag{3.2}$$

where N is the number of sources or 'traces' in the correlation gather and the output energy E_{out} and input energy E_{in} are defined as,

$$E_{i,j}^{out} = \sum_{t(k)=\delta t - t/2}^{\delta t + t/2} \left\{ \sum_{l=1}^{N} f_{i,j,l,t(k)} \right\}^2 \tag{3.3}$$

and

$$E_{i,j}^{in} = \sum_{t(k)=\delta t - t/2}^{\delta t + t/2} \sum_{l=1}^{N} f_{i,j,l,t(k)}^2. \tag{3.4}$$

where f is a function of V_1, Z_1, b_{r_i}, b_{r_j} and is the amplitude value at the lth source at time δt within a time window $[-t/2\ t/2]$. After summing over b_{r_i} and b_{r_j} in equation 3.2, we create a velocity–layer-thickness spectrum. In all examples, we use a time-window length equal to 20 ms. Figure 3.7(a) shows the velocity-layer thickness spectrum computed using all 100 sources and energy up to the third-order multiples ($b_{r_{i,j}} = 4$) from the correlation gather in Figure 3.4(a). We see a peak centered at $V_1 = 1480$ m/s and $Z_1 = 160$ m, close to the correct parameters of velocity and layer thickness however, the estimate is smeared towards higher and lower thicknesses. Figure 3.7(b) shows the corresponding velocity–layer-thickness spectrum from the correlation gather in Figure 3.3(a). In comparison, we achieve a better-constrained peak. The reason for this difference can be explained by observing the two respective correlation gathers. The correlation gather in Figure 3.3(a) shows reflected energy which is well-defined in space and time. This leads to a good estimate of V_1 and Z_1 in Figure 3.7(b). The separation of reflected energy is less clear in the correlation gather of Figure 3.4(a) and the estimate of V_1 and Z_1 in Figure 3.7(a) is more smeared as a result. Nevertheless, we demonstrate that the reflected energy in the correlation gathers contains useful

model information.

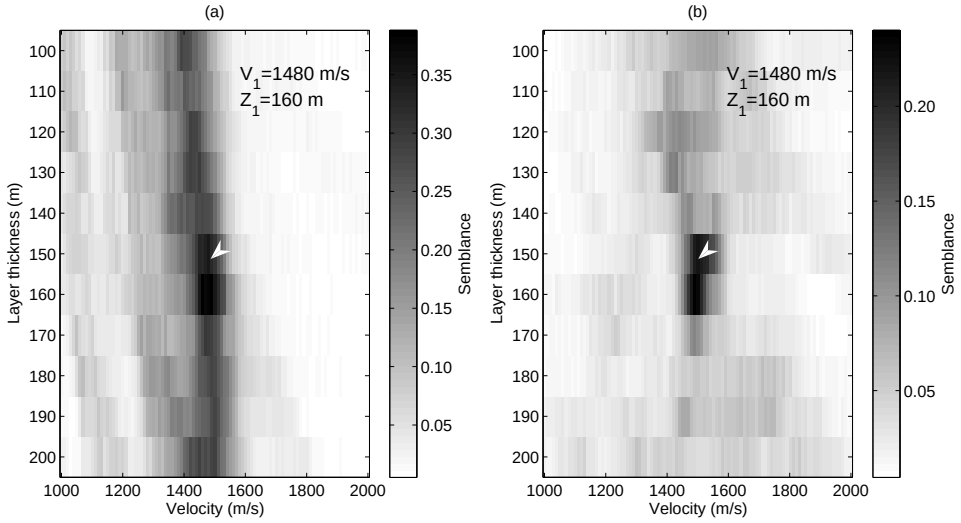

Figure 3.7: (a) Velocity (V_1) – layer thickness (Z_1) spectrum computed from the correlation gather in Figure 3.4(a) using energy up to the third-order multiples. (b) As for (a) but for the correlation gather in Figure 3.3(a). The V_1 and Z_1 values noted in the top right-hand corners correspond to the peak of maximum semblance. The arrowheads denote the actual parameters of velocity and layer thickness.

In addition, the linear non-physical refracted energy in the virtual source gather (Figure 3.6) contains information about the velocity of the half space. We create a second velocity spectrum by stacking energy with the linear traveltime equation

$$t = \tau + \frac{x}{V} \tag{3.5}$$

where τ is the traveltime at the virtual source position and x is the offset from the virtual source to a receiver. Equation 3.5 is equivalent to the slant-stack equation $t = \tau + px$, where p is the ray parameter (Yilmaz, 2001). Hence, the resultant velocity spectrum is a 'pseudo' slant-stack gather. In the slant-stack domain, we would expect reflections to map as ellipses and refractions to map as isolated points of energy (Diebold and Stoffa, 1981). However, as we do not observe reflection hyperbola in Figure 3.6, we expect to see isolated peaks that

correspond to the correct velocity V_2.

We now adopt the more usual form of semblance (i.e., the fraction and summations involving b_{r_i} and b_{r_j} are removed in equation 3.2 and N becomes the number of traces in the virtual source gather). Figure 3.8(a) shows the τ–V_2 spectrum obtained using equation 3.5 for receivers r_1–r_{200}. Note that this spectrum which uses traces to the left of the virtual source position, and all others that follow, was created using the traces in the virtual source gather (i.e., after the traces were reversed in time). Figure 3.8(b) shows the corresponding τ–V_2 spectrum for receivers r_{200}–r_{500}. In both spectra we observe a set of strong peaks at positive times at the correct velocity of 2500 m/s. Between 0 s and 0.5 s, we observe elliptical energy corresponding to the reflections. Peaks corresponding to refracted energy between 0 s and 0.5 s, and specifically the peak corresponding to the virtual refraction RR (Mikesell et al., 2009) at $\tau = 0$ s, are smeared because of the interference of reflected energy in the virtual source gather. At negative times we observe little reflected energy in either spectra but again see a further set of distinct peaks that have the correct velocity of 2500 m/s. Note, although the peaks at negative times have the same traveltime as the arrivals in Figure 3.4(d), the traveltime τ here is the traveltime at the virtual source position and not at the receiver. We obtain sharper peaks in Figure 3.8(b) because we use 100 more receivers in equation 3.5 than in Figure 3.8(a).

We can also use the traveltime difference between peaks $\Delta\tau$ to compute the thickness Z_1 of the refracting layer using the equation

$$Z_1 = \frac{\Delta\tau V_1 V_2}{2\sqrt{V_2^2 - V_1^2}}. \tag{3.6}$$

Assuming we know $V_1 = 1480$ m/s from Figure 3.7, and taking $V_2 = 2500$ m/s and $\Delta\tau = 0.16$ s as the time between peaks in Figure 3.8, the layer thickness using equation 3.6 is equal to 147 m. This agrees well with the alternative estimate

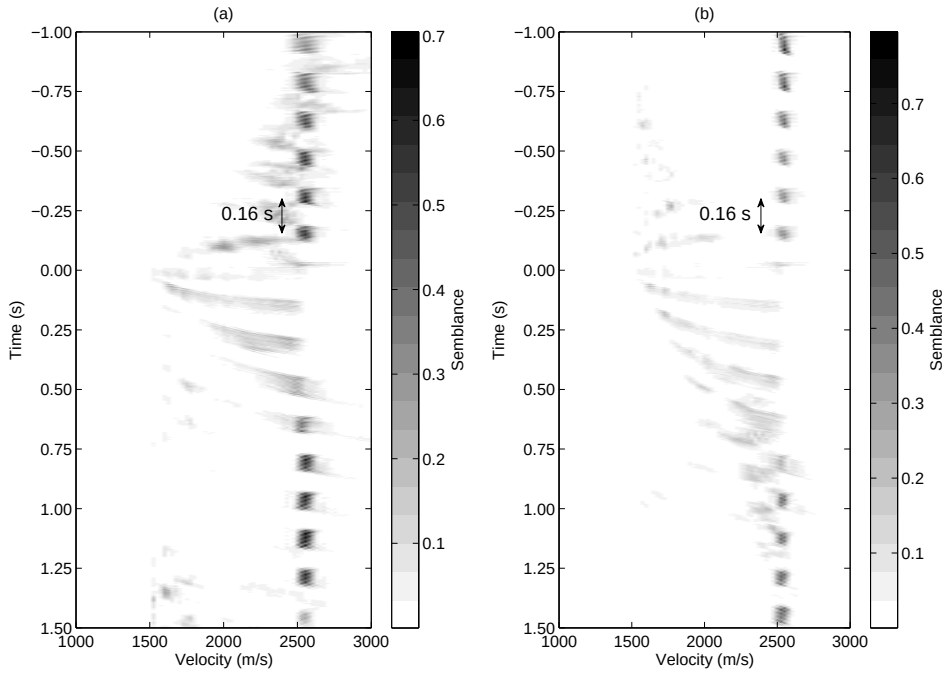

Figure 3.8: Velocity (V_2) – time (τ) spectrum computed using (a) receivers r_1–r_{200} and (b) receivers r_{200}–r_{500} from the virtual source gather in Figure 3.6.

made using the correlation gather (Figure 3.7).

3.3.1 Three layer over a half-space model

We adopt the same approach as above to determine the interval velocities for a three layer over a half-space acoustic model (Figure 3.9). Figure 3.10(a) and Figure 3.10(b) shows the shot gathers from source 50 and source 100, respectively.

Figure 3.11(a) shows the correlation gather for receivers r_{200} and r_{400}, respectively. An interpretation of arrivals, such as that displayed in Figures 3.3(b) and 3.4(a), is more difficult due to the overlapping wavefields created by the addition of two extra interfaces. Figure 3.11(b) displays the interferometric Green's function estimate; note the predominant reflected and refracted energy arrives at positive times. Figure 3.11(c) shows the true Green's function for comparison. Figure 3.12 displays virtual source gathers with the virtual source

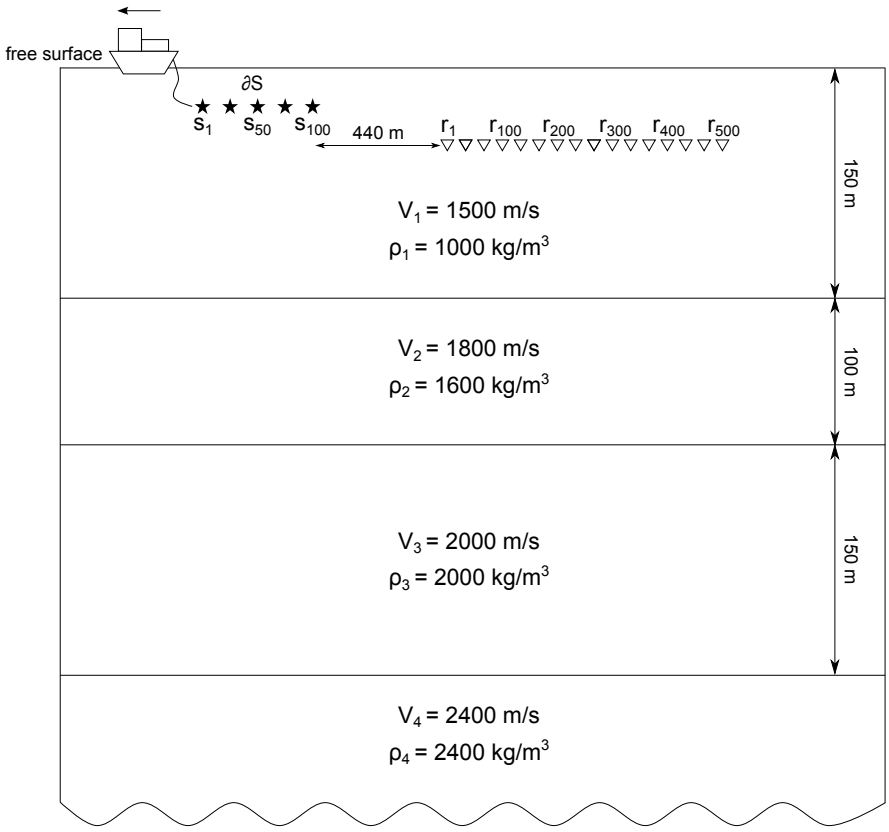

Figure 3.9: Three layer over a half-space model showing interval velocities (V_1, V_2, V_3 and V_4) and densities (ρ_1, ρ_2, ρ_3 and ρ_4). Acquisition geometry same as in Figure 3.3 but without receiver r_0.

positioned at r_{200} and r_{250}, respectively.

The correlation gather is dominated by reflected energy while the virtual source gather also includes non-physical refracted energy. As above, we exploit these differences to produce an estimate of the seismic velocity. Figure 3.13 displays the velocity–layer-thickness spectrum computed using all 100 sources and energy up to the third-order multiples (equation 2.4) from the correlation gather in Figure 3.11(a). We obtain a well-constrained peak close to the correct first-layer velocity and layer-thickness parameters, but also observe a more prominent 'ridge' towards higher and lower thicknesses for the reasons described earlier.

Figure 3.14(a) shows the τ–V spectrum obtained using equation 3.5 for r_1–r_{200} in the virtual source gather of Figure 3.12(a). Figure 3.14(b) shows the corresponding τ–V spectrum for r_{200}–r_{500}. At positive times in both spectra,

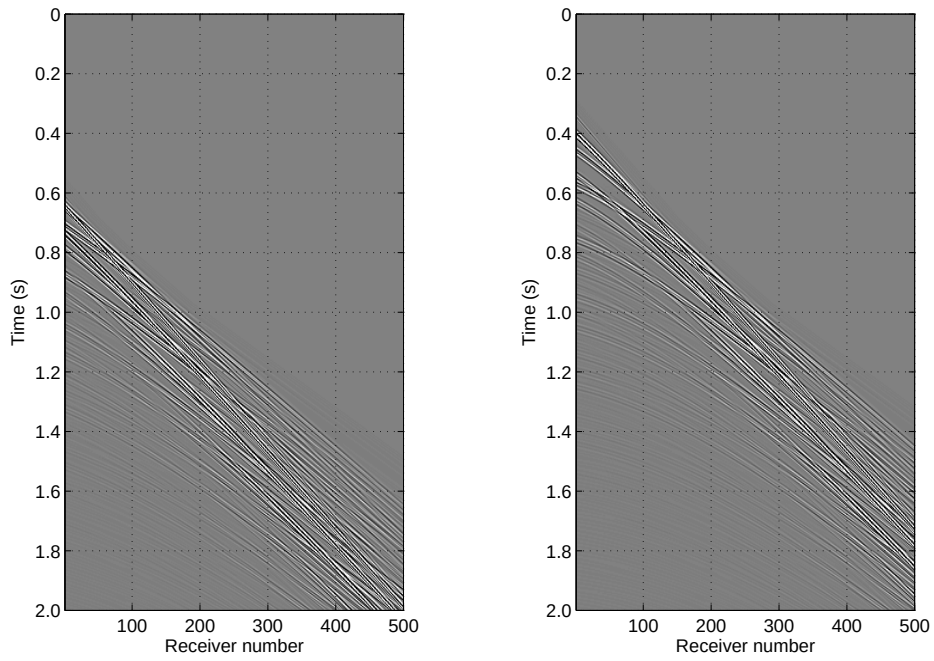

(a) (b)

Figure 3.10: Shot gathers from source 50 (a) and 100 (b) in Figure 3.9.

we observe elliptical energy and spurious peaks that do not correspond to the velocities in the three-layer model. At negative times, we obtain peaks at multiple times τ which correspond to the interval velocities of layers V_2, V_3 and V_4. It is difficult to make assumptions about the thickness of each layer as in the previous example because of the closely-spaced peaks. Notice that in Figure 3.14(a) we do not observe a peak relating to the interval velocity V_4. To record a refraction from the third interface at r_1–r_{200} we require the source-receiver offset to exceed the critical offset (= 1287 m). Although early source numbers are positioned at far enough distance to fulfil this condition, many sources are not and a refraction from the third interface is not recorded for these sources. On the other hand a refraction from the third interface will be recorded and then cross-correlated at r_{200}–r_{500}. This explains why we observe the corresponding peaks in Figure 3.14(b). The above reasoning can also be used to explain why Figure 3.14(b), which considers cross-correlations between receivers located to the right of the virtual source

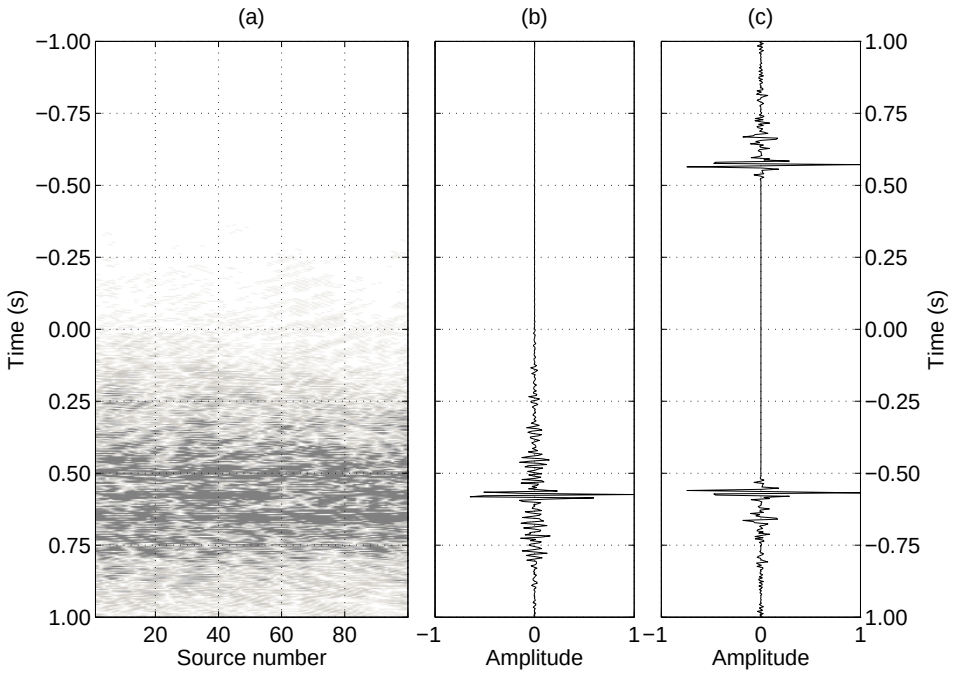

Figure 3.11: (a) Correlation gather for r_{200} and r_{400} for the three layer over a half-space model. (b) Normalized Green's function after summation over source number in (a). (c) Normalized true Green's function.

position, offers better resolution at the correct velocities than Figure 3.14(a) which considers cross-correlations between receivers located to the left of the virtual source position. The cross-correlation between reflections will be more prevalent for r_1–r_{200} and may mask the desired linear refracted energy. The contribution from the cross-correlation of refractions increases for r_{200}–r_{500} as the source-receiver offset exceeds the critical offset. Figure 3.14(c) shows the τ–V spectrum for r_1–r_{250} (i.e., to the left of the virtual source) in the virtual source gather of Figure 3.12(b). Figure 3.14(d) shows the corresponding τ–V spectrum for r_{250}–r_{500}. In Figure 3.14(c) we observe peaks at V_2 and V_3. Again for the reasons described above, peaks at V_4 are obtained only in Figure 3.14(d) when we consider receivers located to the right of the virtual source position.

We can emphasize the linear non-physical refractions and hence the correct velocities, by performing a second cross-correlation of the virtual source gather.

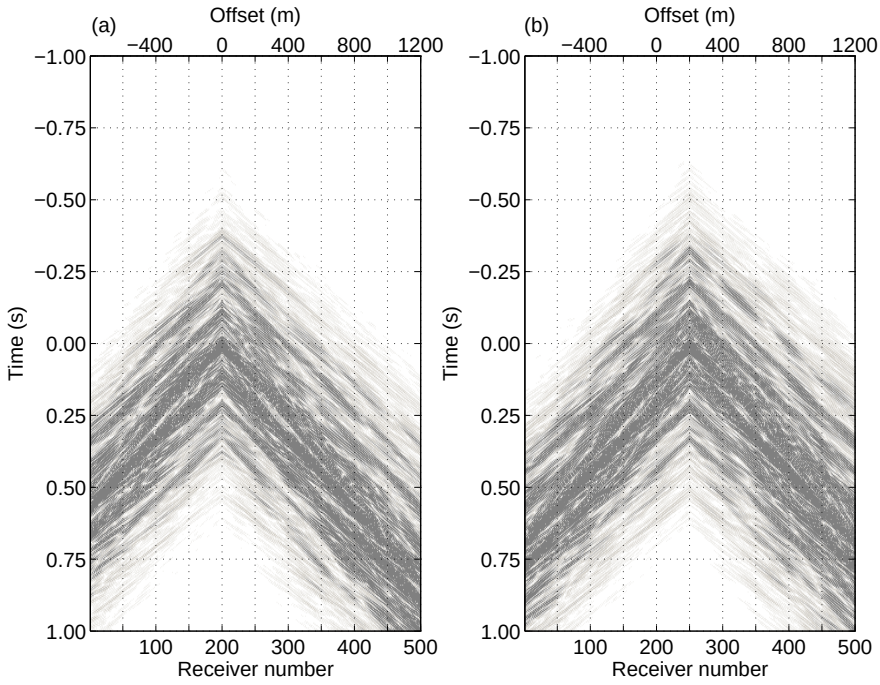

Figure 3.12: Virtual source gathers for the three layer over a half-space model. The virtual source is positioned at (a) r_{200} and (b) r_{250}.

In other words, we produce a new gather by cross-correlating the Green's function estimate at the virtual source position (i.e., the zero-offset Green's function) with the Green's function estimates at the receivers. The procedure has no physical meaning in seismic interferometry but results in new non-physical refractions being shifted upward or downward by the arrival times at the virtual source position. Figure 3.15(a) shows the τ–V spectrum obtained after cross-correlating the estimated Green's functions at r_{250}–r_{500} with the estimated Green's function at r_{250} in the virtual source gather of Figure 3.12(b). At negative times, we achieve two sets of coherent peaks at the correct velocities. Figure 3.15(b) shows the velocity panel after stacking the spectrum in Figure 3.15(a) at negative times. We achieve three peaks positioned close to the expected velocities. These displays confirm our earlier velocity interpretation in Figure 3.14.

We now add random noise, bandlimited to match the source signal, to the source gathers before performing interferometry. The signal-to-noise ratio is equal

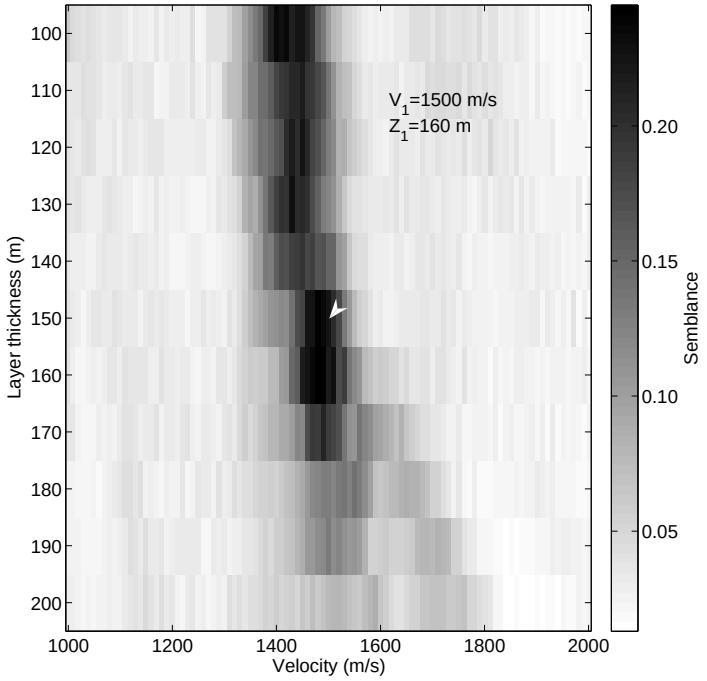

Figure 3.13: Velocity (V_1) – layer thickness (Z_1) spectrum computed from the correlation gather in Figure 3.12(a) using energy up to third-order multiples.

to 1. We consider a virtual source positioned at r_{200}. Figure 3.16(a) shows the τ-V spectrum for r_{200}–r_{500}. We achieve poorly-resolved peaks at V_2 and V_3, but peaks at V_4 are less obvious. We now stack 26 semblance panels which correspond to virtual sources positioned between r_{200} to r_{250} at 2 receiver intervals. Figure 3.16(b) shows the resultant τ-V spectrum. The semblance values are normalized by the number of stacked panels. Much incoherent noise present in Figure 3.16(a) is suppressed during stacking. Peaks at V_2 and V_3 are better resolved and we now obtain, although still weak, a set of peaks at V_4.

3.3.2 More realistic 2.5D model

We apply the same methodology to a more realistic model, based on a North Sea oilfield (Figure 3.17(a)). Figure 3.17(b) shows the acquisition geometry. Figure 3.18 shows the velocity-depth model at a horizontal distance of 2000 m.

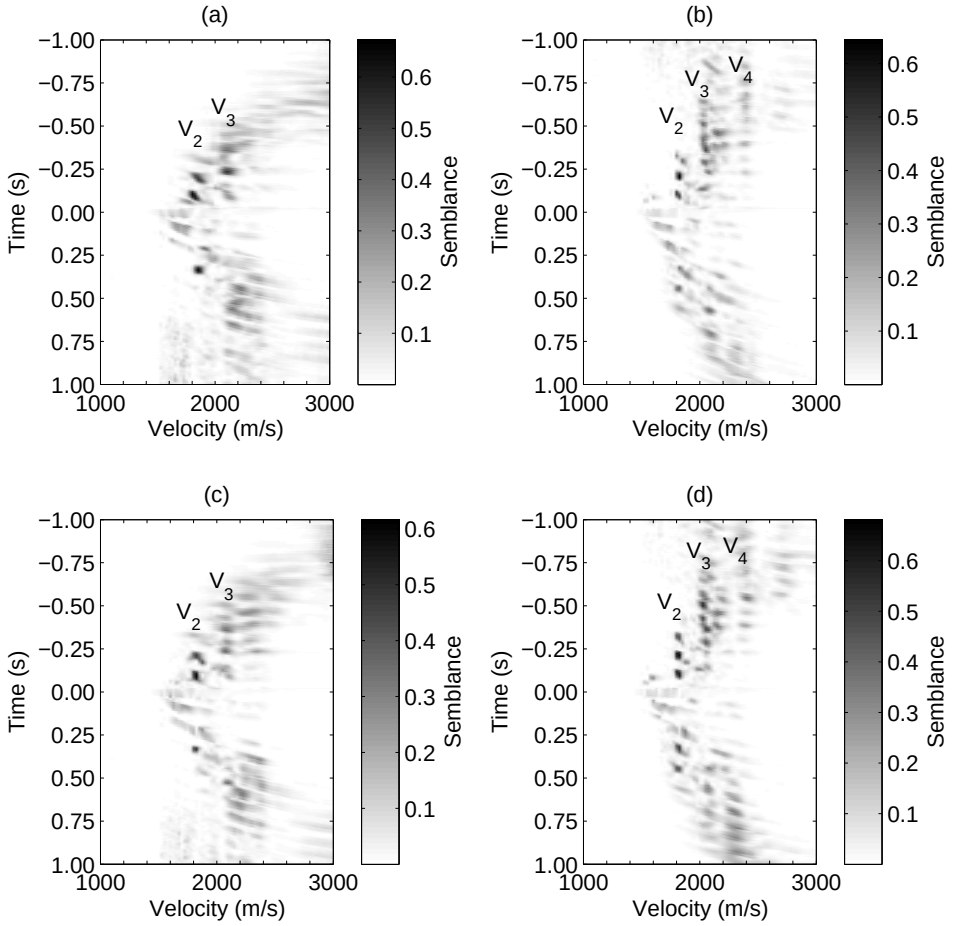

Figure 3.14: Velocity (V) – time (τ) spectra computed using (a) receivers r_1–r_{200} and (b) receivers r_{200}–r_{500} of the virtual source gather in Figure 3.12(a), and (c) receivers r_1–r_{250} and (d) receivers r_{250}–r_{500} of the virtual source gather in Figure 3.12(b).

Figure 3.19 displays two shot gathers from the North Sea model. Figure 3.20 shows the correlation gather for receivers r_1 and r_{35} and Figure 3.21 shows the corresponding velocity–layer-thickness spectrum computed using the reflected energy (equation 2.4) up to the third-order multiples. We obtain the correct velocity and layer thickness of the first layer. Despite the fact that we use a more complex model, our velocity and layer thickness estimate is better resolved than the corresponding estimates in Figure 3.7(a) (single-layer model) and Figure 3.13 (three-layer model). Compared to those examples, our receivers are positioned

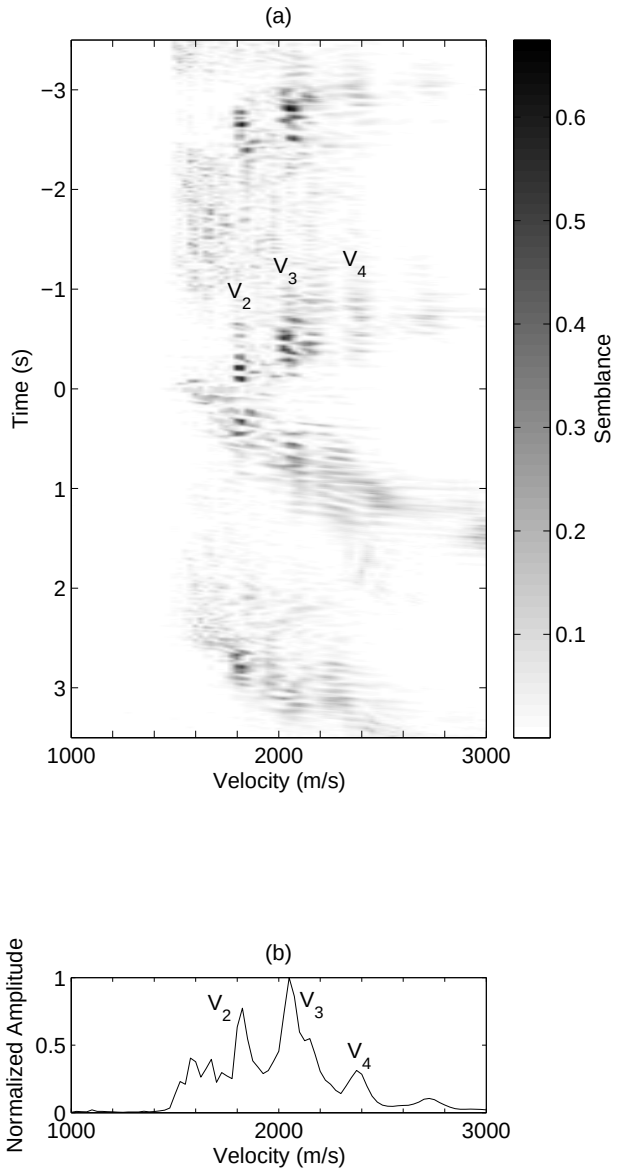

Figure 3.15: (a) Velocity (V) – time (τ) spectra obtained after cross-correlating the records at r_{250} with the records at r_{250}–r_{500} in the virtual source gather of Figure 3.12(b). (b) A velocity panel after a stacking (a) at negative times.

closer to the source array and the layer thickness is greater in this example. Hence, there is a well-defined separation between interfering first-layer reflections in the correlation gather, resulting in a better-defined estimate of the subsurface parameters.

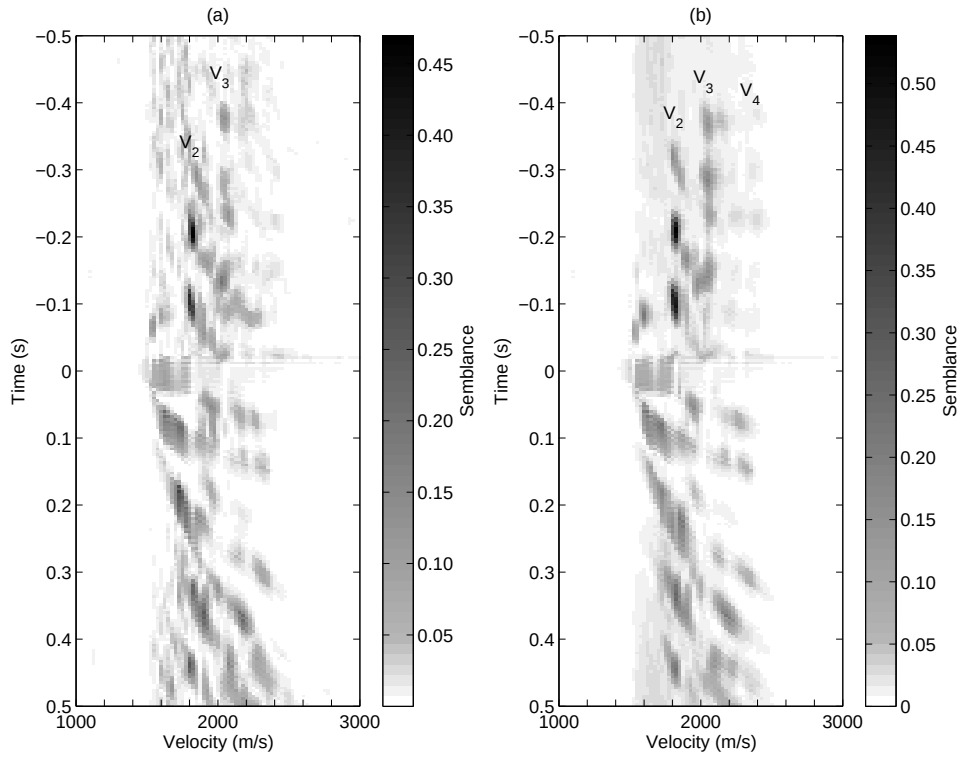

Figure 3.16: Velocity (V) – time (τ) spectrum computed using (a) receivers r_{200}–r_{500} of the virtual source gather in Figure 3.12(a), and (b) after stacking 26 semblance panels corresponding to virtual sources positioned at r_{200} to r_{500} at 2 equal receiver intervals.

Recovery of the first-layer parameters is relatively trivial, however estimating the deeper velocities is more challenging. We now aim to find the refraction velocities of the deeper layers. Figures 3.22(a), (b), (c) and (d) show the virtual source gathers corresponding to the virtual sources positioned at receivers r_{50}, r_{150}, r_{250}, and r_{350}, respectively. Figures 3.23(a) and (b) show the τ–V spectra at negative times using equation 3.5 for r_1– r_{50} and r_{50}–r_{450} from the virtual source gather in Figure 3.22(a) at r_{50}. Figures 3.23(c) and (d) show the τ–V spectra at negative times using equation 3.5 for r_1–r_{150} and r_{150}–r_{450} for the virtual source at r_{150}. We include our interpreted velocities. Figure 3.24 shows the corresponding τ-V spectra for the virtual source gathers in Figure 3.22(c) and (d). A depth interpretation is difficult from such a display; nevertheless, the velocity spectrum

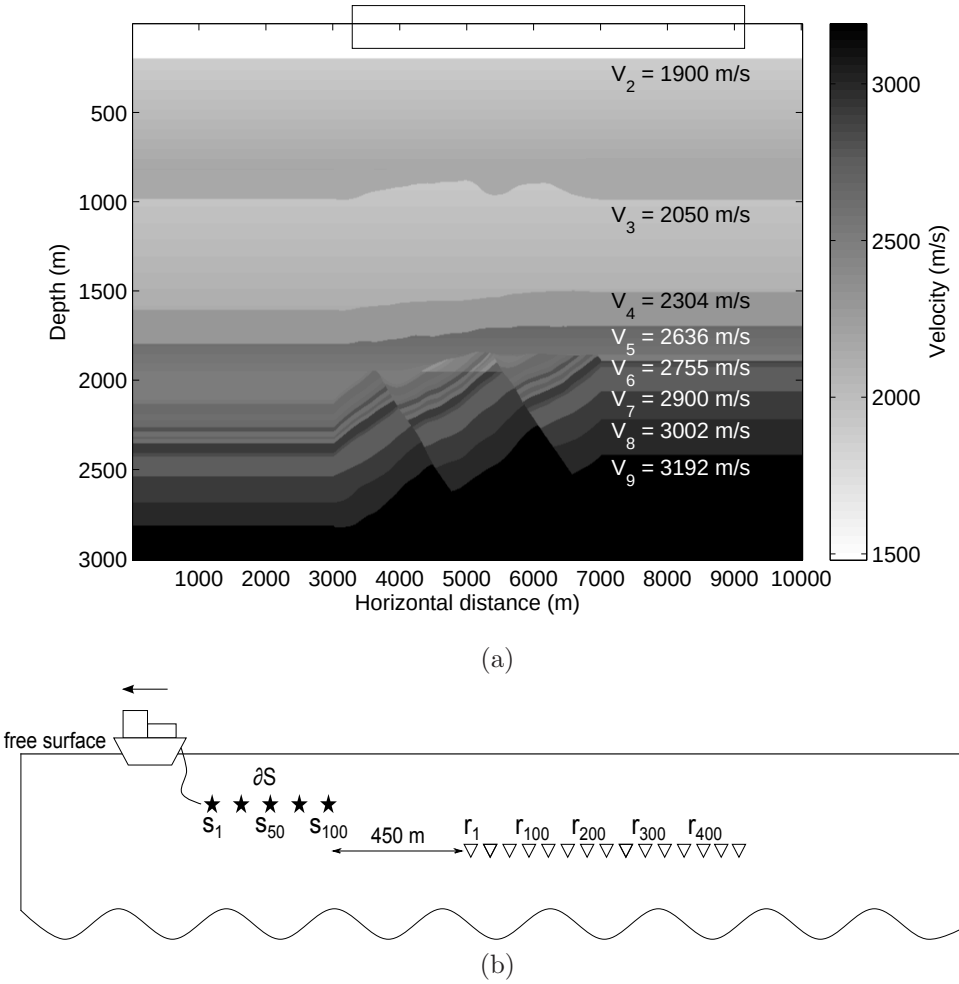

Figure 3.17: (a) More realistic North Sea model. The acquisition geometry (b) is located within the black box in (a). One hundred (100) sources are now spaced every 25 m and 450 receivers are spaced every 12.5 m.

allows us to identify the refraction velocities from a complex model.

3.4 Discussion

In general, the signal-to-noise ratio of refractions can be highly variable along the receiver array (Palmer, 2001). This factor may impact upon methods that use refractions to determine the seismic velocity. We show that seismic interferometry produces repeating non-physical refractions whose velocity can be characterized after a $\tau - p$ transform of the virtual source gather. The repeating nature of these

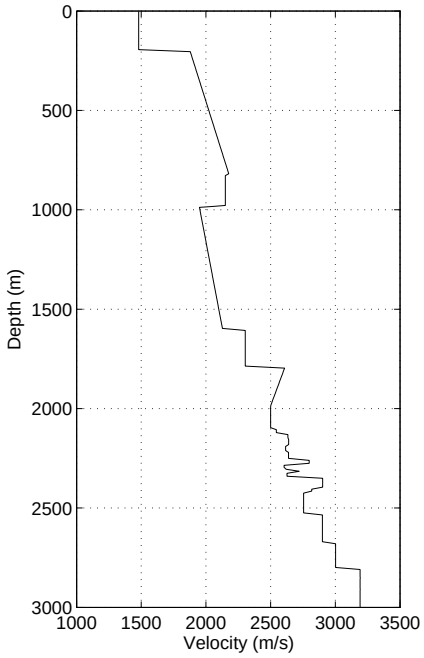

Figure 3.18: Velocity-depth model at horizontal distance 2000 m.

spurious arrivals may help identify refraction velocities in noisy field data.

We note that the method presented here has an advantage over conventional velocity analysis. In cases where the seismic velocity is homogeneous in each layer, we can directly estimate the interval velocities from the cross-correlated refracted energy (as shown in Figure 3.14). Therefore we eliminate the usual requirement to estimate root-mean-square velocities as a first step in order to determine the interval velocity, although we do require long-offset seismic arrays to record the refracted energy.

We have shown that the correlation and virtual source gathers, although linked through seismic interferometry, can be analysed relatively independently. The correlation gather is dominated by reflected energy, useful for determining the properties of the first layer, while the virtual source gather is dominated by non-physical refracted energy, important for determining the remaining seismic velocities of the deeper layers. Rather than being used as an intermediate step

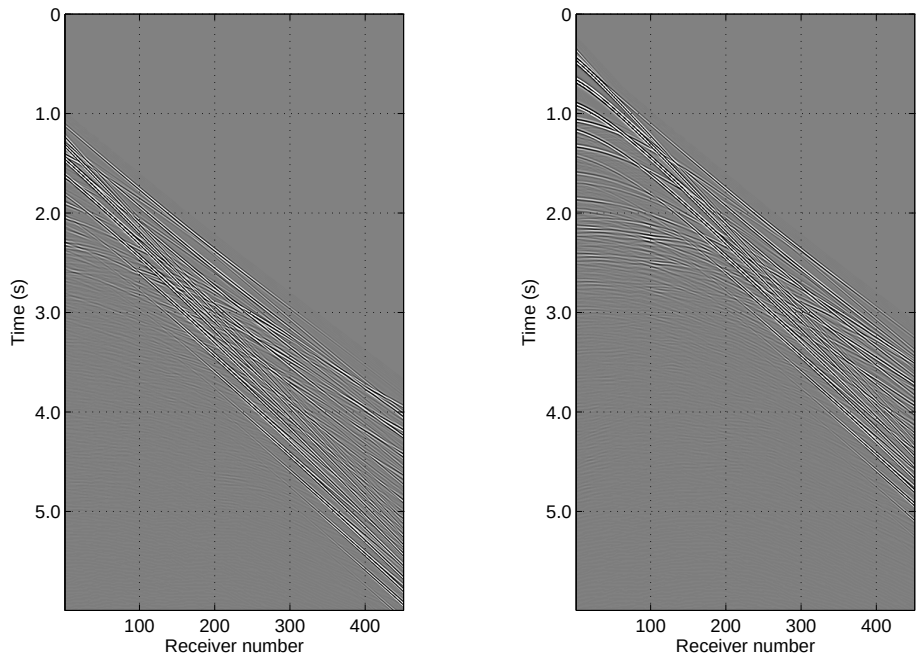

(a) (b)

Figure 3.19: Gather from source 50 (a) and source 100 (b) from the North Sea model.

to obtain the virtual source gather, we have shown that the correlation gather contains useful model information in itself.

In this paper, we have shown that if correctly identified, non-physical energy can be used to extract model information. If we consider a marine-type acquisition geometry such as that in Figure 3.1, studies have shown that the stationary-phase points for reflected energy (between one receiver and another receiver at further offset) are positioned at positive times in the correlation gather (Mikesell et al., 2009). Therefore, after summation over the source boundary we expect physical contributions to dominate over non-physical contributions at positive times in the Green's function estimate. Prior to the stationary-phase point for the primary reflection (e.g., PD in Figure 3.3(b)), the cross-correlation between reflections are non-stationary and sum destructively. We find that the clearest observations of refracted energy are non-physical and occur prior to the direct arrival away from

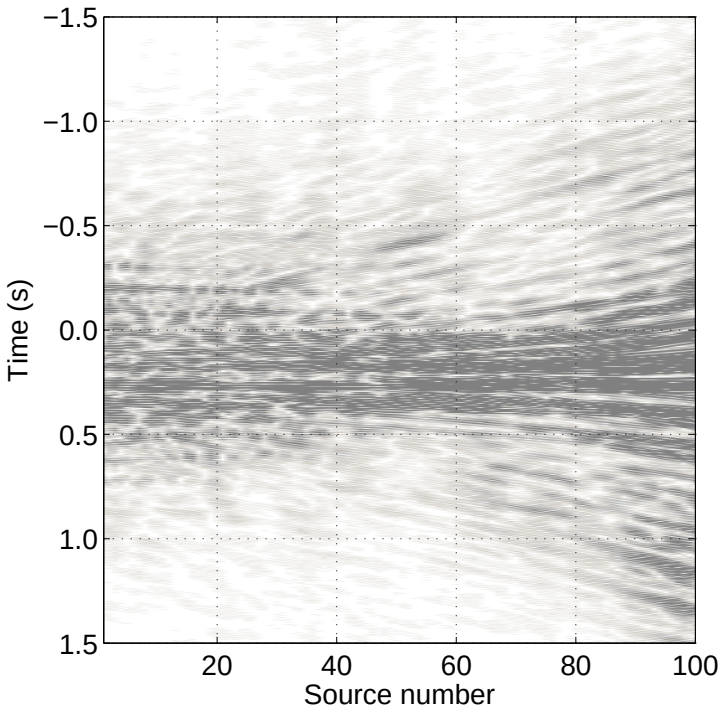

Figure 3.20: Correlation gather for receiver r_1 and r_{35}, for the North Sea model.

the aforementioned dominant reflected energy. Non-physical refractions do exist after the direct arrival (see Figure 3.6); however, they arrive alongside strong reflected energy and hence, their properties are difficult to extract in a semblance analysis. If we wish to understand the contribution of non-physical energy in seismic interferometry, we need to analyse the regions in time and space where their contributions impact most. Methods exist to suppress these non-physical arrivals, or in other words to enhance the physical arrivals in the Green's function estimates (Mehta et al., 2007; Wapenaar et al., 2008; van der Neut and Bakulin, 2009; Curtis and Halliday, 2010a). We show here that the non-physical arrivals dominate over the physical arrivals in the case of one-sided illumination. Hence, using the non-physical arrivals to characterize the model may be more appropriate than suppressing them.

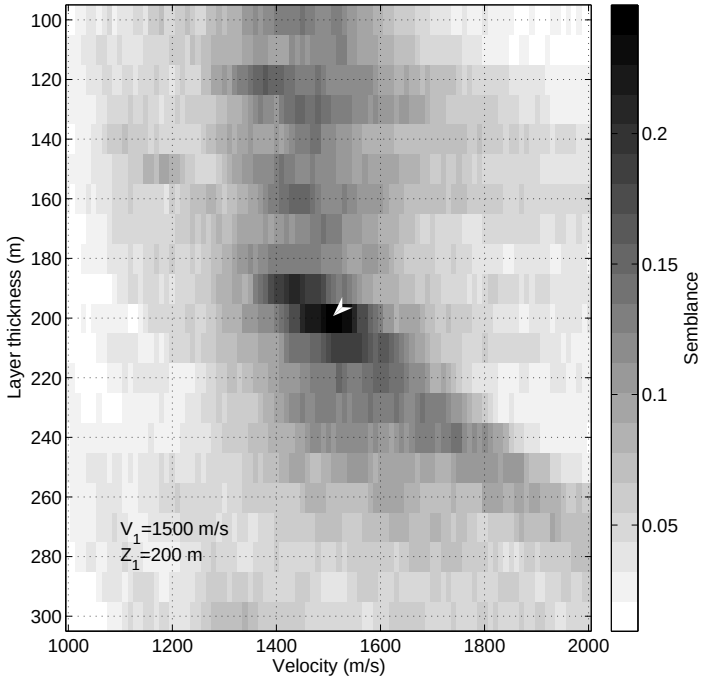

Figure 3.21: Velocity (V_1) – layer-thickness (Z_1) spectrum computed from the North Sea correlation gather using energy up to the third-order multiples.

3.5 Conclusions

In seismic interferometry, the Green's functions between two receivers can be extracted by cross-correlating and summing the Green's functions from an illuminating and surrounding source boundary. The Green's functions obtained in a marine seismic setting with a non-surrounding source boundary are dominated by non-physical or so-called spurious arrivals. We show that the imperfect Green's functions still provide important information about the subsurface velocity – essential information for imaging or migration. Unravelling this information can be challenging when non-physical arrivals dominate the Green's function estimates and bias normal velocity analysis methods. Therefore, new analysis procedures have to be considered.

We show that the reflected and refracted energy in the correlation and virtual source gathers can be analyzed independently and used to obtain information

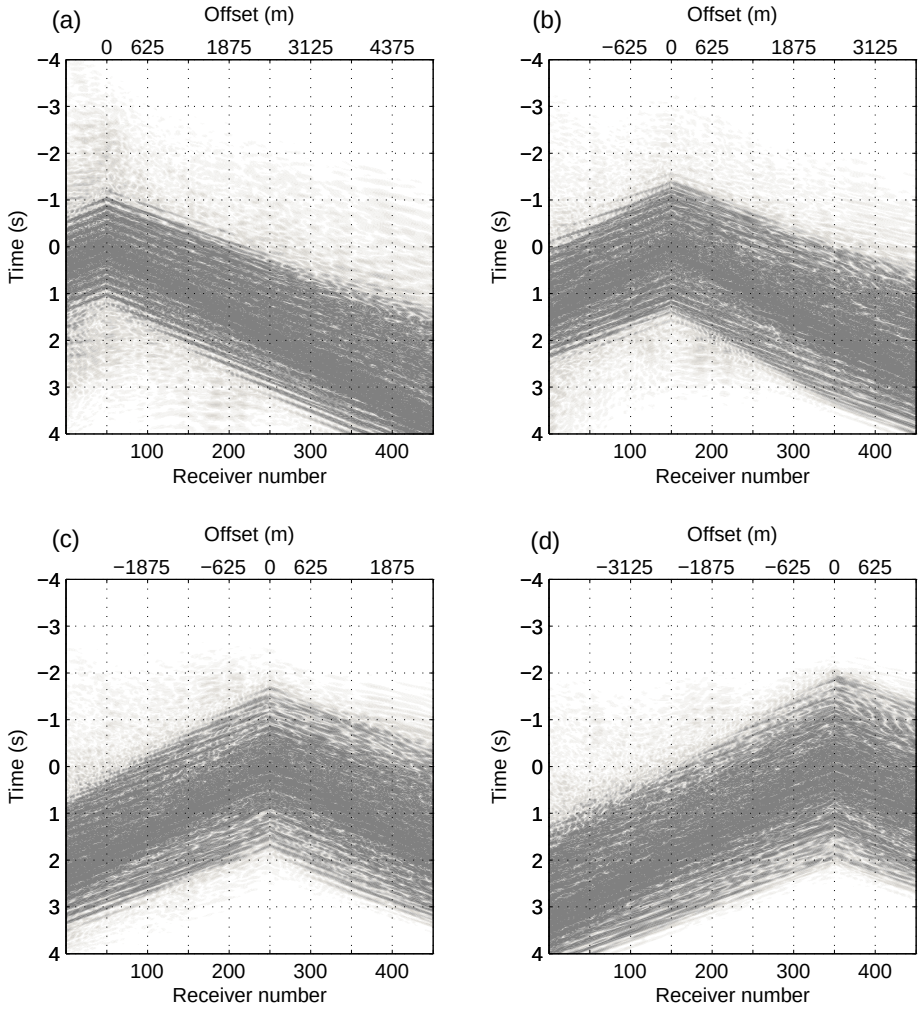

Figure 3.22: Virtual source gathers for the North Sea model. Virtual source positioned at receiver r_{50} (a), r_{150} (b), r_{250} (c) and r_{350} (d).

about the seismic velocity of subsurface strata. Specifically, when the source boundary is one-sided and the receivers are positioned at far offset, we show that the cross-correlations (the Green's functions before summation over the source boundary) are dominated by reflected energy which can be used in a semblance analysis to determine the seismic velocity and thickness of the first layer. Once these cross-correlations are summed over the boundary of sources, the Green's function estimates are dominated by non-physical refracted energy. A semblance analysis on these Green's functions determines refraction velocities of the deeper

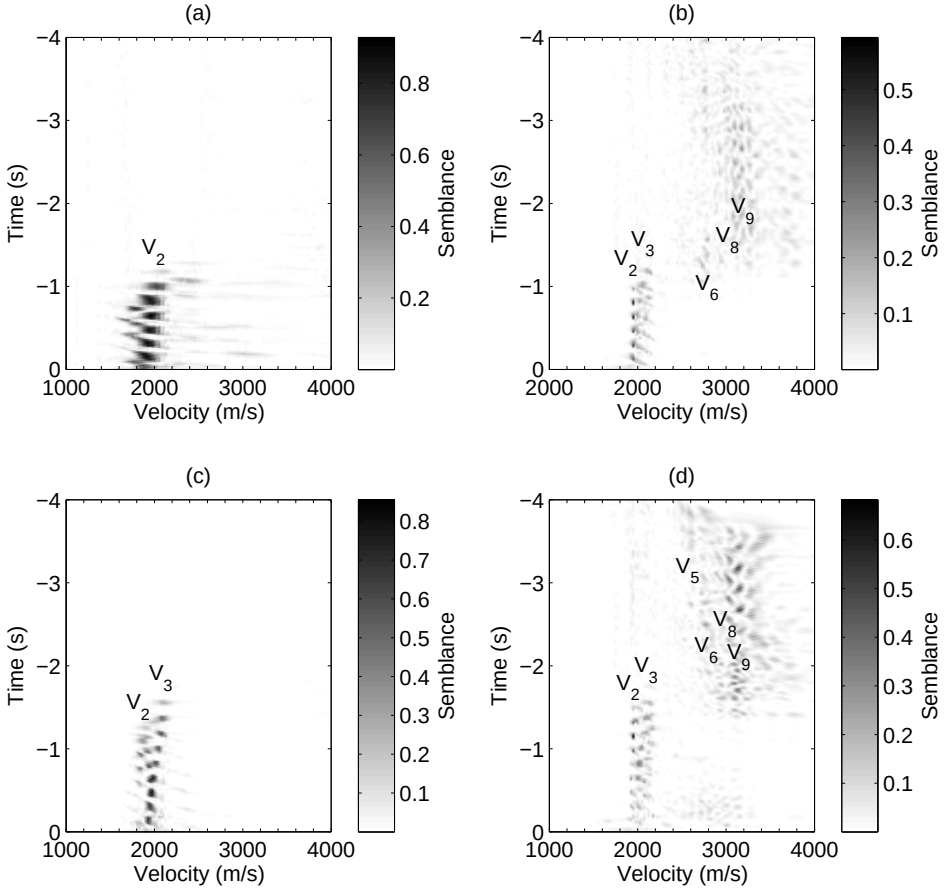

Figure 3.23: Velocity (V) – time (τ) spectra computed using (a) receivers r_1–r_{50} and (b) receivers r_{50}–r_{450} from the virtual source at r_{50}, and (c) receivers r_1-r_{150} and (d) receivers r_{150}-r_{450} from the virtual source at r_{150}.

layers. We demonstrate the velocity analysis procedure on a synthetic single layer over half-space model, and a three layer over a half-space model before applying the approach to a more realistic model based on a North Sea oilfield. In all examples, we were able to estimate the seismic velocity using a combination of physical and non-physical arrivals.

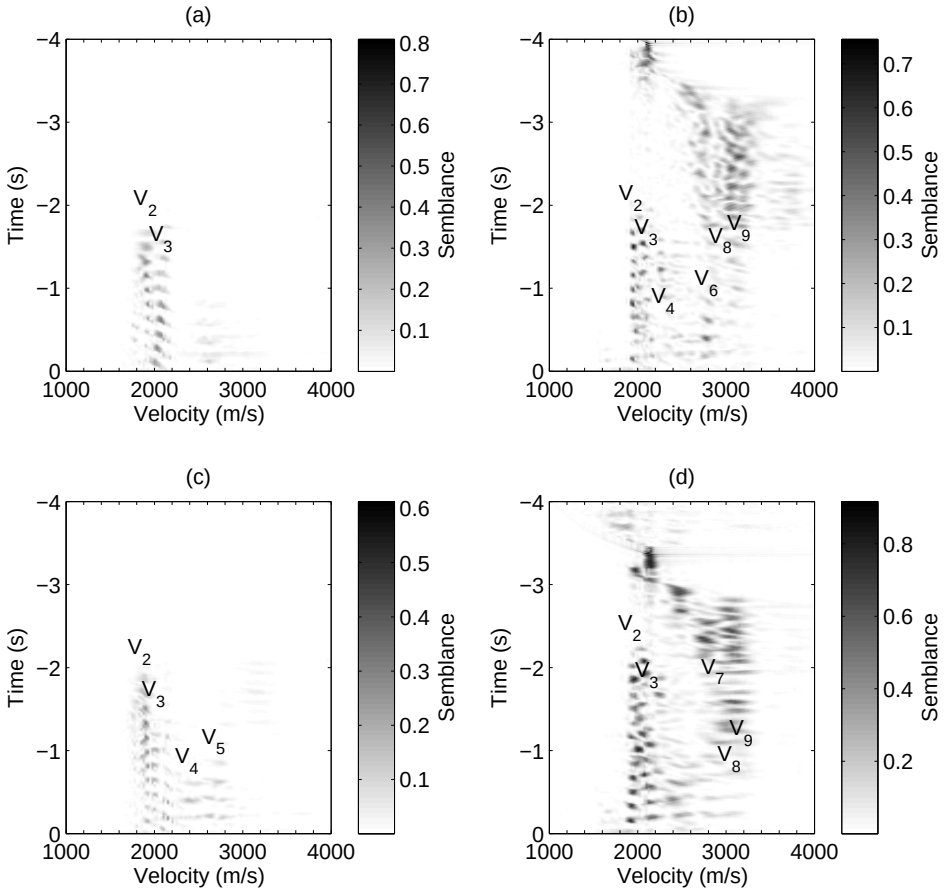

Figure 3.24: Velocity (V) – time (τ) spectra computed using (a) receivers r_1–r_{250} and (b) receivers r_{250}–r_{450} from the virtual source at r_{250}, and (c) receivers r_1-r_{350} and (d) receivers r_{350}-r_{450} from the virtual source at r_{350}.

Chapter 4

Suppressing non-physical reflections in Green's function estimates using source-receiver interferometry

The theory of seismic interferometry requires that sources completely surround the two receivers, but constraints in exploration seismology restrict sources to locations near the surface of the Earth. Seismic interferometry by cross-correlation then introduces usually-undesirable non-physical reflections (spurious multiples) in the Green's function estimates. We show that the dominant non-physical reflections can be converted into physical reflections via convolution using source-receiver interferometry. The resultant Green's functions display fewer non-physical reflections and show significantly better agreement with the true Green's functions than those obtained using cross-correlational interferometry. Non-physical reflections can be further suppressed by iterating the convolution step. By comparing the velocity spectra of the Green's functions retrieved by cross-correlational and source-receiver interferometry, we can retrospectively iden-

tify the dominant non-physical reflections introduced by cross-correlational interferometry.

We show that the non-physical reflections are particularly important for constructing the primary reflections and internal multiples in source-receiver interferometry. This is because the primary reflections and internal multiples cannot be created via the convolution of physical reflections. Instead, the primary reflections and internal multiples are retrieved by the appropriate convolution between a non-physical and physical reflection. We compare cross-correlational interferometry and source-receiver interferometry using synthetic towed streamer data for a 1D acoustic and 2.5D elastic model, respectively. We also show that the non-physical reflections obtained using cross-correlational interferometry allow for the direct estimation of interval velocities and layer thicknesses without the need to use Dix inversion in the 1D example.

Thus, this Chapter shows first that there is substantial information about the physical Green's functions within the unknown non-physical reflections and second that there are good theoretical reasons why source-receiver interferometry might out-perform cross-correlational interferometry in some situations, as has been observed previously in real data from the field.

4.1 Introduction

The theory of seismic interferometry requires we have a complete boundary of sources that surround the two receivers, but practicalities limit the illuminating sources to locations near or on the surface of the Earth (so-called surface sources). When only surface sources are available, non-physical reflections are produced in the Green's function estimates. These are formed by the cross-correlation of reflections from different interfaces, and are called spurious multiples by Snieder

et al. (2006b).

Non-physical reflections would cancel by destructive interference if the surface sources were supplemented by sources at depth (see Figure 14 in Snieder et al. (2006b)), or by wavefields which scatter back toward the receivers by a sufficiently inhomogeneous medium (Wapenaar, 2006). Non-physical reflections can also be suppressed if we decompose the recorded wavefields prior to cross-correlation. Bakulin and Calvert (2006) show that improved Green's function estimates between receivers in a horizontal well are obtained by cross-correlating the full wavefield Green's function with the time-windowed direct arrivals at the virtual source. Mehta et al. (2007) instead perform up/down decomposition at ocean-bottom receivers, which allows the upgoing wavefield to be cross-correlated with the time-windowed downgoing direct arrivals. The physical reflections are well recovered in both methods because cross-correlational seismic interferometry essentially removes the common component of the reflection that passes through both receivers (Figure 4.1(a)). Also, by omitting the reflected wavefields from Green's functions at $\mathbf{x}_A$ for example, the aforementioned methods do not produce cross-correlations between different reflections, and thus unwanted non-physical reflections are suppressed.

The suppression methods of Bakulin and Calvert (2006) and Mehta et al. (2007) are only applicable when receivers are positioned vertically beneath surface sources (e.g., Figure 4.1(a)). However, these methods fail to recover the physical reflections when receivers are positioned adjacent to surface sources as in towed streamer recordings. In that case the direct arrival travels horizontally along the receiver array and hence, does not share a common component of the recorded reflections as demonstrated in Figure 4.1(a). For this reason the Green's functions are best obtained in towed streamer data by cross-correlating the reflections at both receivers. For example, Schuster et al. (2004) show that the cross-correlation of a first-order free-surface multiple with a ghost reflection isolates the Green's

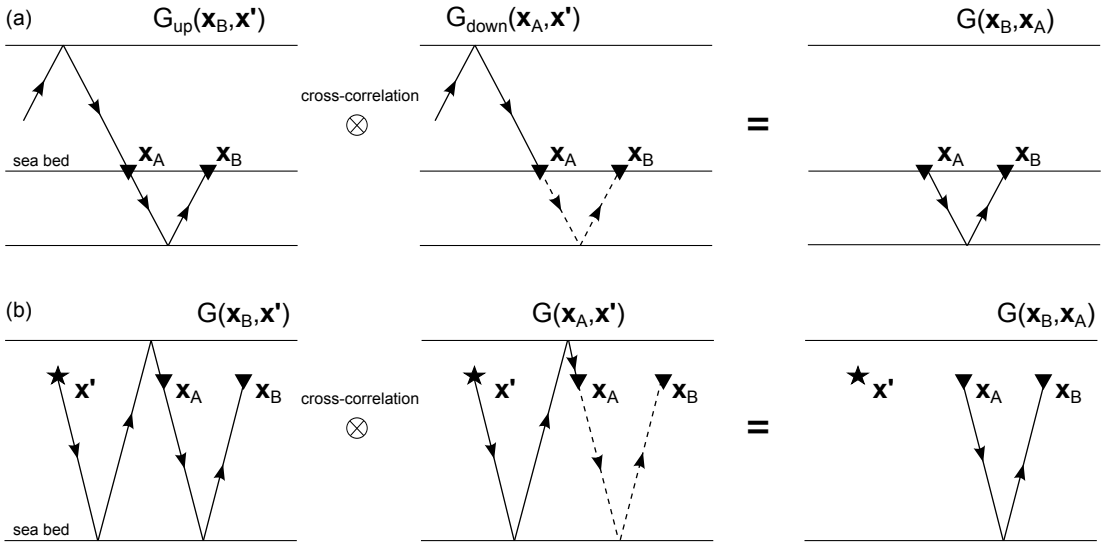

Figure 4.1: (a) Cross-correlation of the upgoing Green's function recorded at $\mathbf{x}_B$ (*left*) with the downgoing Green's function recorded at $\mathbf{x}_A$ (*middle*) isolates the traveltime of the primary reflection between the receiver locations (*right*). The common portion of the reflection which is annihilated in this case is the direct arrival recorded at $\mathbf{x}_A$. (b) Cross-correlation of the first-order free-surface multiple at $\mathbf{x}_B$ (*left*) with the ghost reflection at $\mathbf{x}_A$ (*middle*) isolates the traveltime of the primary reflection between the receiver locations (*right*).

function kinematically equivalent to the primary reflection between the two receivers (Figure 4.1(b)). Such a formulation allows the physical components of Green's functions to be constructed, but unfortunately introduces the undesirable non-physical reflections as described above.

It has recently been observed in a field data set that inter-receiver Green's function estimates obtained using source-receiver interferometry were of better quality than those obtained by cross-correlational or cross-convolutional interferometry (Duguid et al., 2011). To-date, no explanation of why this should be the case has been proposed. In this Chapter we show that the dominant non-physical reflections obtained using sources and receivers in a towed streamer configuration from cross-correlational seismic interferometry, can be used constructively in source-receiver interferometry to obtain Green's function estimates with fewer non-physical reflections. Essentially, source-receiver interferometry includes a step which allows many of the non-physical reflections to be converted back into

physical reflections via convolution. In this instance we use a modified version of source-receiver interferometry to obtain Green's functions between receivers only. While this may not provide a full explanation of the results of Duguid et al. (2011), it does provide a basis with which we might expect the quality improvement to be observed in more general applications of source-receiver interferometry.

In the next section we outline cross-correlational and source-receiver interferometry and describe the methodology whereby non-physical reflections can be used constructively in source-receiver interferometry to produce physical reflections. We then demonstrate the phenomenon on a 1D acoustic model and subsequently on a 2.5D model based on a North sea oilfield. We finish by discussing the implications and limitations of this work.

4.2 Methodology

To avoid the requirement for both monopolar and dipolar sources, Wapenaar and Fokkema (2006) show that if sources lie in the far-field of the receivers, the Green's function $G(\mathbf{x}_B, \mathbf{x}_A)$ between two receivers positioned at $\mathbf{x}_A$ and $\mathbf{x}_B$ plus its complex conjugate is approximated by the cross-correlation of wavefields from only monopolar sources:

$$G(\mathbf{x}_B, \mathbf{x}_A) + G^*(\mathbf{x}_B, \mathbf{x}_A) \approx \oint_{\partial S_1} \frac{2}{\rho c} G(\mathbf{x}_B, \mathbf{x}') G^*(\mathbf{x}_A, \mathbf{x}') d^2\mathbf{x}', \tag{4.1}$$

where ρ and c are the density and velocity, respectively, and are assumed to be constant at each source positioned at $\mathbf{x}'$ on a boundary ∂S_1. The Green's functions on the right-hand side represent pressure responses at the receiver locations $\mathbf{x}_A$ and $\mathbf{x}_B$ from impulsive pressure sources at $\mathbf{x}'$. Assuming the Green's functions are excited by a source wavelet $s(\omega)$, e.g., $s(\omega)G(\mathbf{x}_A, \mathbf{x}')$, the right-hand side of equation 4.1, would in theory include the power spectrum of the source wavelet $|s(\omega)|^2$. Integrating the cross-correlations over the total number of sources (closed

integral in equation 4.1) isolates the Green's function $G(\mathbf{x}_B, \mathbf{x}_A) + G^*(\mathbf{x}_B, \mathbf{x}_A)$ as though a source was fired at $\mathbf{x}_A$ and the response recorded at $\mathbf{x}_B$. Equation 4.1 is the simplified acoustic approximation in seismic interferometry.

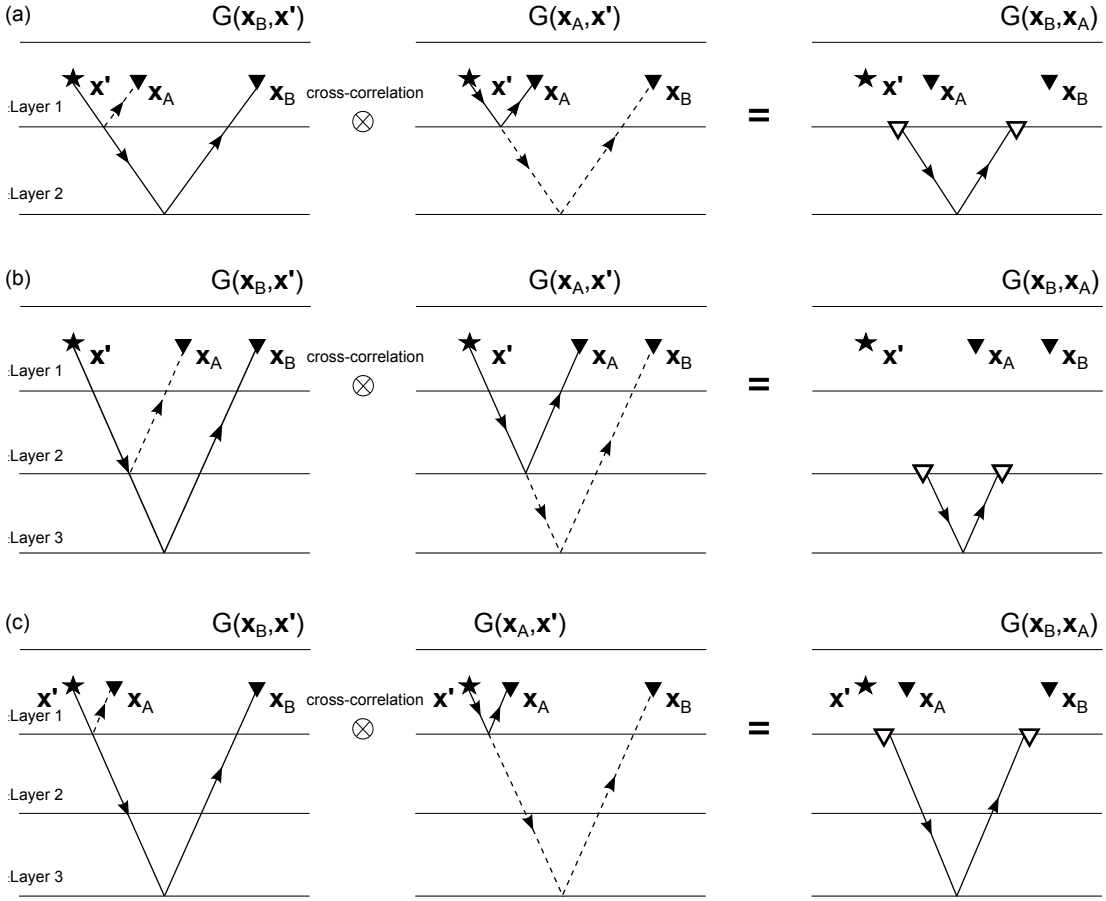

Figure 4.2: Non-physical reflections in cross-correlational seismic interferometry. (a) Cross-correlation of the primary reflection from the second interface at $\mathbf{x}_B$ (*left*) with the primary reflection from the first interface at $\mathbf{x}_A$ (*middle*) isolates a non-physical reflection from the second interface (*right*), as though the virtual source and receiver were positioned at the first interface (open triangles). (b) Cross-correlation of the primary reflection from the third interface at $\mathbf{x}_B$ (*left*) with the primary reflection from the second interface at $\mathbf{x}_A$ (*middle*) isolates a non-physical reflection from the third interface (*right*), as though the virtual source and receiver were positioned at the second interface (open triangles). (c) Cross-correlation of the primary reflection from the third interface at $\mathbf{x}_B$ (*left*) with the primary reflection from the first interface at $\mathbf{x}_A$ (*middle*) isolates a non-physical reflection from the third interface (*right*), as though the virtual source and receiver were positioned at the first interface (open triangles).

We illustrated in Figure 4.1 for a simple 1D medium that cross-correlational

interferometry (equation 4.1) removes the traveltime associated with the common component of the wavefield that passes through both receivers, resulting in waves that have the traveltimes of physical reflections. However, the same process synthesizes waves with the traveltime of a non-physical reflection by cross-correlation of the primary reflection from two different interfaces, for example the primary reflection from the second interface recorded at $\mathbf{x}_B$ cross-correlated with the primary reflection from the first interface recorded at $\mathbf{x}_A$ (Figure 4.2(a)). The non-physical reflection can be intuitively interpreted as the wavefield reflected from the second interface as though the virtual source and receiver were positioned at the first interface. As shown on the right-hand side of Figure 4.2(a), the retrieved Green's function is positioned to the left of the two receivers. However, in a laterally invariant medium the retrieved Green's function could just as well be shifted to the right to represent the reflection propagating directly between the receivers. The cross-correlation between the primary reflection from the third interface with the primary reflection from the second interface provides the traveltime of a non-physical reflection corresponding to a reflection propagating through the third layer only (Figure 4.2(b)). A non-physical reflection that propagates through two layers is provided by the cross-correlation of the primary reflections shown in Figure 4.2(c). What can be observed immediately, is that some of these non-physical reflections are sensitive only to the velocity within a single layer (Figures 4.2(a) and 4.2(b)). We will investigate this property below to provide a new velocity analysis method that uses non-physical reflections to identify individual layer velocity directly, without the need for Dix inversion (Dix, 1955).

Whilst cross-correlational interferometry subtracts the traveltimes of the two recorded wavefields, cross-convolutional interferometry adds the traveltimes of the two wavefields. For example, given a source positioned midway between two receivers the cross-convolution of two appropriately chosen primary reflections,

one propagating forward and one propagating backward, isolates the traveltime of a first-order free-surface multiple. To obtain the cross-convolutional Green's function we remove the complex conjugate from equation 4.1:

$$G(\mathbf{x}_B, \mathbf{x}_A) \approx \oint_{\partial S_2} \frac{2}{\rho c} G(\mathbf{x}_B, \mathbf{x}'') G(\mathbf{x}_A, \mathbf{x}'') d^2\mathbf{x}''. \tag{4.2}$$

Equation 4.2 is the far-field acoustic approximation to cross-convolutional interferometry and is similar to the integral derived by Poletto and Wapenaar (2009) used to obtain the Green's function as though there had been a reflector at the source boundary. Now it is necessary that receiver $\mathbf{x}_A$ is positioned outside of the source boundary whilst the remaining receivers are co-located with sources on the boundary ∂S_2 (Figure 4.3(a)). Unfortunately in marine exploration seismology it is unlikely that we have access to a receiver towed in front of the source at $\mathbf{x}_A$. However, we can circumvent this by constructing the forward-time Green's functions $\tilde{G}(\mathbf{x}'', \mathbf{x}_A)$ using cross-correlational interferometry with the source boundary ∂S_1 (Figure 4.3(b)):

$$\tilde{G}(\mathbf{x}'', \mathbf{x}_A) + \tilde{G}^*(\mathbf{x}'', \mathbf{x}_A) \approx \oint_{\partial S_1} \frac{2}{\rho c} G(\mathbf{x}'', \mathbf{x}') G^*(\mathbf{x}_A, \mathbf{x}') d^2\mathbf{x}'. \tag{4.3}$$

The tilde on the left-hand side of equation 4.3 represents the fact that $\mathbf{x}''$ and $\mathbf{x}_A$ may not be in the correct position (e.g., Figure 4.2). By source-receiver reciprocity, the Green's function $\tilde{G}(\mathbf{x}'', \mathbf{x}_A)$ on the left-hand side of equation 4.3 is equivalent to that required by cross-convolutional interferometry as sketched in Figure 4.3(a).

Substituting only the forward-time (t_+) Green's functions $\tilde{G}(\mathbf{x}'', \mathbf{x}_A) = \tilde{G}(\mathbf{x}_A, \mathbf{x}'')$ obtained from equation 4.3 into the cross-convolutional equation 4.2 we obtain the Green's function between receivers positioned at $\mathbf{x}_A$ and $\mathbf{x}_B$,

$$G(\mathbf{x}_B, \mathbf{x}_A) \approx \frac{4}{\rho^2 c^2} \int_{\partial S_2} \int_{\partial S_1} \Big[G(\mathbf{x}'', \mathbf{x}') G^*(\mathbf{x}_A, \mathbf{x}') \Big]_{t_+} G(\mathbf{x}_B, \mathbf{x}'') d^2\mathbf{x}' d^2\mathbf{x}''. \tag{4.4}$$

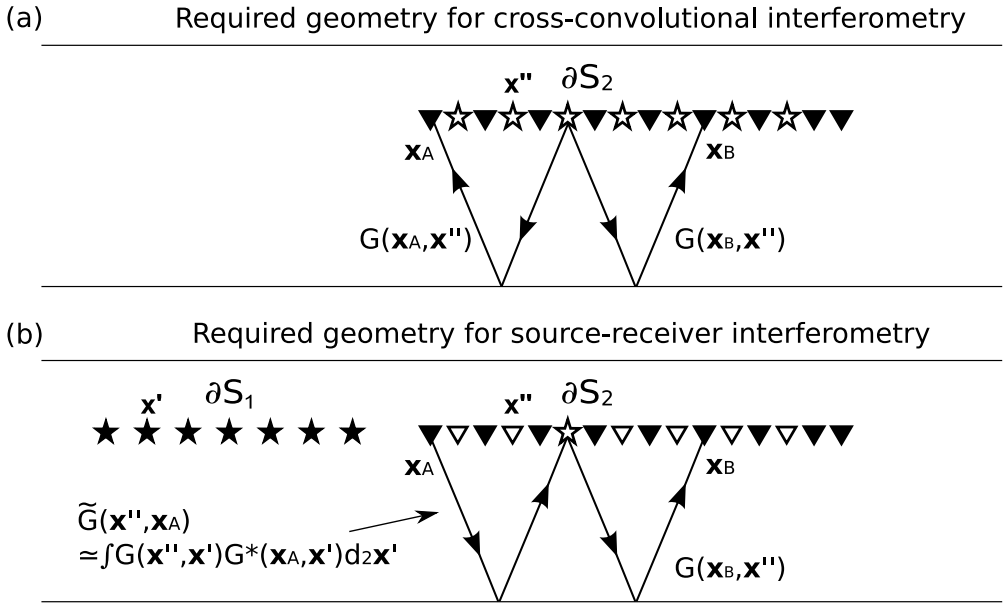

Figure 4.3: Acquisition geometries required for cross-convolutional (a) and source-receiver interferometry (b). The traveltime of the Green's function $G(\mathbf{x}_A, \mathbf{x}'')$ required by cross-convolutional interferometry (a) is equivalent to the traveltime of the Green's function $G(\mathbf{x}'', \mathbf{x}_A)$ obtained using cross-correlational interferometry (b). ∂S_1 and ∂S_2 represent the source boundaries from cross-correlational and cross-convolutional interferometry, respectively. For simplicity, we ignore free-surface effects in the sketch.

The outer integral assumes that sources and receivers are co-located on the boundary ∂S_2. We do not explicitly include it here, but convolution in equation 4.4 would result in $|s(\omega)|^3$ being introduced on the right-hand side. Equation 4.4 represents an approximation to acoustic source-receiver interferometry.

An interesting aspect about source-receiver interferometry is that the non-physical reflections created by cross-correlational interferometry in the first step (square brackets in equation 4.4) contribute to the traveltime of physical reflections when convolved with the reflected Green's functions $G(\mathbf{x}_B, \mathbf{x}'')$ in the second step. We demonstrate this in Figure 4.4 which shows the construction of a primary reflection, free-surface multiple and an internal multiple in source-receiver interferometry using non-physical reflections in a laterally invariant

medium. For example, the traveltime of the primary reflection from the third interface is recovered by convolving the non-physical reflection previously obtained by cross-correlational interferometry in Figure 4.2(b), with the primary reflection from the second interface (Figure 4.4(a)). Similar combinations between primaries and non-physical reflections provide the traveltime of the other primary reflections.

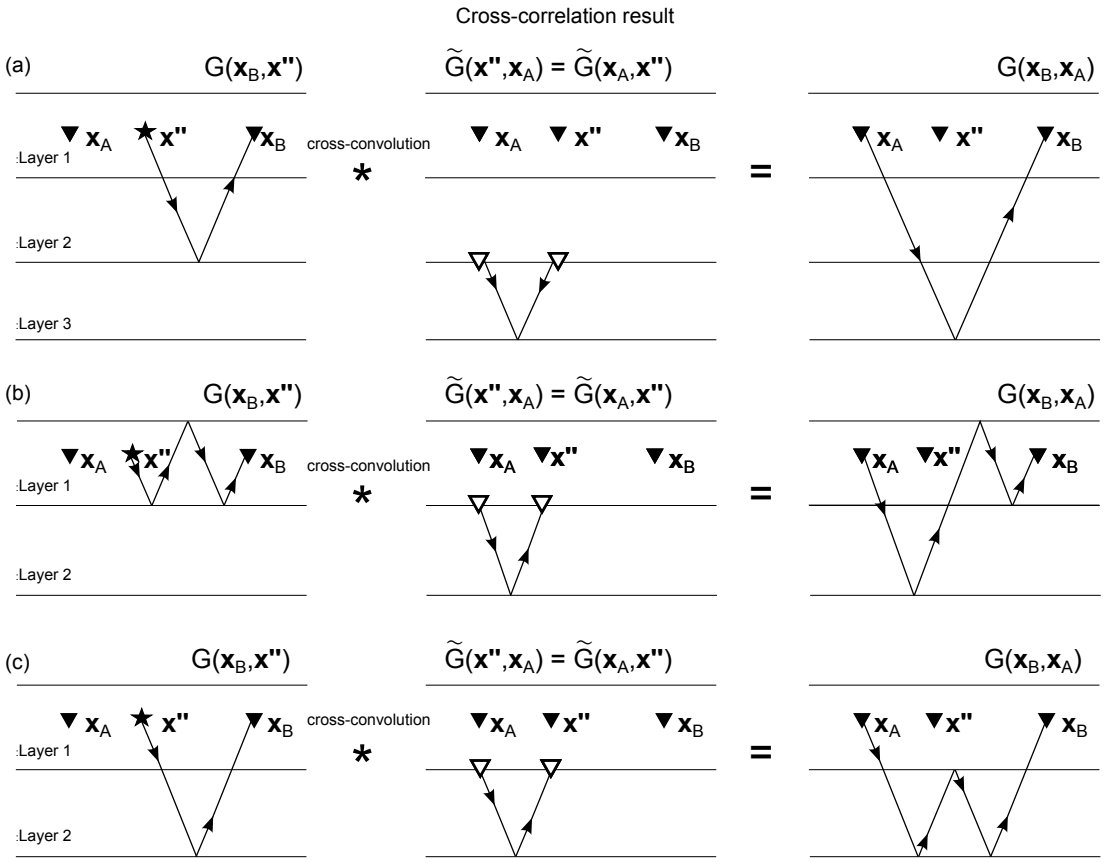

Figure 4.4: The construction of physical reflections using non-physical reflections in source-receiver interferometry. (a) Cross-convolution of the primary reflection from the second interface (*left*) with the non-physical reflection from the third interface as though the virtual source and receiver were positioned at the second interface (*middle*) isolates the primary reflection from the third interface. (b) Cross-convolution of a free-surface multiple (*left*) with the non-physical reflection from the second interface as though the virtual source and receiver were positioned at the first interface (*middle*) isolates the free-surface multiple between receiver locations (*right*). (c) Cross-convolution of the primary reflection from the second interface (*left*) with the non-physical reflection from the second interface as though the virtual source and receiver were positioned at the first interface (*middle*) isolates the internal multiple between receiver locations (*right*).

In the derivation of equation 4.4, we used cross-correlational interferometry to solve the problem of never having a receiver in front of the source (equation 4.3). At first, this step would seem unnecessary because in a 1D medium the corresponding physical Green's functions could be replicated by simply choosing the appropriate source to receiver offset. We instead use cross-correlational interferometry because the purpose of this Chapter is to show how non-physical reflections synthesised by that method can be combined to create physical primary reflections by using convolution.

Equation 4.4 appears similar to that derived in source-receiver interferometry (see equation 10 in Curtis and Halliday (2010b)). However, in principle the two equations are different: in equation 4.4 we obtain the Green's function between two receivers using two source boundaries whereas Curtis and Halliday (2010b) retrieve the Green's function between a source and receiver using two boundaries, one of sources and another of receivers. Curtis and Halliday (2010b) adopt the following approach. In the first step, the Green's functions between the receiver and the receivers on the boundary are obtained from cross-convolutional interferometry using Green's functions from a boundary of sources. This creates a virtual source at the receiver location alongside the original source. In the second step, the desired Green's function between the source and virtual source (previously the receiver) is obtained from cross-correlational interferometry using recordings at the receiver boundary. The term source-receiver interferometry is entirely appropriate for equation 4.4 because in the first step we turn a receiver into a virtual source using cross-correlational interferometry and in the second step, we convolve the virtual source recordings with recordings at the other receivers using a second source boundary.

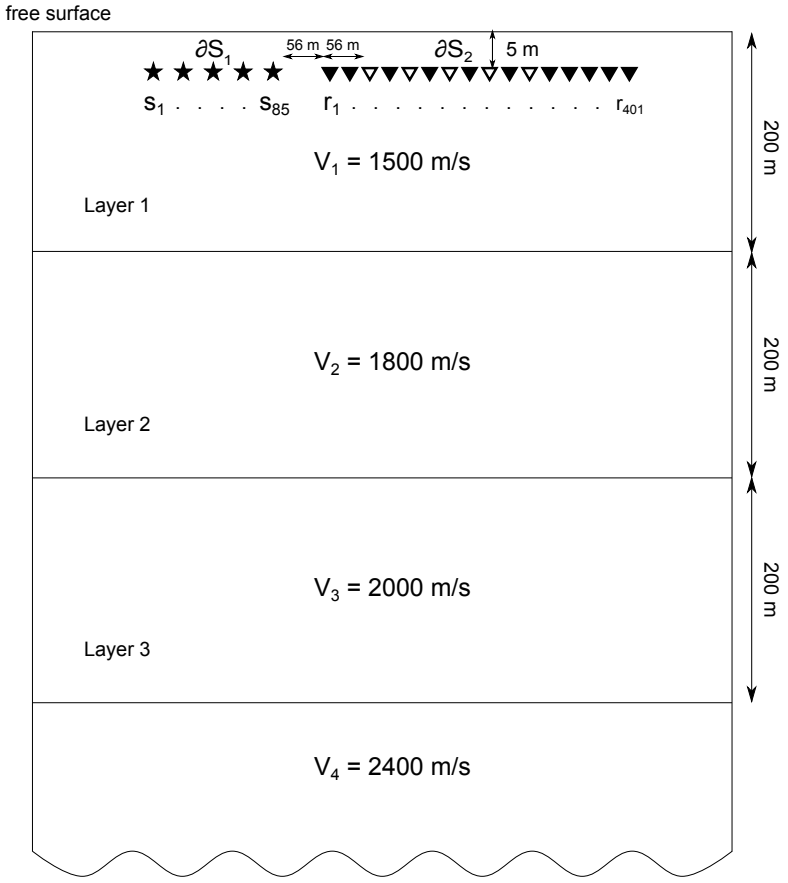

Figure 4.5: Three layer over a half-space acoustic velocity model and acquisition geometry. The source boundary ∂S_1 contains 85 sources (stars), separated at 8 m intervals, and illuminates 401 receivers (triangles) separated at 4 m intervals. Open triangles represent co-located receivers and sources corresponding to the ∂S_2 boundary. Sources and receivers are positioned at 5 m depth. The interval velocities V_k, are shown for the kth layer, where $k = 1,...,3$.

4.3 Illustrative example

Figure 4.5 shows an acoustic three-layered velocity model and acquisition geometry. The full wavefield from each source (stars) to all receivers (triangles) was modelled using a finite-difference scheme (Robertsson et al., 1994). For each source we subtract the modelled direct arrival from the full wavefield to obtain only the reflected wavefield at the receivers. Figure 4.6 shows two shot gathers from the model in Figure 4.5.

Figure 4.7(a) shows the Green's function estimates obtained using equation 4.1

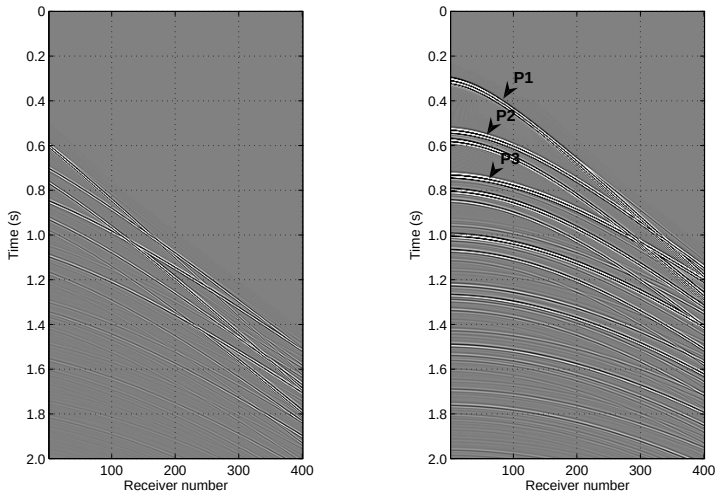

(a) (b)

Figure 4.6: Shot gathers from source 1 (a) and 85 (b) in Figure 4.5. P1–P3 denote primary reflections from the first, second and third interface, respectively.

by cross-correlating the reflected wavefield at receiver r_1 ($\mathbf{x}_A$) with itself and with the reflected wavefield along the receiver array, and summing the cross-correlations over the source boundary ∂S_1. Arrowheads (1–5) annotate the dominant non-physical reflections. Non-physical reflection (1) is created by the cross-correlation of the primary reflection from the second interface with the primary reflection from the first interface (e.g., Figure 4.2(a)). Non-physical reflection (2) is created by the cross-correlation of the primary reflection from the third interface with the primary reflection from the second interface (e.g., Figure 4.2(b)). The cross-correlation between the primary reflection from the third interface and primary reflection from the first interface as sketched in Figure 4.2(c) provides non-physical reflection (3). non-physical reflection (4) is less intuitive, but is provided by the cross-correlation of the primary reflection from the third interface with the first-order free-surface multiple. Figure 4.7(b) shows the Green's function estimates obtained using source-receiver interferometry in equation 4.4. For comparison, Figure 4.7(c) shows the gather as if an actual source was positioned at r_1.

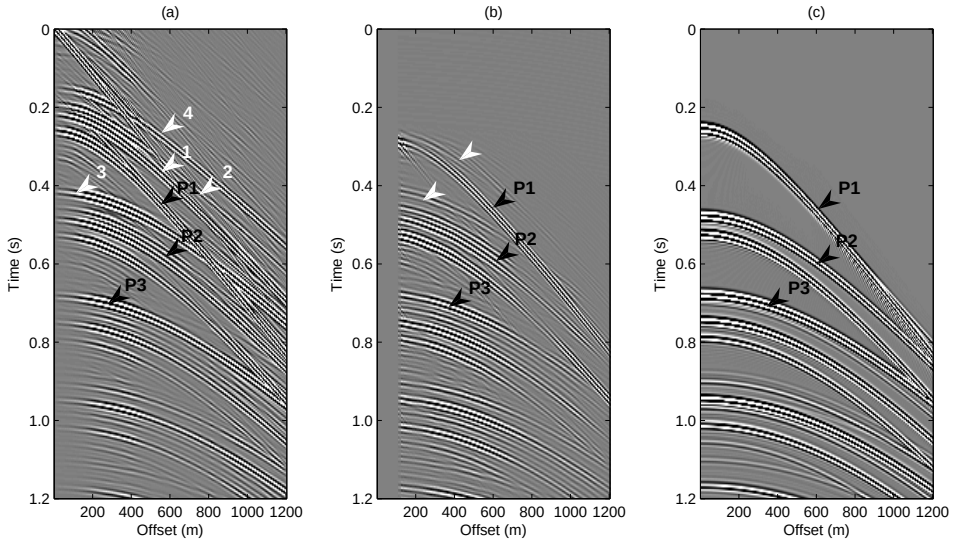

Figure 4.7: Green's function estimates obtained using (a) cross-correlational interferometry (equation 4.1) and (b) source-receiver interferometry (equation 4.4). (c) True Green's functions. White arrowheads (1-5) in (a) denote non-physical reflections (explained in text). P1–P3 denote primary reflections from the first, second and third interface, respectively.

By using source-receiver interferometry we obtain Green's functions that more closely resemble the true Green's functions (Figure 4.7(c)) and which show fewer non-physical reflections than the Green's function estimates made using cross-correlational interferometry (Figure 4.7(a)). As described above, it appears that non-physical reflections produced in cross-correlational interferometry provide physical reflections in source-receiver interferometry. This is important because the primary reflections and internal multiples cannot be retrieved by the cross-convolutions of physical reflections from an upper source boundary (e.g., equation 4.2). They can only be retrieved using appropriate convolutions of primary reflections and non-physical reflections in source-receiver interferometry (e.g., equation 4.4). For example, the primary reflection from the second interface (P2) in Figure 4.7(b) is provided by the convolution of non-physical reflection (1) in Figure 4.7(a) with the primary reflection from the first interface. Likewise, the primary reflection from the third interface (P3) is provided by the convolution of

non-physical reflection (2) in Figure 4.7(a) with the primary reflection from the second interface (e.g., Figure 4.4(a)). These dominant non-physical reflections have been used to create physical reflections by source-receiver interferometry. The convolution of pairs of physically reflected wavefields results in physical free-surface multiples in a laterally invariant medium. The convolutions of non-physical reflections with multiples as shown in Figure 4.4(b) enhances these free-surface multiple estimates in source-receiver interferometry. However, it should be remembered there still exist convolutions that will provide non-physical reflections after source-receiver interferometry (e.g., see arrivals at the white arrowheads in Figure 4.7(b)). Despite this, their amplitudes are much weaker than the corresponding non-physical reflections from cross-correlational interferometry.

Identifying the non-physical reflections from physical reflections is an important issue. Draganov et al. (2010) show that unlike their physical counterparts, non-physical reflections are identifiable because they change polarity after application of a damping compensation factor to the Green's function estimates. Curtis and Halliday (2010a) show that in a scattering medium the non-physical arrivals can be identified by using either wavefield separation or by reversing the order of the cross-correlation (physical arrivals obey reciprocity, non-physical arrivals do not).

We can also use source-receiver interferometry as a tool to identify the dominant non-physical reflections produced in cross-correlational interferometry. We can discriminate the non-physical reflections easily by transforming the gathers into the time-velocity domain, or in other words by generating their velocity spectra. The velocity spectrum displays the signal coherency along hyperbolic traveltimes t according to the equation

$$t = t_0 + \frac{x^2}{V^2}, \tag{4.5}$$

where t_0 is the two-way zero-offset traveltime, x is the offset between the virtual source and receiver, and V is the velocity of the subsurface (Taner and Koehler, 1969). We adopt semblance as the coherency measure (Neidell and Taner, 1971)

which is defined as

$$S_c = \frac{E_{out}}{M \cdot E_{in}} \qquad 0 \leq S_c \leq 1, \tag{4.6}$$

where

$$E_{out} = \sum_{t=t(i)-\Delta t/2}^{t=t(i)+\Delta t/2} \left\{ \sum_{j=1}^{M} f_{j,t} \right\}^2 , \tag{4.7}$$

and

$$E_{in} = \sum_{t=t(i)-\Delta t/2}^{t=t(i)+\Delta t/2} \sum_{j=1}^{M} f_{j,t}^2 , \tag{4.8}$$

where M is equal to the number of traces, $t(i)$ is the traveltime (equation 4.5), $f_{j,t}$ is the amplitude value on the jth trace at time t and Δt is a time window equal to 8 ms in the following example.

Figure 4.8(a) shows the velocity spectrum obtained from the Green's functions in Figure 4.7(a) while Figure 4.8(b) shows that obtained from the Green's functions in Figure 4.7(b). Figure 4.8(c) shows the spectrum obtained from the true Green's functions in Figure 4.7(c). Peaks corresponding to non-physical reflections 1, 2, 3 and 4 in Figure 4.8(a) are suppressed in Figure 4.8(b). The peak to the right of P1 in Figure 4.8(b) represents the non-physical reflection prior to the corresponding primary in Figure 4.7(b). Nevertheless, the velocity spectrum obtained from the source-receiver interferometric Green's functions shows good resemblance with the true velocity spectrum. Therefore, the velocity spectrum from source-receiver interferometry can be used in comparison with the velocity spectrum from cross-correlational interferometry to help identify the dominant non-physical reflections, in this case non-physical reflections 1, 2, 3 and 4.

Furthermore, the non-physical reflections in cross-correlational interferometry can also be used to characterize the interval velocities of the model. Consider again the non-physical reflection created by the cross-correlation of the primary reflections in Figure 4.2(a). If this specific cross-correlation were to be repeated using a linear array of sources like that shown in Figure 4.5 to obtain the Green's

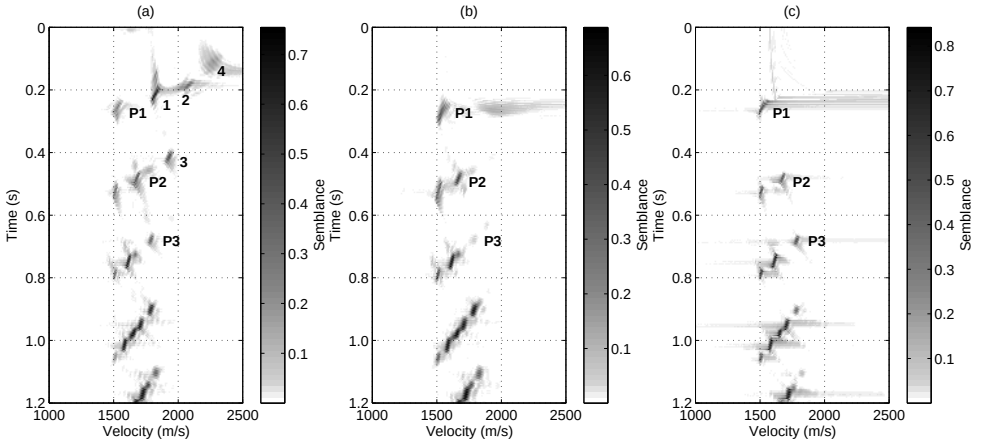

Figure 4.8: (a), (b) and (c) shows the velocity spectrum obtained from the Green's functions in Figures 4.7(a), 4.7(b) and 4.7(c), respectively. Annotated peaks correspond to the arrivals in Figure 4.7.

functions along a receiver array, we would expect the non-physical reflection to moveout with the interval velocity V_2 and have a zero-offset traveltime $t_{02} = 2Z_2/V_2$, where Z_2 is the thickness of the second layer. Similarly, the cross-correlation between the primary reflection from the third interface with the primary reflection from the second interface provides the traveltime of a non-physical reflection with moveout of the interval velocity V_3 and has a zero-offset traveltime $t_{03} = 2Z_3/V_3$, corresponding to a reflection propagating through the third layer only (Figure 4.2(b)). In general, the interval velocity V_k and two-way traveltime t_{0k} of the kth layer can be extracted by cross-correlating the primary reflections from the top and bottom of the kth layer along a receiver array. These non-physical reflections will be identifiable because the traveltime propagating through a single layer has the smallest t_0 traveltime. We exploit this property to find the interval velocities and thicknesses from the Green's function estimates in Figure 4.7(a).

Figure 4.9 shows the velocity spectrum in Figure 4.8(a) between 0 – 0.35 s. As expected, the non-physical peaks which have the smallest traveltimes correspond to the non-physical reflections described above (e.g., Figures 4.2(a) and 4.2(b)).

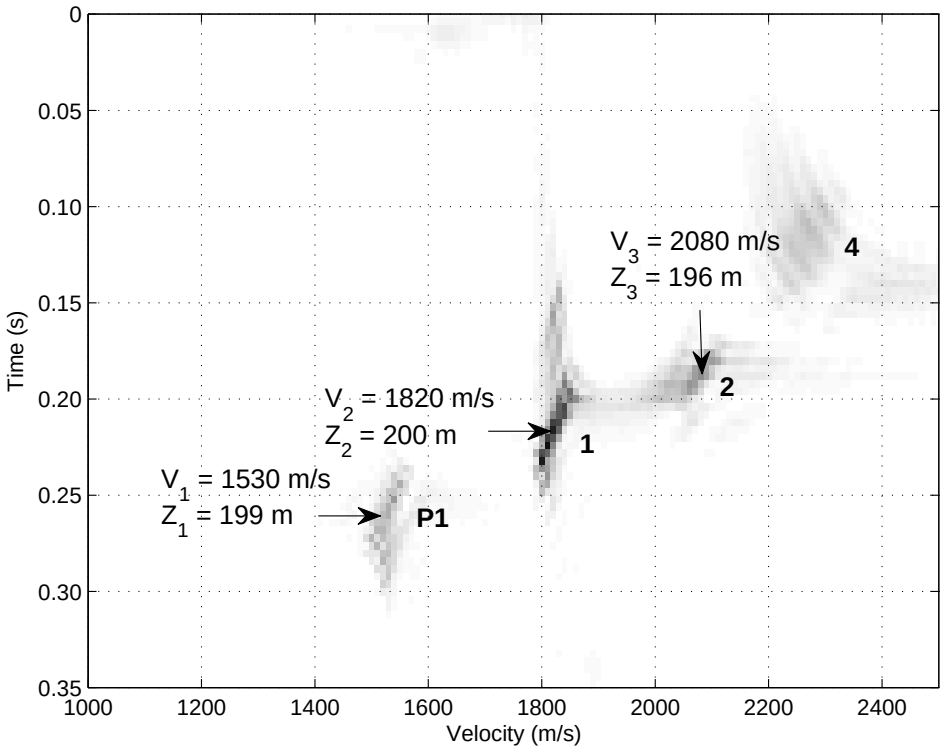

Figure 4.9: A close-up of the velocity spectrum in Figure 4.8(a) showing peaks between 0 s – 0.35 s. These peaks allow for a layer velocity and thickness interpretation as shown.

We are able to determine both interval velocity and layer thickness for each layer using the physical reflection P1, and non-physical reflections 1 and 2. The interval velocity and corresponding thickness parameters (computed using the relation $Z_k = (t_{0k}V_k)/2$) in Figure 4.9 show good agreement with the model values in Figure 4.5.

4.4 Discussion

There are several limitations to the velocity analysis procedure described above. Unlike the primary reflections, non-physical reflections do not propagate directly between the two receivers. The non-physical reflection samples a portion of the subsurface left (or right) of the receivers (e.g., Figure 4.2(a)). In a medium

with lateral velocity variations, the estimated seismic velocity will be inaccurate if the seismic velocity through which the non-physical reflection has travelled is different to the desired seismic velocity directly underneath the receivers. Additionally, while the above example is acoustic, in the an(elastic) real Earth, mode conversions between P- and S-waves are likely to complicate velocity interpretations.

We investigate the above limitations by comparing cross-correlational and source-receiver interferometry for the 2.5D elastic North Sea model in Figure 4.10(a). Source boundaries ∂S_1 and ∂S_2, each containing 65 sources, and 351 receivers are positioned as shown in Figure 4.10(b). Sources and receivers are vertically offset by 5 m. The vertical offset contravenes the requirement in source-receiver interferometry that sources and receivers are co-located on the boundary ∂S_2 (Figure 4.3(b)). The dataset was provided by an industry partner and hence, we have no control over the source and receiver depth. In this instance the depth difference is small and we do not correct for this discrepancy. Figure 4.11 displays two shot gathers from the model in Figure 4.10.

Figure 4.12(a) shows the Green's function estimates obtained using cross-correlational interferometry (equation 4.1) with the virtual source positioned at r_1, Figure 4.12(b) shows the Green's function estimates obtained using source-receiver interferometry (equation 4.4) and Figure 4.12(c) shows the true Green's functions. We identify two non-physical reflections (annotated by white arrowheads in Figure 4.12(a)) obtained by cross-correlational interferometry which are suppressed by source-receiver interferometry. Furthermore, source-receiver interferometry does well at constructing the later arrival times. For example, the source-receiver interferometric Green's functions inside the ellipse at approximately 1.5 s show better resemblance to the true Green's functions than the corresponding cross-correlational interferometric Green's functions.

Figure 4.13 show the corresponding velocity spectra for the Green's functions

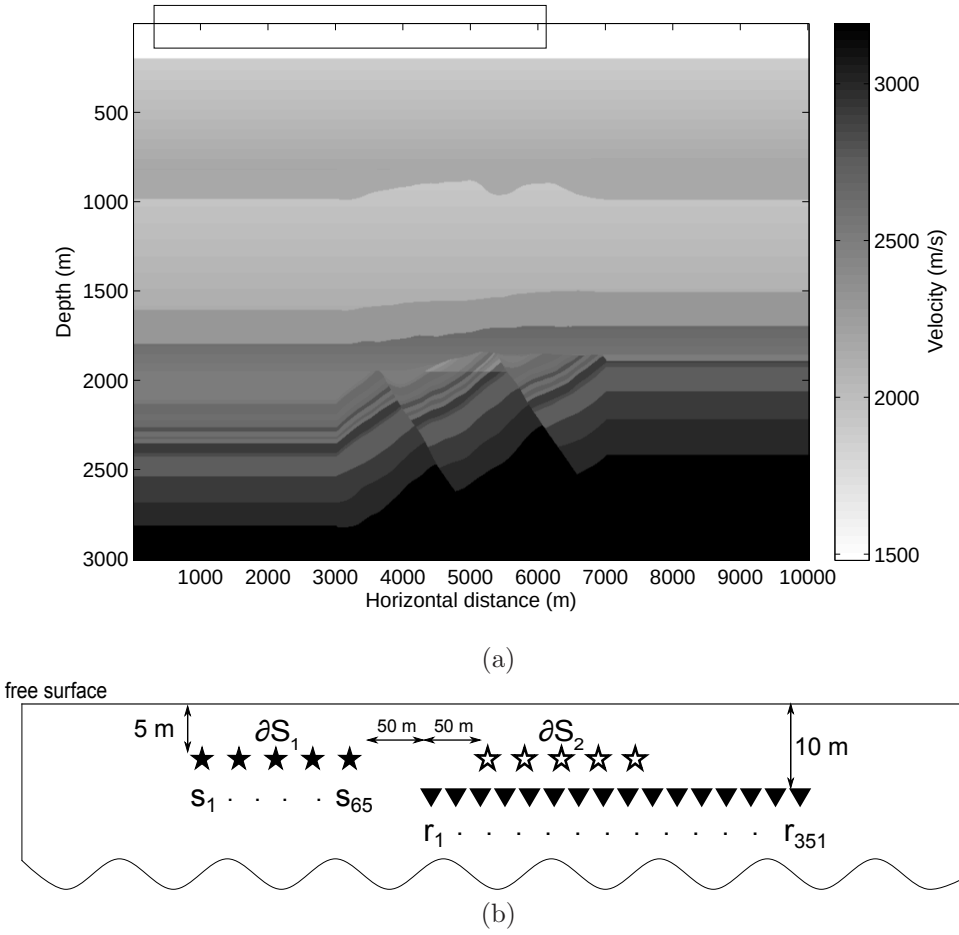

Figure 4.10: (a) 2.5D elastic North Sea model. (b) Acquisition geometry located within the confines of box in (a). Source boundaries ∂S_1 and ∂S_2 contain 65 sources separated at 25 m intervals. The 351 receives are separated at 12.5 m intervals.

described above. We now use a time-window of length 12 ms around the traveltimes computed using equation 4.5. Peaks enclosed by the ellipses at approximately 0.5 s and 0.75 s in Figure 4.13(a) correspond to the two annotated non-physical reflections in Figure 4.12(a). No equivalent peaks exist inside the ellipses after source-receiver interferometry in Figure 4.12(b). We identify a further non-physical reflection at approximately 1.5 s in Figure 4.13(a) which is also suppressed after source-receiver interferometry. Overall, the source-receiver interferometric velocity spectrum shows a better resemblance to the true velocity spectrum. These results suggest that source-receiver interferometry is more

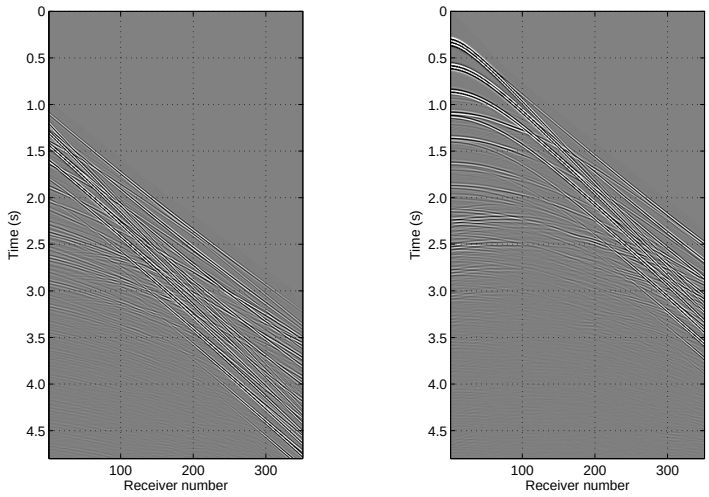

(a) (b)

Figure 4.11: Shot gathers from source 1 (a) and 85 (b) in Figure 4.10.

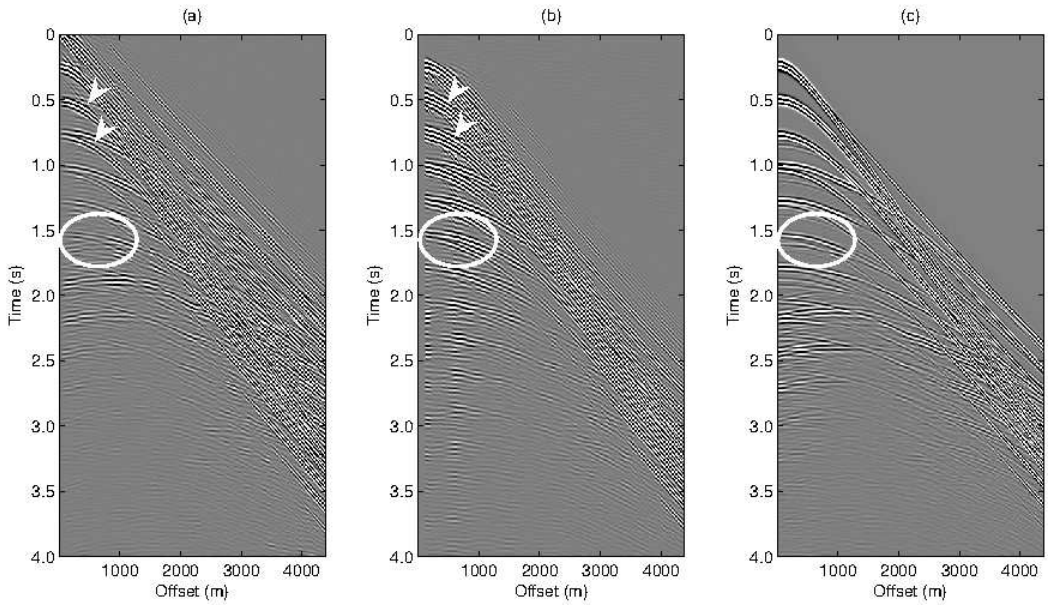

Figure 4.12: Green's function estimates obtained using (a) cross-correlational interferometry (equation 4.1) and (b) source-receiver interferometry (equation 4.4). (c) True Green's functions.

effective than cross-correlational interferometry for surface seismic data.

While the subsurface seismic velocity interpretation in Figure 4.9 is straightforward for the acoustic model in Figure 4.5, the method has limitations that

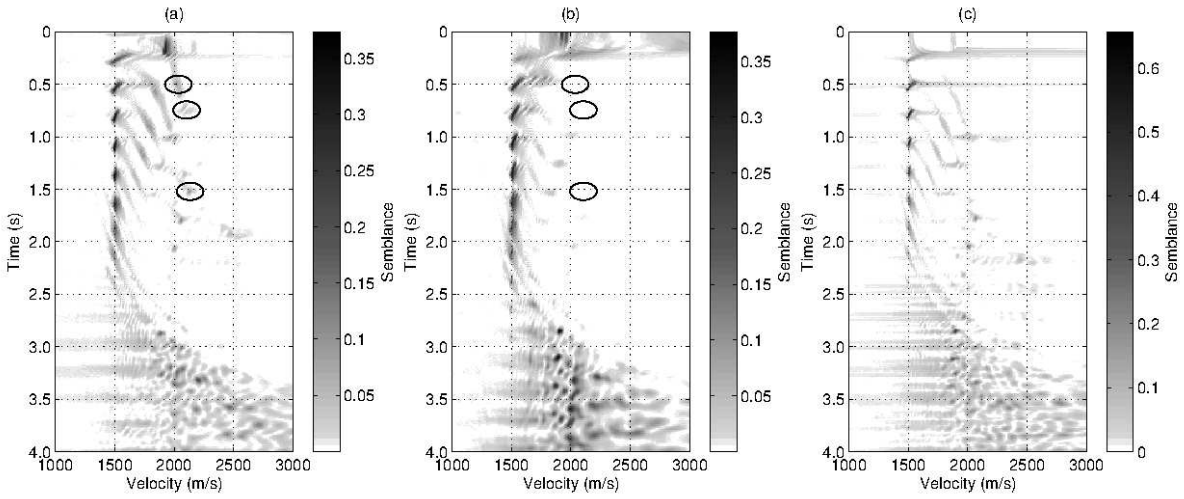

Figure 4.13: (a), (b) and (c) shows the velocity spectrum obtained from the Green's functions in Figures 4.12(a), 4.12(b) and 4.12(c), respectively.

are worth discussing when applied to a complex medium like that in Figure 4.10. First, non-physical reflections may be less identifiable in a complex medium. Draganov et al. (2010) showed that for a complex subsurface the non-physical reflections will smear into correlation noise and hence, not appear as identifiable events. Similarly, we only identify three prominent non-physical reflections in Figure 4.13 and a priori we cannot be confident that any of them provide the velocity and thickness of a specific layer. Assigning a velocity and thickness interpretation to these peaks is difficult because the non-physical reflections are likely to represent a correlation between high-orders of reflections.

In reality, assigning the peaks of non-physical reflections to specific layers may prove problematic even in the acoustic scenario. In Figure 4.9 we assumed that a peak with an increased velocity represented a non-physical reflection propagating through a deeper and therefore successive layer. If for example the velocity had decreased in one layer relative to the layer above, we would have interpreted the corresponding peak to have travelled through a shallower, but non-existent layer. Furthermore, identifying the appropriate non-physical reflections based on their t_0 traveltime will not always work. In Figure 4.9 we conveniently

ignored non-physical reflection (4) even though its t_0 traveltime was the smallest of the non-physical reflections. Similarly, it is plausible that a non-physical reflection which has travelled through two thinner layers (e.g., Figure 4.2(c)) has a smaller t_0 traveltime than a non-physical reflection which has travelled through a single but thicker layer. In this instance choosing the peaks which have the smallest t_0 traveltimes as above would lead to an inaccurate estimation of velocity. Thus, it would appear that any velocity estimate made using non-physical reflections would need to be confirmed or verified by conventional methods. Nevertheless, the information provided by the non-physical reflections clearly contains complementary information.

The source at $\mathbf{x}'$ in Figure 4.2(a) provides the dominant contribution to the retrieval of the non-physical reflection and is therefore referred to as a stationary-phase source (Snieder et al., 2006b). Hence, to recover a non-physical reflection that has the correct velocity and traveltime requires sources to be positioned at the *non-physical* stationary-phase locations. If the stationary-phase sources are missing, the non-physical reflections will have inaccurate traveltimes and velocities in much the same way that the physical reflections may be poorly constructed if the appropriate stationary-phase sources are not sampled.

Interestingly, Mallinson et al. (2011) show that a physical refraction can be created using a similar method to that outlined here. In the first step, the authors cross-correlate two refractions which leads to a non-physical arrival termed the virtual refraction (Mikesell et al., 2009). The virtual refraction passes through the origin of the virtual source gather and has a linear moveout that defines the velocity of the refracting medium. Like the non-physical reflection, the virtual refraction appears to be acquired with the virtual source and receiver positioned on the refracting interface. In the second step, Mallinson et al. (2011) convolve the virtual refraction with a physical refraction from the same interface. This step creates a physical refraction by in effect adding the upgoing and downgoing

component to the virtual refraction. Similarly, we have used a cross-correlation and then convolution to convert a non-physical reflection into a physical reflection.

Cross-correlational interferometry using equation 4.1 forms the basis for interferometric imaging (Schuster et al., 2004) and interpolation schemes (Wang et al., 2009; Hanafy et al., 2009; Wang et al., 2010). In these applications the Green's functions suffer from non-physical reflections caused by a limited source aperture. Source-receiver interferometry may suppress some of the non-physical reflections in the resultant images and virtual source gathers.

The procedure in equation 4.4 involves a double integral over three sets of Green's functions. In principle, the theory of source-receiver interferometry imposes no constraint on the number of cross-correlational/cross-convolutional boundaries and integrations. We now investigate what happens when we include a further cross-convolution on the right-hand side of equation 4.4. Mathematically, the above statement corresponds to a triple integral:

$$G(\mathbf{x}_B, \mathbf{x}_A) \approx$$
$$\frac{8}{\rho^3 c^3} \int_{\partial S_2} \int_{\partial S_2} \int_{\partial S_1} \Big[G(\mathbf{x}'', \mathbf{x}') G^*(\mathbf{x}_A, \mathbf{x}') \Big] G(\mathbf{x}_B, \mathbf{x}'') G(\mathbf{x}_B, \mathbf{x}'') d^2\mathbf{x}' d^2\mathbf{x}'' d^2\mathbf{x}'', \quad (4.9)$$

where we include a further cross-convolution of the Green's functions $G(\mathbf{x}_B, \mathbf{x}'')$ and integration along the source boundary ∂S_2 on the right-hand side. In the 1D example, the procedure can be thought of as convolving the source-receiver interferometric Green's function estimates in Figure 4.7(b) with the physical Green's functions and integrating again over the source boundary ∂S_2.

Figure 4.14(a) shows the Green's function estimates obtained using the original form of source-receiver interferometry (equation 4.4) and is identical to that shown previously in Figure 4.7(b). Figure 4.14(b) shows the Green's function estimates obtained using a new form of source-receiver interferometry (equation 4.9) and Figure 4.14(c) display the true Green's functions. It is clear

from Figure 4.14(b), that higher-order reflections are recovered by introducing a further convolution. The white arrowhead above the first-order free-surface multiple (M1) highlights a remaining non-physical reflection. This arrival is created by convolution of the upper non-physical reflection in Figure 4.14(a) with the physical primary reflection from the first interface. Despite this, the lower non-physical reflection in Figure 4.14(a) has been used again to a create physical reflection. The lower non-physical reflection in Figure 4.14(a) is equivalent to non-physical reflection (3) in Figure 4.2(c) and Figure 4.7(a). When this non-physical reflection is convolved with the primary reflection from the first interface in equation 4.9, we recover the primary reflection from the third interface (P3) in Figure 4.14(b). Thus, it would appear that by using a further convolution in equation 4.9, we can suppress some of the remaining non-physical reflections by using them to provide the true reflections at later times.

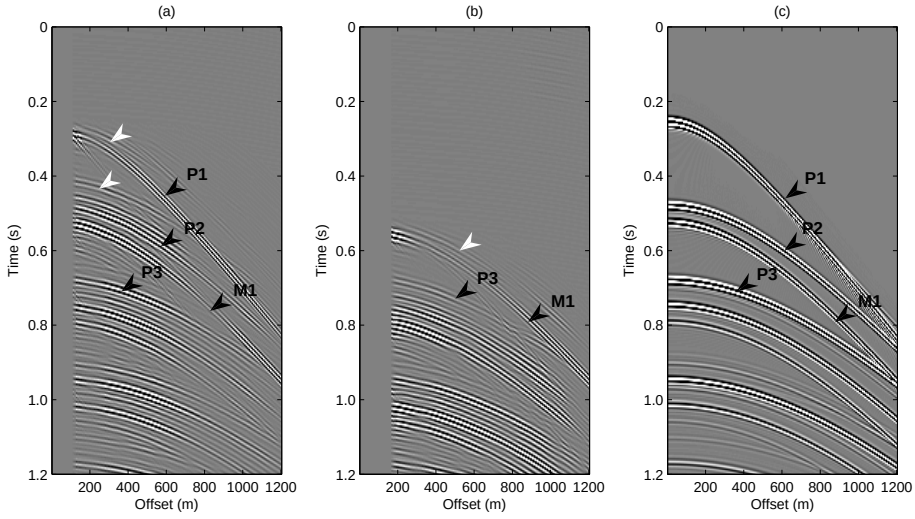

Figure 4.14: Green's function estimates obtained using (a) the original form of source-receiver interferometry (equation 4.4) and (b) a new form of source-receiver interferometry (equation 4.9). (c) True Green's functions. P1–P3 denote primary reflections from the first, second and third interface, respectively. M1 corresponds to the first-order free-surface multiple and white arrowheads correspond to non-physical reflections.

Despite the various practical limitations outlined above, the theory presented

shows why source-receiver interferometry might perform better than cross-correlational and cross-convolutional interferometry in some situations. It also shows that non-physical reflections contain physical information about the medium of propagation. Even though these methods have practical limitations in the laterally heterogeneous Earth, it should be remembered that conventional moveout-based velocity analysis methods also share several such limitations. Hence, it is likely that in future these methods may provide complementary information to conventional techniques, and that research into new methods to obtain physical information from non-physical arrivals will be profitable.

4.5 Conclusion

Seismic interferometry refers to the process whereby the Green's function is synthesized between two receivers using their recordings from a surrounding and enclosing boundary of sources. If only surface sources are available, non-physical reflections which represent the cross-correlation of reflections from different interfaces, are introduced into the Green's function estimates.

We show that non-physical reflections can be used to our advantage: so-called source-receiver interferometry converts many of the non-physical reflections obtained using cross-correlational interferometry back into physical reflections via cross-convolutional interferometry. The resultant Green's function estimates display fewer non-physical reflections than those obtained using cross-correlational interferometry and display better agreement with the true Green's functions propagating between the receivers. We can use source-receiver interferometry to identify the dominant non-physical reflections obtained from cross-correlational interferometry. This can be achieved by transforming the cross-correlational and source-receiver interferometric Green's functions into the time-velocity domain.

The non-physical reflections obtained initially by cross-correlational interfer-

ometry are particularly important in generating the primary reflections and internal multiples via convolution. This is because the primary reflections and internal multiples cannot be retrieved by the convolution of physical reflections from surface sources, but only by the appropriate convolution of a non-physical and physical reflection. We demonstrate cross-correlational and source-receiver interferometry on a 1D acoustic and 2.5D elastic model, respectively. In the 1D example we show that non-physical reflections associated with the cross-correlation of the primary reflection from the top and a bottom of a specific layer allow for the direct estimation of interval velocities and layer thicknesses. Identifying the appropriate non-physical reflection for velocity estimation is more difficult in the complex 2.5D example, but improvements in the Green's functions are still visible.

Chapter 5

Discussion

Throughout this thesis we have outlined novel applications which utilise the non-physical arrivals in the correlation gather (Chapter 2) and in the virtual source gather (Chapter 3) to estimate subsurface seismic velocities. We have also shown how to use the non-physical arrivals to create physical reflections via convolution (Chapter 4). We start by discussing how velocity analysis of the correlation gather could be extended to elastic and passive recordings. We then outline how source-receiver interferometry can be used to predict only the internal multiples and to approximate the dipolar boundary sources. Finally, we describe two ways in which the non-physical reflections could be emphasized or enhanced in interferometry for applications such as those outlined to date where their use is of most value.

5.1 Interferometric velocity analysis

5.1.1 Elastic example

In Chapter 2 we devised a procedure to determine the seismic velocity using interferometric wavefields in the correlation gather. In those examples we only considered acoustic wavefields and hence we did not account for shear waves

and/or mode conversions that would be present within the Earth's subsurface. We now discuss the implications when the method is applied to elastic recordings such as are obtained (approximately) from measurements available on land.

In elastic interferometry, Vasconcelos et al. (2008) adopt different source-receiver combinations in the correlation gather to isolate the surface waves. Their analysis has implications if we wish to determine the seismic velocity using elastic wavefields in the correlation gather. They show that sources outside of, or far from, the receiver pair contribute predominantly to the retrieval of surface waves (Figure 5.1(a)) and that sources positioned directly above or close to one of the receivers contribute predominantly to the retrieval of body waves (Figure 5.1(b)). Vasconcelos et al. (2008) mute the wavefields in the correlation gather corresponding to sources positioned as in Figure 5.1(b) and hence, after integration over the sources, the Green's function estimates contain surface waves. Therefore, we would expect the sources in Figure 5.1(b) to be useful for determining the P-wave and S-wave velocities, respectively.

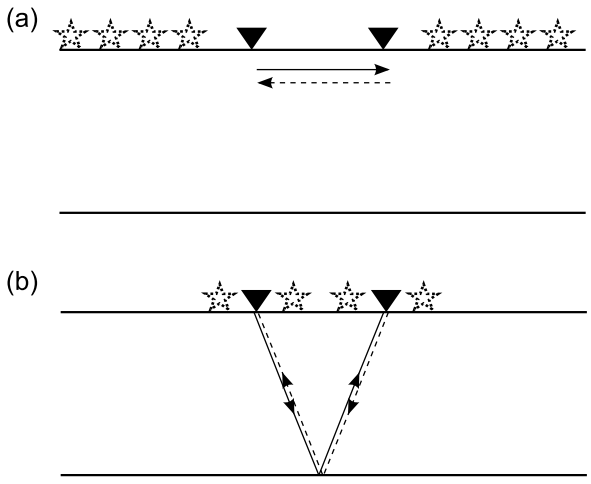

Figure 5.1: In a land setting sources far from of the receiver pair (a) contribute predominantly to surface waves whilst sources close to the receiver pair (b) contribute predominantly to body waves.

Consider the elastic model and acquisition configuration in Figure 5.2 (note that

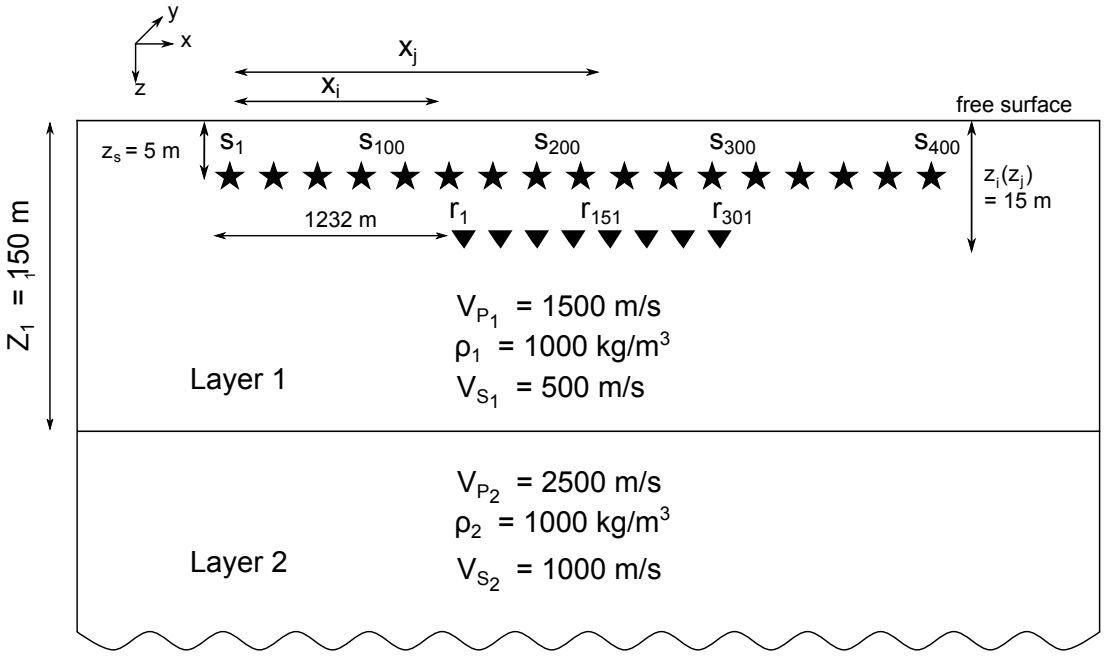

Figure 5.2: Elastic model consisting of a layer over a half-space, both homogeneous. Layer 1 is bounded on top by a free surface and below by a planar interface at 150 m depth. The P-wave velocities (V_{P_1} and V_{P_2}), S-wave velocities (V_{S_1} and V_{S_2}) and densities (ρ_1 and ρ_2) are shown.

the model has the same acquisition geometry as that described in Chapter 2 but we now introduce a shear-wave component and receivers measure the vertical component of the wavefield). This situation resembles a land setting where the upper layer represents solid material, and receivers are located in individual shallow wells. It should be noted that there is no requirement for the receivers to be positioned at depth. Figure 5.3(a) shows the correlation gather for receivers r_1 and r_{151}, Figure 5.3(b) displays the Green's function estimate found by summing over sources in the correlation gather, and Figure 5.3(c) shows the true Green's function. The Green's function estimate shows reasonable agreement with the true Green's function because we use a large upper boundary of sources which spans many of the stationary-phase source locations.

To obtain an estimate of the seismic velocity and layer thickness, we measure the signal coherency along traveltimes in the correlation gather (equation 2.4, Chapter 2). For a more detailed description of the procedure see section 2.2 in

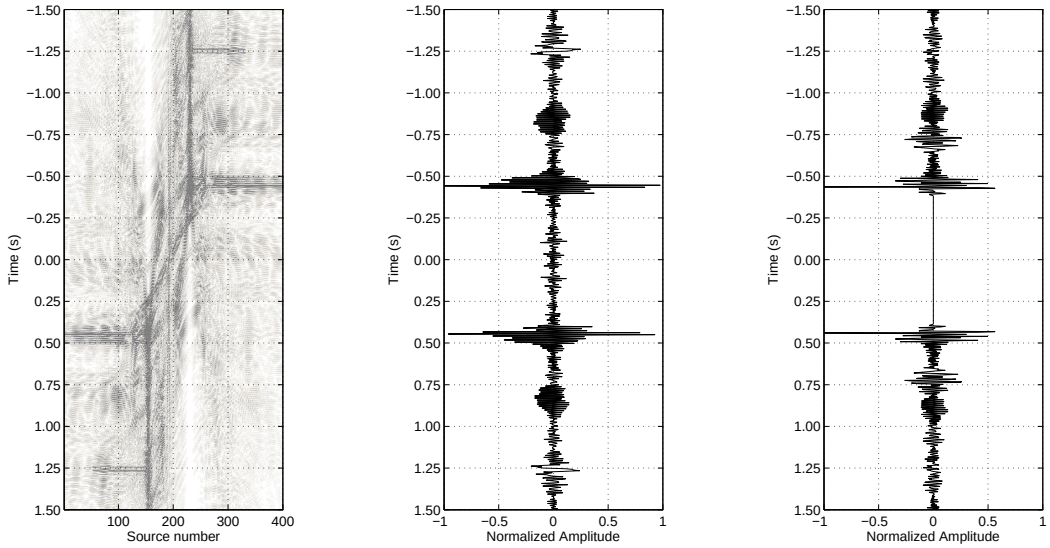

(a) (b) (c)

Figure 5.3: Interferometric Green's function estimates and true Green's function for the single layer over a half-space model in Figure 5.2. (a) Correlation gather for receivers 1 and 151 showing arrivals between -1.5 s and 1.5 s. (b) Green's function estimate after summation over source position in (a). (c) True Green's function plus its time-reversed component.

Chapter 2.

Figure 5.4(a) shows the P-wave velocity – layer-thickness spectrum computed using energy up to the third-order multiples and for all 400 sources. Figure 5.4(b) shows the corresponding spectrum but using only sources 130–160 (i.e., sources in similar positions to those sketched in Figure 5.1(b)). Although the spectrum in Figure 5.4(a) displays less 'noise', we achieve a broad diagonal peak, with the most coherent values positioned at lower thicknesses. When we consider sources 130–160 however, the semblance in Figure 5.4(b) may be 'noisy' but we achieve a well-defined peak at approximately $V_{P_1} = 1600$ m/s and $Z_1 = 160$ m, close to the true parameters of velocity and layer thickness.

To compute the S-wave velocity we fix the layer thickness at 160 m (as estimated from Figure 5.4(b)) and measure the signal coherency along traveltime curves that depend upon the shear-wave velocity only. Figure 5.5 shows the S-wave velocity

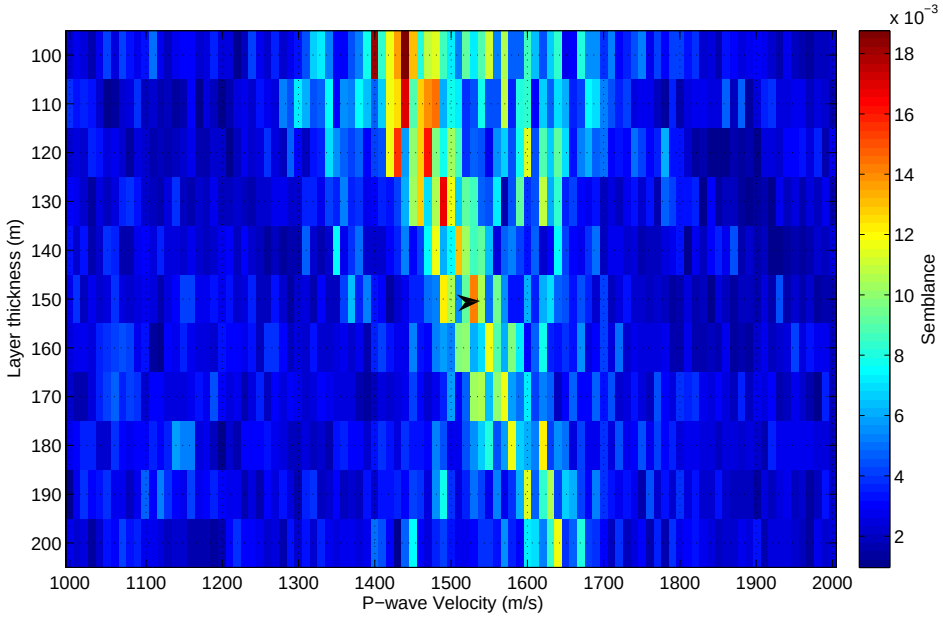

(a)

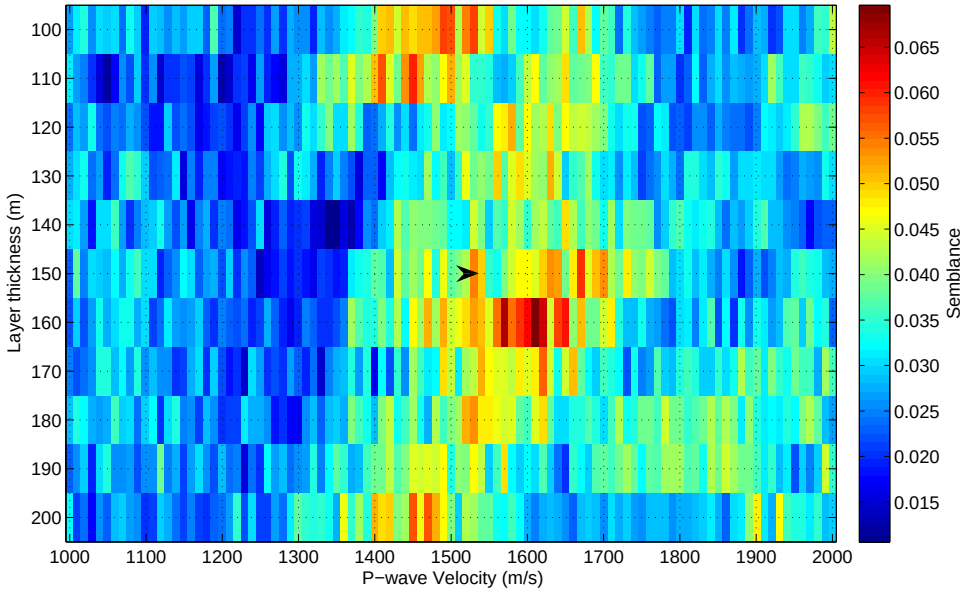

(b)

Figure 5.4: Spectra computed from the correlation gather in Figure 5.3(a). (a) P-wave semblance computed using all 400 sources and energy up to the third-order multiples. The arrowhead indicates the true values of velocity and layer thickness. (b) As for (a) but computed using only sources 130–160.

spectrum computed using energy up to the third-order multiples and for sources 130–160. The maximum semblance is obtained at a velocity of 480 m/s. This

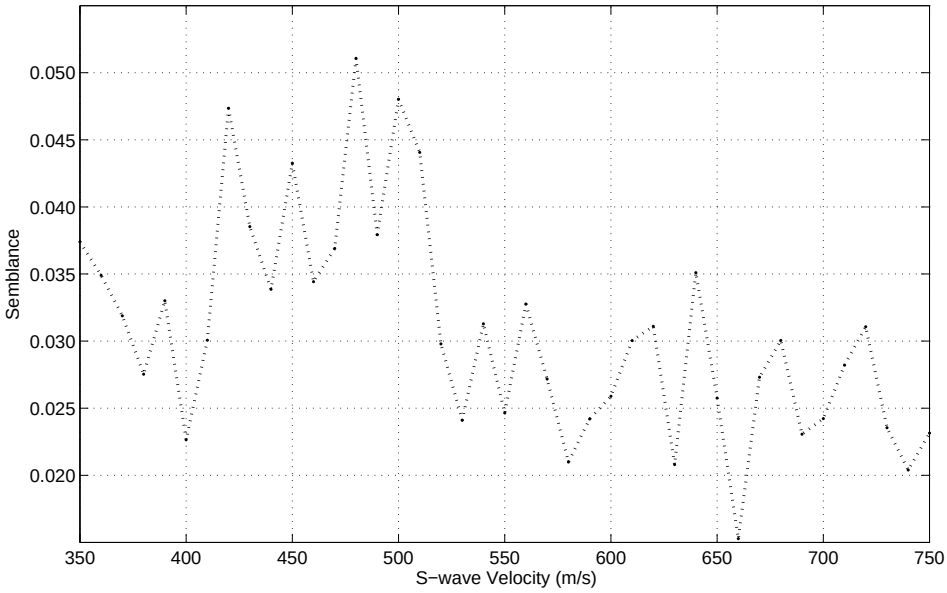

Figure 5.5: S-wave velocity semblance computed using sources 130–160 and energy up to the third-order multiples.

value is near to the actual S-wave velocity of 500m/s.

The quality of the P-wave results in Figure 5.4(b) and the S-wave results in Figure 5.5 are not as good as the semblance results in Chapter 2. For example, the peak value at 480 m/s in Figure 5.5 is only marginally higher than the peak value at 420 m/s. It may be that the interfering body and surface waves in the correlation gather degrade the resolution of the semblance results. Or perhaps we use too few sources in the semblance computation to achieve a good estimate of the subsurface velocity. Clearly, further developments are required to apply interferometric velocity analysis to elastic data.

5.1.2 Passive interferometry

Although we outline interferometric velocity analysis with respect to controlled-source interferometry, it is interesting to speculate whether the method could be applied to passive seismic interferometry. In passive interferometry, or in explorations settings where sources are fired at near simultaneous time (referred

to as blended data by Berkhout (2008)), the correlation gathers are not available because the Green's function is implicitly summed over unknown source positions. Wapenaar (2011) discusses the relation between the simultaneous-source method and seismic interferometry.

Seismic interferometry has a strong link to the receiver function method (Galetti and Curtis, 2012). We have discovered that the method of interferometric velocity analysis shares much similarity with the teleseismic receiver function method outlined by Zhu and Kanamori (2000). They show that the traveltime difference between a direct P-wave receiver function and a mode converted Ps[1] receiver function can be used to identify the V_P/V_S ratio and depth Z to the Moho underneath a single seismometer. We instead use the traveltime differences between different orders of reflections. Their resultant semblance plots are very similar to those shown in Chapter 2. Whereas we incorporate multiple reflections to improve our final result, Zhu and Kanamori (2000) reduce the ambiguity of the final parameters by including the later multiple converted phases. Specifically, they consider two further differential traveltimes, the first being the difference between a direct P-wave and the arrival PpPs and the second between a direct P-wave and the arrival PpSs + PsPs.

As Zhu and Kanamori (2000) compute V_P/V_S and Z using a single receiver function trace, it is conceivable to imagine our method extended to passive interferometry (or interferometry performed using simultaneous sources) where a Green's function is obtained between two receivers. We suspect that if such a method was to be formulated, we would require a complete boundary of sources, or at least to have sources positioned at the stationary-phase locations because we would require a Green's function estimate that bears a close resemblance to the true impulse response.

However, we should bear in mind that interferometric velocity analysis in

[1]In receiver function notation, except for the first arrival, lowercase letters denote upgoing waves and uppercase letters denote downgoing waves.

this instance would only be advantageous if we had two receivers or limited receiver coverage. If Green's functions could be estimated along a receiver array, conventional velocity analysis techniques or those discussed in this thesis could be employed instead. Nevertheless, there is a clear link between interferometry and receiver function analysis meaning such methods could be employed.

5.2 Source-receiver interferometry

5.2.1 Obtaining the internal multiples only

In Chapter 4, we have already shown that internal multiples can be predicted using a variant of source-receiver interferometry (Curtis and Halliday (2010b)). The internal multiples were retrieved as part of a wider remit to obtain Green's function estimates with fewer non-physical arrivals. In fact, it has long been known that internal multiples can be retrieved using a combination of cross-correlation and cross-convolution (Jakubowicz, 1998). In this section, we reformulate the method of Jakubowicz (1998) and show how to obtain internal multiples only using source-receiver interferometry.

Internal multiples have no downward reflections at the free-surface but one or more downward reflections within the subsurface. The order of an internal multiple is defined by the total number of subsurface downward reflections. For example, a first-order internal multiple will experience two upward reflections and one downward reflection. As an internal multiple will have reflected within the earth at least three times, they have a small amplitude which makes them difficult to discriminate from primaries and surface-related multiples in reflection records. Nevertheless, if not separated or attenuated prior to velocity analysis or imaging, internal multiples can be misinterpreted as primaries or free-surface multiples and may create noise in resulting images.

Berkhout and Verschuur (1997) outlined one scheme to predict internal

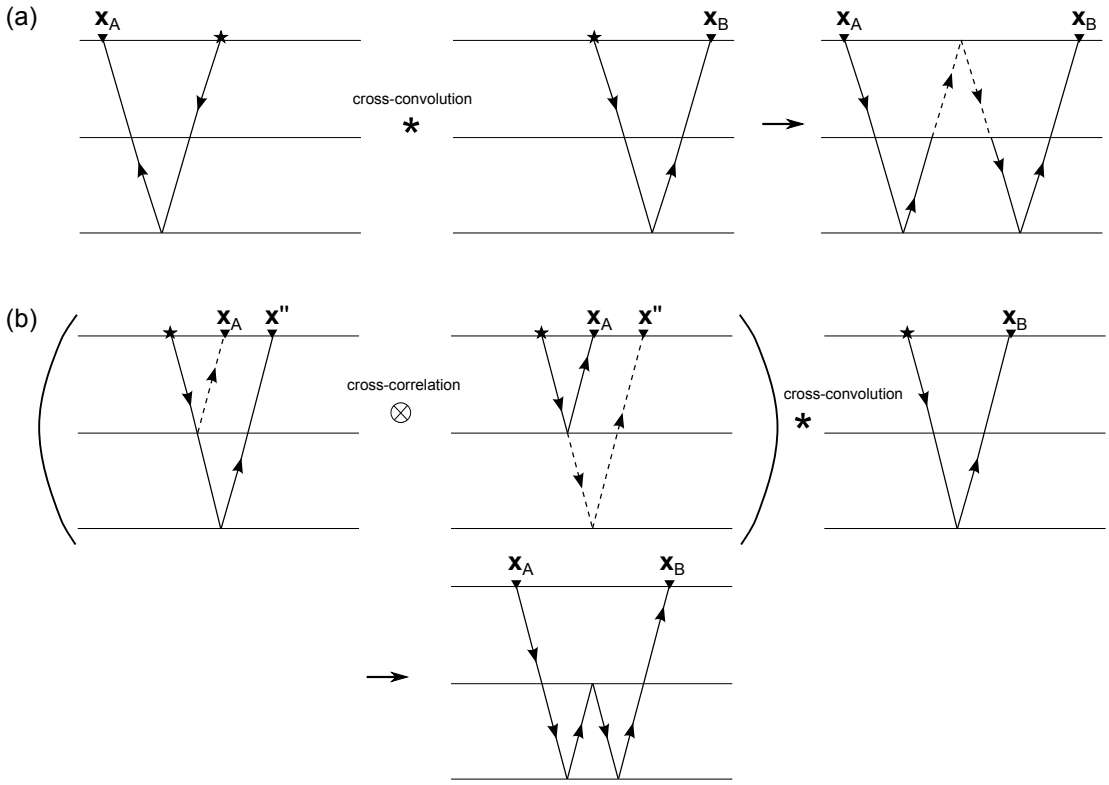

Figure 5.6: (a) The cross-convolution of two primary reflections provides a first-order free-surface multiple. To predict internal multiples by cross-convolution, we need to remove the component of the primary reflections from the first interface (equivalent to the dashed raypath on the right-hand side). (b) The cross-correlation of the primary reflection from the second interface with the primary reflection from the first interface results in a wavefield which appears to have reflected from the second interface with the virtual source and receiver positioned at the first interface. Its subsequent cross-convolution with the primary reflection (*right*) creates an internal multiple (*bottom*).

multiples by convolving two model-derived Green's functions (i.e., Green's functions derived using an appropriate velocity model) redatumed to the multiple-generating interface. However, Jakubowicz (1998) showed that the combination of three primary arrivals will correctly predict an internal multiple without the need for a velocity model (Figure 5.6(b)). Ikelle (2006) presents a similar approach based on virtual seismic events. We show that a similar approach to that of Jakubowicz (1998) and Ikelle (2006) is another particular case of source-receiver interferometry. In a related method, Poliannikov (2011) adapts source-receiver interferometry to find the underside reflections between receivers positioned in a

horizontal well within the subsurface.

Figure 2.11 from Chapter 2 shows the acoustic model and acquisition geometry, but we now fix both sources and receivers at 5 m depth and assume that we have access to wavefield recordings that only contain primaries and internal multiples: we therefore now assume that all surface-related multiples were eliminated at a prior point in the work flow. As we no longer have wavefields which reflect back into the medium via the free surface (i.e., scatterers outside of the source boundary), it is appropriate to consider cross-correlational and cross-convolutional interferometry with respect to only monopolar sources.

Figure 5.7(a) shows the full reflection Green's functions at 5 m depth obtained using the monopolar cross-correlational interferometric equation 2.1 (Chapter 2). The wavefield is multiplied by a t^3 gain to increase the amplitude of the internal multiples. Figure 5.7(c) displays the same gather but includes a traveltime interpretation of the selected internal multiples. Figure 5.8 shows a sketch of the selected internal multiples (1–5).

To obtain the internal multiples, we perform a similar operation to that demonstrated in Figure 5.6(b) using source-receiver interferometry. We first consider the cross-convolution of two reflected wavefields using the equation:

$$G_{r-p}(\mathbf{x}_B, \mathbf{x}_A) \approx \int_{\partial S_2} G_{p_2,p_3+im}(\mathbf{x}_B, \mathbf{x}'')G_{p_2,p_3}(\mathbf{x}_A, \mathbf{x}'')d^2\mathbf{x}'', \tag{5.1}$$

where G_{p_2,p_3+im} comprises the second-layer and third-layer primary reflections plus internal multiples, and G_{p_2,p_3} comprises only the second-layer and third-layer primary reflections, respectively. We have already shown that the convolution of two reflected wavefields provides a free-surface multiple between two receiver locations (Figure 5.6(a)). However this formulation in equation 5.1 is inappropriate to predict only the internal multiples because cross-convolution in equation 5.1 creates new reflections whose raypath contains a portion which

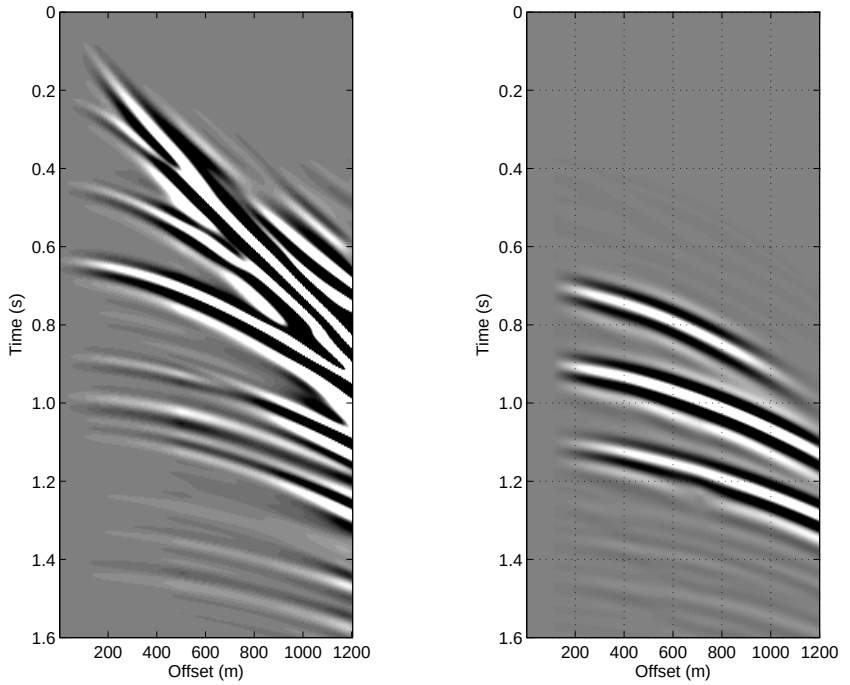

(a) (b)

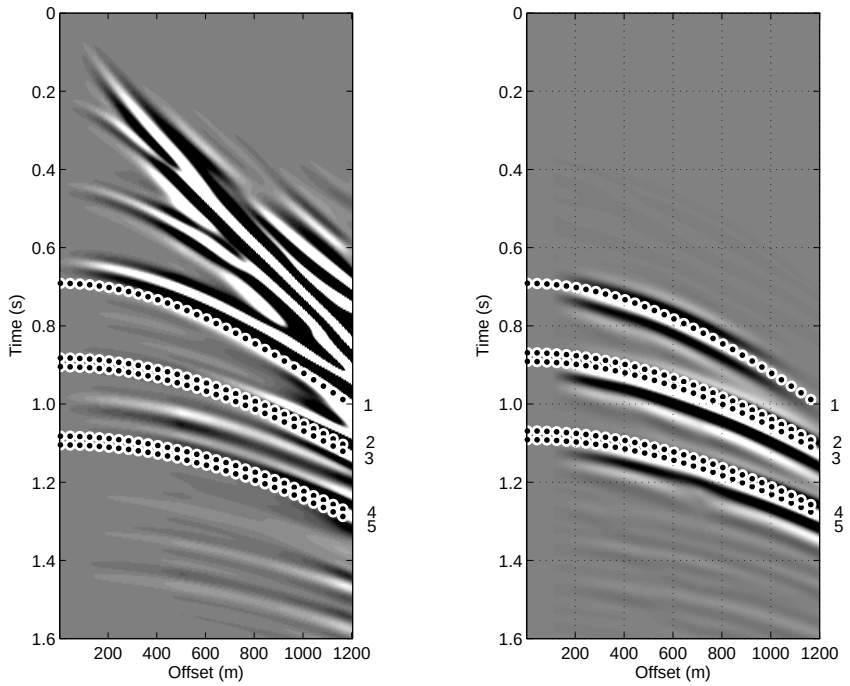

(c) (d)

Figure 5.7: Virtual source gather obtained using (a) the simplified monopolar cross-correlational equation 2.1 and (b) the source-receiver interferometric equation 5.3 for the model in Figure 2.11. A traveltime interpretation of (a) and (b) is provided in (c) and (d), respectively. The dotted hyperbolae (1–5) represent the internal multiples defined in Figure 5.8

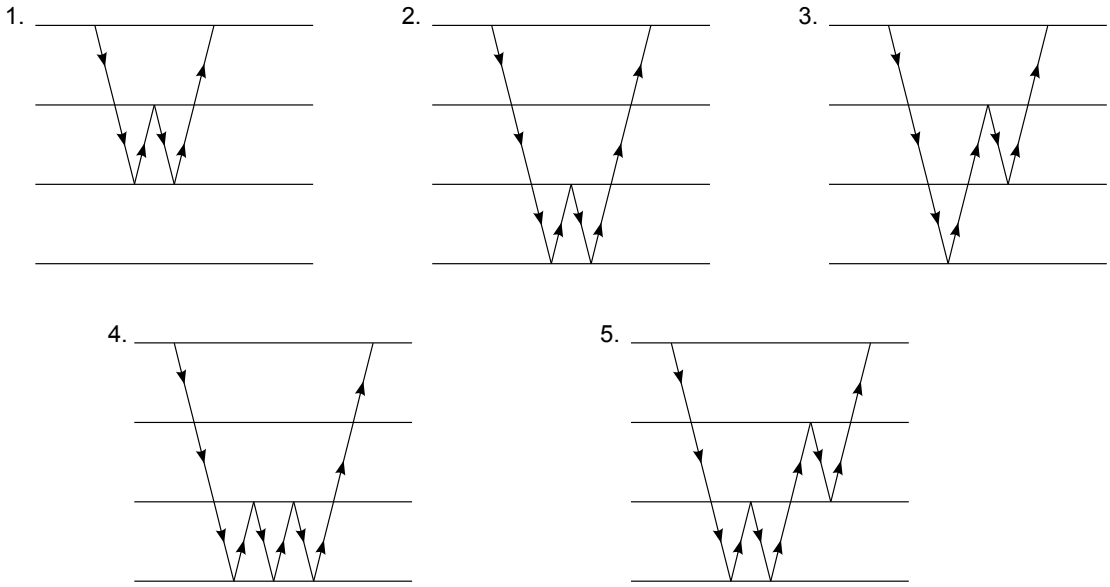

Figure 5.8: The raypaths of internal multiples in Figure 5.7(c) and 5.7(d). For simplicity, we assume straight raypaths in this sketch.

is equivalent to the primary reflection reflected from the first interface (dashed line in Figure 5.6(a)). Removal of this primary reflection can be achieved by cross-correlating the first primary reflection $G_{p_1}(\mathbf{x}_A, \mathbf{x}')$ with the second and third primary reflections $G_{p_2,p_3}(\mathbf{x}'', \mathbf{x})$ according to

$$G_{np}(\mathbf{x}'', \mathbf{x}_A) \approx \int_{\partial S_1} G_{p_2,p_3}(\mathbf{x}'', \mathbf{x}') G^*_{p_1}(\mathbf{x}_A, \mathbf{x}') d^2\mathbf{x}'. \tag{5.2}$$

where the subscript *np* refers to non-physical on the left-hand side. Equation 5.2 will result in two non-physical arrivals (or spurious multiples) where the traveltime of the first primary reflection has been subtracted from the second and third primary reflection, respectively. Hence, the resultant wavefield on the left-hand-side of equation 5.2, will appear to have been acquired with the receivers positioned at the first interface. The output of the cross-correlation in Figure 5.6(b) is shown in Figure 4.2(a) (Chapter 4).

Hence, by assuming source-receiver reciprocity and substituting $G_{np}(\mathbf{x}'', \mathbf{x}_A)$ in

equation 5.2 for $G_{p_2,p_3}(\mathbf{x}_A, \mathbf{x}'')$ in equation 5.1 we obtain the Green's functions

$$G_{r-p}(\mathbf{x}_B, \mathbf{x}_A) \approx \int_{\partial S_2} \int_{\partial S_1} [G_{p_2,p_3}(\mathbf{x}'', \mathbf{x}') G^*_{p_1}(\mathbf{x}_A, \mathbf{x}')] G_{p_2,p_3+im}(\mathbf{x}_B, \mathbf{x}'') d^2\mathbf{x}' d^2\mathbf{x}'', \tag{5.3}$$

which comprise only internal multiples. An example of this equation is demonstrated in Figure 5.6(b). As depicted in Figure 5.6(b), it is important that we only consider the second-layer primary reflections and the third-layer primary reflections plus internal multiples in equation 5.1, or in other words, only reflections whose upward reflection point is beneath the first-possible multiple generating interface, and for this reason the first-layer primary reflection is removed to obtain G_{p_2,p_3+im} and G_{p_2,p_3}. If the primary from the first interface is included, we would construct primaries and multiples.

Equation 5.3 is similar to that derived in source-receiver interferometry (Curtis and Halliday, 2010b), except the terms on the right-hand-side are modified appropriately. Note that here, the cross-convolutions are essentially virtual reflections (Poletto and Farina, 2010), a non-physical reflection as though there was a reflector (or scatterer) at the source position. However, the source is positioned so close to the free-surface that the resultant wavefields are kinematically almost equal to internal multiples to the extent that an adaptive filter might be used to remove them from seismic data (Dragoset, 1995). Figure 5.7(b) shows the virtual source gather obtained using source-receiver interferometry in equation 5.3 for the fixed receiver at $\mathbf{x}_A$ and every receiver ($\mathbf{x}_B$) at 5 m depth. Figure 5.7(d) shows the same gather with a selected traveltime interpretation.

A potentially impractical feature of internal multiple estimation as outlined here (and in the methods of Jakubowicz (1998) and Ikelle (2006)) is that in preparation we must isolate the primary reflections by applying a normal moveout correction using the appropriate velocity model, mute the unwanted primary reflections

and/or internal multiples, and then apply an inverse normal moveout correction to recover the desired reflections suitable for use in equation 5.3. We could of course use full wavefields in equation 5.3: we would still obtain Green's functions kinematically equal to the internal multiples but we would then require them to be separated from other arrivals – primary reflections, multiples and non-physical reflections.

5.2.2 Approximating the dipolar boundary sources

The full interferometric integral requires dipolar sources (equation 1.2, Chapter 1). As we have already mentioned in the Introduction, dipolar sources are rarely available in most acquisition settings. In theory dipolar sources can be predicted by constructing source-side derivatives using two source boundaries. However, it is more common to have a higher density of receivers than sources.

Source-receiver interferometry may offer a solution to predict the dipolar sources. Consider the acquisition geometry in Figure 5.9(a); notice here that we have a higher density of sources than receivers. This is the geometry required by cross-correlational source-receiver interferometry when the source in the centre for example at $\mathbf{x}_A$, has been replaced by a receiver.

If we construct the Green's function between every receiver on the boundary ∂S_2 and the receivers at $\mathbf{x}_A$ and $\mathbf{x}_B$ using conventional cross-correlational interferometry (equation 2.1, Chapter 2), we have created a new boundary of virtual sources along ∂S_2 (Figure 5.9(b)). This supplements the existing source boundary ∂S_1. Therefore in theory, we can use the actual Green's functions fired at $\mathbf{x}'$ and the interferometric Green's functions fired at $\mathbf{x}''$ to create a finite-difference approximation to the derivatives required by the complete theory of seismic interferometry (equation 1.2, Chapter 1). As a result, the Green's functions obtained using the complete interferometric formula 1.2 may be improved over those obtained using the simplified interferometric equation 2.1.

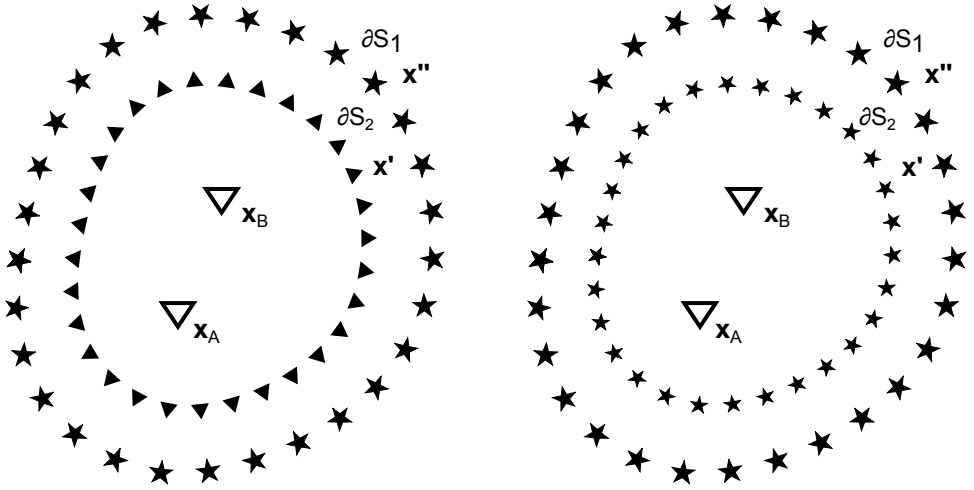

(a) (b)

Figure 5.9: (a) Acquisition set-up for cross-correlational source-receiver interferometry. In theory, if the boundary of receivers ∂S_2 are turned into virtual sources (b) the dipolar sources required by the complete theory of interferometry could be approximated using a finite-difference scheme.

5.3 Emphasizing the non-physical reflections

It is natural for geophysicists to seek the physical arrivals in Green's function estimates because these arrivals are most familiar to them. For this reason, many authors have sought to suppress the non-physical arrivals in favour of physical arrivals in the Green's function estimates (Bakulin and Calvert, 2006; Mehta et al., 2007; van der Neut and Bakulin, 2009; Curtis and Halliday, 2010a). However, we acknowledge that not all non-physical arrivals will provide benefits. Nevertheless, as we have shown the non-physical arrivals to be useful and complementary to their physical counterparts, its possible that we may wish their contributions to be enhanced. In this section, we investigate that objective and briefly describe two ways in which physical arrivals may be suppressed in favour of the non-physical arrivals.

5.3.1 Isolating non-physical arrivals using cross-correlational and deconvolutional interferometry

Isolating only the non-physical reflected wavefield is difficult in cross-correlational interferometry because term C_4 (equation 2.3, Chapter 2), the term which is predominantly responsible for the non-physical arrivals, contributes to physical reflections too. In theory, we could use the fact that cross-correlational and deconvolutional interferometry (Vasconcelos and Snieder, 2008a,b) construct equivalent physical arrivals, but different non-physical arrivals to solely isolate the non-physical arrivals.

Vasconcelos and Snieder (2008a,b) show that causal ($t > 0$) direct (D_1) and reflected (D_2) waves are produced by deconvolutional interferometry. These are equivalent to the arrivals corresponding to terms C_1 and C_2 in cross-correlational interferometry (equation 2.3, Chapter 2). These arrivals are considered physical and are produced in both cross-correlational and deconvolutional interferometry.

However, there are no arrivals in deconvolutional interferometry which correspond to the cross-correlations of reflections, C_4; the term which is predominantly responsible for the non-physical arrivals in cross-correlational seismic interferometry. Likewise, there are non-physical arrivals present in deconvolutional interferometry (termed free-point scattered waves by Vasconcelos and Snieder (2008a)) which have no equivalent in cross-correlational interferometry.

Therefore in theory, if we were to match the cross-correlational Green's functions with the deconvolutional Green's functions by least-squares, we would expect the physical arrivals to match up. If we were then to subtract the two Green's functions the physical arrivals would be suppressed but the non-physical arrivals from both cross-correlational and deconvolutional interferometry would remain.

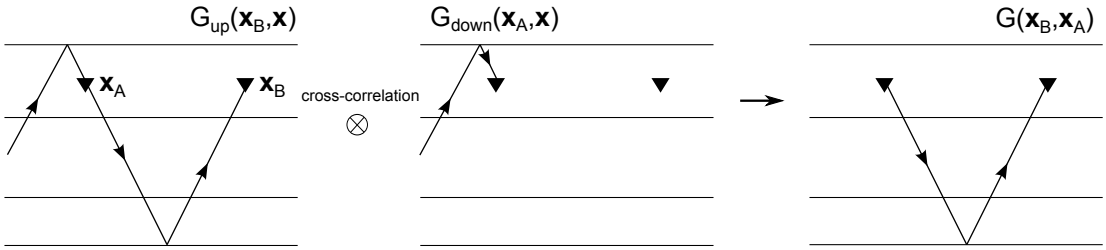

Figure 5.10: Cross-correlation of the downgoing wavefield at $\mathbf{x}_A$ with the upgoing wavefield at $\mathbf{x}_B$ will isolate the phase of the primary reflection between the receiver locations.

5.3.2 Wavefield separation

Mehta et al. (2007) show that an improved Green's function is obtained when the time-windowed downgoing wavefield (or direct arrival) at the virtual source is cross-correlated with the upgoing wavefield at the receivers (Figure 5.10). This form of interferometry means that non-physical reflections are suppressed to an extent. Conversely, if we wish to emphasize the non-physical reflections we can cross-correlate the upgoing wavefield at $\mathbf{x}_A$ with the upgoing wavefield at $\mathbf{x}_B$ (Figure 5.11).

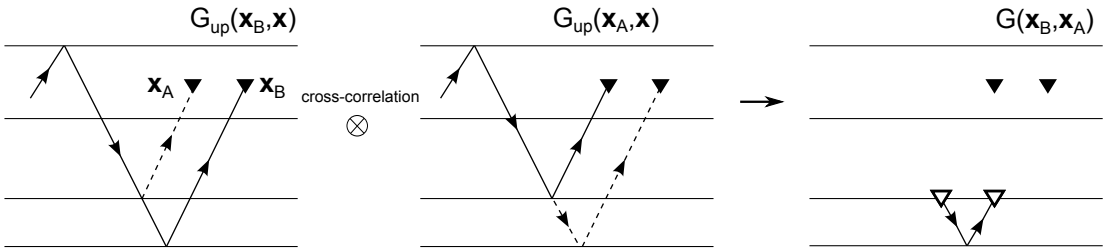

Figure 5.11: Cross-correlation of the upgoing wavefield at $\mathbf{x}_A$ with the upgoing wavefield at $\mathbf{x}_B$ will isolate the phase of the non-physical reflections.

5.4 Conclusion

We have shown how interferometric velocity analysis as outlined in Chapter 2 could be extended to elastic and passive data. We then describe the link between source-receiver interferometry and internal multiple prediction. We then discuss

how source-receiver interferometry may be used to compute the dipolar boundary sources. Finally, we return to the theme of non-physical energy and show how these arrivals may be emphasized using a least-squares and subtraction step, or by wavefield separation. These latter processing steps may benefit applications which use non-physical arrivals to characterize subsurface properties of the Earth.

Chapter 6

Conclusions

Seismic interferometry refers to the process whereby the Green's function is retrieved between two points using the cross-correlation, cross-convolution or deconvolution of wavefields. The theory was initially developed to retrieve Green's functions between two receivers, but has since been extended to extract Green's functions between two sources or more generally between a source and receiver. Several assumptions required by the theory of seismic interferometry are often breached because they do not conform to usual practices in conventional exploration seismology. As a result, non-physical arrivals are introduced in the Green's function estimates. In Chapter 1, we outline the theory of interferometry and explain in more detail why non-physical arrivals exist.

This thesis focuses on applications which use non-physical arrivals in the Green's function estimates between receivers in marine-type geometries to infer subsurface properties. These methods complement existing techniques that use physical arrivals. We also show that the non-physical arrivals do not have to be suppressed but can be used constructively to create physical reflections in source-receiver interferometry.

In Chapter 2, we estimate subsurface seismic velocities and layer thicknesses using the wavefield properties of the correlation gather. The velocity and

thickness parameters are extracted by measuring the signal coherency along traveltime curves in the correlation gather. When the method is applied to find the properties of the uppermost layer, the procedure implicitly incorporates the physical and non-physical energy in the Green's function estimates. When the method is applied to a multi-layered Earth, the root-mean-square velocities are estimated in a 'layer-stripping' approach by using traveltime curves which represent wavefields corresponding to non-physical reflections (spurious multiples) solely. Interval velocities are then estimated by using the root-mean-square velocities and thickness parameters in a Dix-type inversion. The estimated interval velocities show good agreement with the model values. The procedure implicitly uses free-surface and internal multiples to constrain velocity and layer thickness estimates; arrivals which are commonly handled incorrectly in many velocity analysis procedures. However, the layer-stripping approach has its limitations. For example, if an estimated velocity is inaccurate near the beginning of the process, the error will cause subsequent velocity and thickness estimates to suffer. We reduce these errors by incorporating multiples to constrain parameters. Nevertheless, the approach is only applicable to two receivers at a time. This offers an advantage over conventional velocity procedures because we are able to obtain a velocity estimate between every receiver pair in a receiver array. Furthermore, in areas where receiver coverage may be sparse, interferometric velocity analysis provides a direct alternative if conventional velocity methods are not applicable.

In Chapter 3 we use a simpler method to extract the velocities of the deeper layers. In this application, interfering reflections in the correlation gathers are suitable for recovering the seismic velocity and thickness of the first layer. However, in the case of one-sided illumination we find that the Green's function estimates (the Green's functions after summation over sources in the correlation gather) contain very weak reflections and are instead dominated by non-physical

refractions. This inherent bias allows refraction velocities to be estimated from the non-physical refractions using a $\tau - p$ domain semblance analysis of the Green's function estimates. The estimated velocities are easily identified as repeating bright spots on the semblance panel. The results demonstrate that the reflected and refracted energy can be analysed relatively independently if both the correlation gathers and Green's function estimates are used.

It has recently been shown that the surface-wave Green's function estimates from a field data set obtained using source-receiver interferometry show improvement over the Green's functions obtained using cross-correlational interferometry. No explanation why this may occur has been proposed. In Chapter 4, we show that source-receiver interferometry results in improved reflected Green's functions. The non-physical reflections or spurious multiples (i.e., cross-correlations between reflections from different interfaces) are often considered as unwanted artifacts. We show that these non-physical reflections can be used constructively to create physical primary reflections and multiples as part of the convolution step within source-receiver interferometry. The non-physical reflections can be suppressed using a further convolution step. The non-physical reflections are very important in providing the resultant primary reflections and internal multiples because convolution between physical reflections merely provides the free-surface multiples. Convolution between non-physical and physical reflections provides the primary reflections and internal multiples. We also show that a set of these non-physical reflections allows interval velocities and layer thicknesses to be estimated directly without the need to first obtain root-mean-square velocities and two-way traveltimes and then perform a Dix-type inversion for layer properties.

The applications in this thesis demonstrate that non-physical arrivals provide complementary information along with the physical arrivals to obtain information about subsurface properties. From this viewpoint, it seems clear that ideally the

non-physical contributions should be analysed before being suppressed. Seismic interferometry continues to develop at pace and therefore we anticipate that applications which use non-physical arrivals await future discovery.

Bibliography

Aki, K., 1957, Space and time spectra of stationary stochastic waves with special reference to microtremors: Bull Earthq Res Inst, **35**, 415–456.

Bakulin, A., and R. Calvert, 2006, The virtual source method: Theory and case study: Geophysics, **71**, no. 4, SI139–SI150.

Berkhout, A. J., and D. J. Verschuur, 1997, Estimation of multiple scattering by iterative inversion, Part I: Theoretical considerations: Geophysics, **62**, 1586–1595.

Berkhout, A. J. G., 2008, Changing the mindset in seismic data acquisition: The Leading Edge, **27**, 924–938.

Brekhovskikh, L. M., 1960, Waves in layered media: Academic Press.

Campillo, M., and A. Paul, 2003, Long-range correlations in the diffuse seismic coda: Science, **299**, 547–549.

Castle, R. J., 1994, A theory of normal moveout: Geophysics, **59**, 983–999.

Claerbout, J. F., 1968, Synthesis of a layered medium from its acoustic transmission response: Geophysics, **33**, 264–269.

Clayton, R. W., and R. A. Wiggins, 1976, Source shape estimation and deconvolution of teleseismic body-waves: Geophysical Journal of the Royal Astronomical Society, **47**, 151–177.

Cole, S., 1995, Passive seismic and drill-bit experiments using 2-D arrays: PhD thesis, Stanford University.

Curtis, A., 2009, Source-receiver seismic interferometry: SEG Technical Program

Expanded Abstracts, **28**, 3655–3659.

Curtis, A., and D. Halliday, 2010a, Directional balancing for seismic and general wavefield interferometry: Geophysics, **75**, no. 1, SA1–SA14.

———, 2010b, Source-receiver wavefield interferometry: Physical Review E, **81**, 046601.

Curtis, A., H. Nicolson, D. Halliday, J. Trampert, and B. Baptie, 2009, Virtual seismometers in the subsurface of the Earth from seismic interferometry: Nature Geoscience, **2**, 700–704.

Derode, A., E. Larose, M. Campillo, and M. Fink, 2003a, How to estimate the green's function of a heterogeneous medium between two passive sensors? Application to acoustic waves: Applied Physics Letters, **83**, 3054–3056.

Derode, A., E. Larose, M. Tanter, J. de Rosny, A. Tourin, M. Campillo, and M. Fink, 2003b, Recovering the green's function from field-field correlations in an open scattering medium (L): The Journal of the Acoustical Society of America, **113**, 2973–2976.

Diebold, J. B., and P. L. Stoffa, 1981, The traveltime equation, tau-p mapping, and inversion of common midpoint data: Geophysics, **46**, 238–254.

Dix, C. H., 1955, Seismic velocities from surface measurements: Geophysics, **20**, 68–86.

Douma, H., and R. Snieder, 2006, Correcting for bias due to noise in coda wave interferometry: Geophysical Journal International, **164**, 99–108.

Draganov, D., R. Ghose, E. Ruigrok, J. Thorbecke, and K. Wapenaar, 2010, Seismic interferometry, intrinsic losses and Q-estimation: Geophysical Prospecting, **58**, 361–373.

Dragoset, B., 1995, Geophysical applications of adaptive-noise cancellation: SEG Technical Program Expanded Abstracts, **14**, 1389–1392.

Duguid, C., D. Halliday, and A. Curtis, 2011, Source-receiver interferometry for seismic wavefield construction and ground roll removal: The Leading Edge, **30**,

838–843.

Forghani, F., and R. Snieder, 2010, Underestimation of body waves and feasibility of surface-wave reconstruction by seismic interferometry: The Leading Edge, **29**, 790–794.

Galetti, E., and A. Curtis, 2012, Generalised receiver functions and seismic interferometry: Tectonophysics.

González-Serrano, A., and J. F. Claerbout, 1984, Wave-equation velocity analysis: Geophysics, **49**, 1432–1456.

Halliday, D., and A. Curtis, 2008, Seismic interferometry, surface waves and source distribution: Geophysical Journal International, **175**, 1067–1087.

———, 2009a, Generalized optical theorem for surface waves and layered media: Physical Review E, **79**, 056603.

———, 2009b, Seismic interferometry of scattered surface waves in attenuative media: Geophysical Journal International, **178**, 419–446.

Hanafy, S. M., W. Cao, and G. T. Schuster, 2009, Interferometric interpolation of 3D SSP data: SEG Technical Program Expanded Abstracts, **28**, 3138–3142.

Hong, T. K., and W. Menke, 2006, Tomographic investigation of the wear along the San Jacinto fault, southern California: Physics of the Earth and Planetary Interiors, **155**, 236–248.

Ikelle, L. T., 2006, A construct of internal multiples from surface data only: the concept of virtual seismic events: Geophysical Journal International, **164**, 383–393.

Jakubowicz, H., 1998, Wave equation prediction and removal of interbed multiples: SEG Technical Program Expanded Abstracts, **17**, 1527–1530.

Kennett, B. L. N., 1977, Toward a more detailed picture of the oceanic crust and mantle: Marine Geophysical Researches, **3**, 7–42.

Koren, Z., and I. Ravve, 2006, Constrained dix inversion: Geophysics, **71**, no. 6, R113–R130.

Kumar, P., K. Sain, and H. C. Tewari, 2003, A direct method of estimating depth to a reflector from seismic wide-angle reflection times: Geophysical Journal International, **152**, 740–748.

Lobkis, O. I., and R. L. Weaver, 2001, On the emergence of the green's function in the correlations of a diffuse field: The Journal of the Acoustical Society of America, **110**, 3011–3017.

Mallinson, I., P. Bharadwaj, G. Schuster, and H. Jakubowicz, 2011, Enhanced refractor imaging by supervirtual interferometry: The Leading Edge, **30**, 546–550.

Mehta, K., A. Bakulin, J. Sheiman, R. Calvert, and R. Snieder, 2007, Improving the virtual source method by wavefield separation: Geophysics, **72**, no. 4, V79–V86.

Mehta, K., R. Snieder, R. Calvert, and J. Sheiman, 2008, Acquisition geometry requirements for generating virtual-source data: The Leading Edge, **27**, 620–629.

Meissner, R., 1965, Multiple events in refraction shooting: Geophysical Prospecting, **13**, 617–658.

Mikesell, D., and K. van Wijk, 2011, Seismic refraction interferometry with a semblance analysis on the crosscorrelation gather: Geophysics, **76**, SA77–SA82.

Mikesell, D., K. van Wijk, A. Calvert, and M. Haney, 2009, The virtual refraction: Useful spurious energy in seismic interferometry: Geophysics, **74**, no. 3, A13–A17.

Muijs, R., J. O. A. Robertsson, and K. Holliger, 2007, Prestack depth migration of primary and surface-related multiple reflections: Part I–imaging: Geophysics, **72**, no. 2, S59–S69.

Neidell, N. S., and M. T. Taner, 1971, Semblance and other coherency measures for multichannel data: Geophysics, **36**, 482–497.

Nowroozi, A. A., 1990, Interpretation of seismic reflection records: Direct

calculation of interval velocities and layer thicknesses from travel-times: Pure and Applied Geophysics, **133**, 103–115.

Palmer, D., 2001, Imaging refractors with the convolution section: Geophysics, **66**, 1582–1589.

Poletto, F., and B. Farina, 2010, Synthesis and composition of virtual-reflector (VR) signals: Geophysics, **75**, no. 4, SA45–SA59.

Poletto, F., and K. Wapenaar, 2009, Virtual reflector representation theorem (acoustic medium): The Journal of the Acoustical Society of America, **125**, no. 4, EL111–EL116.

Poliannikov, O. V., 2011, Retrieving reflections by source-receiver wavefield interferometry: Geophysics, **76**, no. 1, SA1–SA8.

Rickett, J., and J. Claerbout, 1999, Acoustic daylight imaging via spectral factorization: Helioseismology and reservoir monitoring: The Leading Edge, **18**, 957–960.

Robertsson, J. O. A., J. O. Blanch, and W. W. Symes, 1994, Viscoelastic finite-difference modeling: Geophysics, **59**, 1444–1456.

Sabra, K. G., P. Roux, and W. A. Kuperman, 2005, Arrival-time structure of the time-averiaged ambient noise cross-correlation function in an oceanic waveguide: The Journal of the Acoustical Society of America, **117**, 164–174.

Sain, K., and K. L. Kaila, 1996, Direct calculation of interval velocities and layer thicknesses from seismic wide-angle reflection times: Geophysical Journal International, **125**, 30–38.

Schultz, P. S., 1982, A method for direct estimation of interval velocities: Geophysics, **47**, 1657–1671.

Schuster, G. T., J. Yu, J. Sheng, and J. Rickett, 2004, Interferometric/daylight seismic imaging: Geophysical Journal International, **157**, 838–852.

Shapiro, N. M., M. Campillo, L. Stehly, and M. H. Ritzwoller, 2005, High-resolution surface-wave tomography from ambient seismic noise: Science, **307**,

1615–1618.

Slob, E., D. Draganov, and K. Wapenaar, 2007, Interferometric electromagnetic Green's functions representations using propagation invariants: Geophysical Journal International, **169**, 60–80.

Slob, E., and K. Wapenaar, 2007, Electromagnetic Green's functions retrieval by cross-correlation and cross-convolution in media with losses: Geophysical Research Letters, **34**, L05307.

Snieder, R., 2004, Extracting the green's function from the correlation of coda waves: A derivation based on stationary phase: Physical Review E, **69**, 046610.

———, 2007, Extracting the Green's function of attenuating heterogeneous acoustic media from uncorrelated waves: The Journal of the Acoustical Society of America, **121**, 2637–2643.

Snieder, R., J. Sheiman, and R. Calvert, 2006a, Equivalence of the virtual-source method and wave-field deconvolution in seismic interferometry: Physical Review E, **73**, 066620.

Snieder, R., K. van Wijk, M. Haney, and R. Calvert, 2008, Cancellation of spurious arrivals in green's function extraction and the generalized optical theorem: Physical Review E, **78**, 036606.

Snieder, R., K. Wapenaar, and K. Larner, 2006b, Spurious multiples in seismic interferometry of primaries: Geophysics, **71**, no. 4, SI111–SI124.

Taner, M. T., and F. Koehler, 1969, Velocity spectra-digital computer derivation applications of velocity functions: Geophysics, **34**, 859–881.

Tatanova, M., A. Bakulin, K. Mehta, V. Korneev, and B. Kashtan, 2008, Reconstructing head waves with virtual source method: SEG Technical Program Expanded Abstracts, **27**, 183–187.

van der Neut, J., and A. Bakulin, 2009, Estimating and correcting the amplitude radiation pattern of a virtual source: Geophysics, **74**, no. 2, SI27–SI36.

van der Neut, J., J. Thorbecke, K. Mehta, E. Slob, and K. Wapenaar,

2011, Controlled-source interferometric redatuming by crosscorrelation and multidimensional deconvolution in elastic media: Geophysics, **76**, SA63–SA76.

van Manen, D.-J., A. Curtis, and J. O. A. Robertsson, 2006, Interferometric modeling of wave propagation in inhomogeneous elastic media using time reversal and reciprocity: Geophysics, **71**, no. 4, SI47–SI60.

van Manen, D.-J., J. O. A. Robertsson, and A. Curtis, 2005, Modeling of wave propagation in inhomogeneous media: Physical Review Letters, **94**, 164301.

Vasconcelos, I., J. Gaiser, A. Calvert, and C. Calderón-Macías, 2008, Retrieval and suppression of surface waves using interferometry by correlation and deconvolution: SEG Technical Program Expanded Abstracts, 2566–2570.

Vasconcelos, I., and R. Snieder, 2008a, Interferometry by deconvolution: Part 1 - Theory for acoustic waves and numerical examples: Geophysics, **73**, no. 3, S115–S128.

———, 2008b, Interferometry by deconvolution: Part 2 - Theory for elastic waves and application to drill-bit seismic imaging: Geophysics, **73**, no. 3, S129–S141.

Wang, Y., S. Dong, and Y. Luo, 2010, Model-based interferometric interpolation method: Geophysics, **75**, no. 6, WB211–WB217.

Wang, Y., Y. Luo, and G. T. Schuster, 2009, Interferometric interpolation of missing seismic data: Geophysics, **74**, no. 3, SI37–SI45.

Wapenaar, K., 2003, Synthesis of an inhomogeneous medium from its acoustic transmission response: Geophysics, **68**, 1756–1759.

———, 2004, Retrieving the elastodynamic green's function of an arbitrary inhomogeneous medium by cross correlation: Physical Review Letters, **93**, 254301.

———, 2006, Green's function retrieval by cross-correlation in case of one-sided illumination: Geophysical Research Letters, **33**, L19304.

———, 2011, On the relation between seismic interferometry and the simultaneous-source method: 73rd Annual Conference and Exhibition, EAGE,

Extended Abstracts, C020.

Wapenaar, K., D. Draganov, R. Snieder, X. Campman, and A. Verdel, 2010a, Tutorial on seismic interferometry: Part 1 — basic principles and applications: Geophysics, **75**, no. 5, 75A195–75A209.

Wapenaar, K., and J. Fokkema, 2006, Green's function representations for seismic interferometry: Geophysics, **71**, no. 4, SI33–SI46.

Wapenaar, K., E. Slob, R. Snieder, and A. Curtis, 2010b, Tutorial on seismic interferometry: Part 2 — underlying theory and new advances: Geophysics, **75**, 75A211–75A227.

Wapenaar, K., J. van der Neut, and E. Ruigrok, 2008, Passive seismic interferometry by multidimensional deconvolution: Geophysics, **73**, no. 6, A51–A56.

Wapenaar, K., J. van der Neut, E. Ruigrok, D. Draganov, J. Hunziker, E. Slob, J. Thorbecke, and R. Snieder, 2011, Seismic interferometry by crosscorrelation and by multidimensional deconvolution: a systematic comparison: Geophysical Journal International, **185**, 1335–1364.

Weaver, R. L., and O. I. Lobkis, 2001, Ultrasonics without a source: Thermal fluctuation correlations at mhz frequencies: Physical Review Letters, **87**, 134301–1–134301–4.

Yilmaz, Ö., 2001, Seismic data analysis: Society of Exploration Geophysicists.

Zhu, L., and H. Kanamori, 2000, Moho depth variation in southern California from teleseismic receiver functions: Journal of Geophysical Research-Solid Earth, **105**, 2969–2980.

Appendix 1: Extension of the shifted hyperbola equation to account for multiple raypaths within each layer

Taner and Koehler (1969) showed that for a horizontally-layered Earth, the square of the traveltime, t^2, can be expressed as a power series with respect to the horizontal distance, x^2:

$$t^2 = c_1 + c_2 x^2 + c_3 x^4 + c_4 x^6 + \ldots, \tag{A1}$$

where the coefficients c_1, c_2, $c_3, \ldots$ are constants dependent on the layer thickness and seismic velocity of subsurface strata. When the maximum offset is small compared to the depth of target, equation A1 is truncated to the first two terms, with c_1 and c_2 defined as,

$$c_1 = \left(\sum_{k=1}^{M} t_k \right)^2, \tag{A2}$$

$$c_2 = \frac{\sum_{k=1}^{M} t_k}{\sum_{k=1}^{M} t_k V_k^2} \equiv \frac{1}{V_{rms}^2}, \tag{A3}$$

where t_k and V_k are the zero-offset two-way traveltime and interval velocity in the kth layer, respectively, and V_{rms} is the rms velocity.

Through close inspection of the acoustic model in Figure 2.1, it is clear that the maximum offset, for example from source 1 to receiver 301, greatly exceeds the depth to the third layer. Thus, equation A1 will become inaccurate at these far offsets.

One way to obtain higher accuracy at far offset is to include the fourth-order term in x in equation A1 (Yilmaz, 2001). However, the term c_3, as well as coefficients c_4 and c_5, becomes increasingly complex and difficult to compute. To overcome this difficulty, Castle (1994) showed that the traveltime equation A1, exact to fourth-order, can be expressed as a time-shifted hyperbola

of the following form:

$$t = t_0\left(1 - \frac{1}{S}\right) + \sqrt{\left(\frac{t_0}{S}\right)^2 + \frac{x^2}{SV_{rms}^2}} \tag{A4}$$

where t_0 is the zero-offset two-way traveltime:

$$t_0 = \sum_{k=1}^{M} t_k = 2\sum_{k=1}^{M} \frac{Z_k}{V_k}. \tag{A5}$$

Here, Z_k is the layer thickness of the kth layer. Before defining S we let

$$\mu_j = \frac{1}{t_0}\sum_{k=1}^{M} V_k^j t_k. \tag{A6}$$

The constant S is equal to

$$S = \frac{\mu_4}{\mu_2^2}. \tag{A7}$$

Note that

$$\mu_2 = V_{rms}^2. \tag{A8}$$

When S takes the value of 1, the shifted hyperbola traveltime in equation A4 assumes the traveltime in equation A1 up to second-order.

We wish to extend the traveltime in equation A4 to account for multiple raypaths within each layer. To achieve this objective, we simply replace the two-way traveltime t_0 in equation A5 by an equation of the form,

$$t_{0_{mult}} = \sum_{k=1}^{M} t_k = 2\sum_{k=1}^{M} \frac{b_{k,r_j} Z_k}{V_k}, \tag{A9}$$

where b_{k,r_j} is the number of bounce points in the kth layer to the jth receiver. Hence, equations A6 and A7 change accordingly. Substituting $t_{0_{mult}}$ and the appropriate form of equation A6 and A7 into the time-shifted hyperbola

traveltime, equation A4 is expressed as

$$t = t_{0_{mult}} \left(1 - \frac{1}{S} \right) + \sqrt{\left(\frac{t_{0_{mult}}}{S} \right)^2 + \frac{x^2}{S V_{rms}^2}}. \tag{A10}$$

It is important to note that for the uppermost layer (i.e., when $k = 1$ in equation A9) any term involving the layer thickness Z_1 suggests that the traveltime is computed through the complete layer. This is consistent only when both sources and receivers are positioned at the surface of the Earth. In fact, the acquisition geometry of Figure 2.11 illustrates that sources and receivers are positioned at depth beneath the free surface. Therefore, when we compute the traveltime t of a ray passing through layer 1, we must replace $2b_{k,r_j}Z_1$ in equation A9 by the expression $(2b_{k,r_j}Z_1 - z_{r_j} - z_s)$ where z_s and z_{r_j} are the depth of the source and receiver, respectively. For $k \geq 2$ the term $b_{k,r_j}Z_k$ is sufficient.